

AD-A169 010

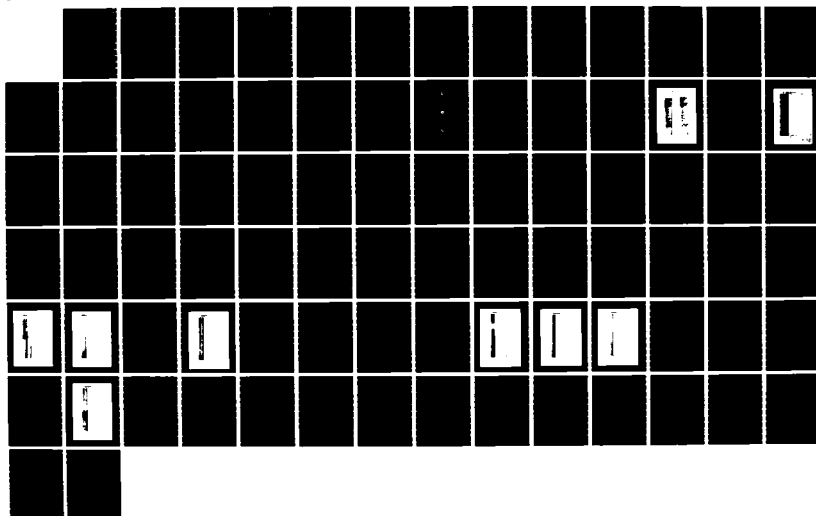
MAGNETOSPHERIC PLASMA STUDIES USING DATA FROM THE
DYNAMICS EXPLORER HIGH A. (U) SOUTHWEST RESEARCH INST
SAN ANTONIO TX J N BARFIELD FEB 86 AFGL-TR-86-0034
F19628-82-K-0024

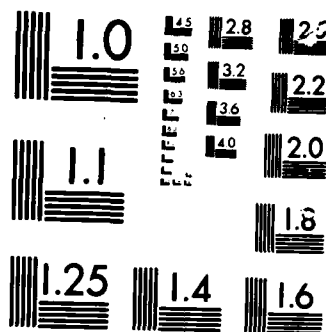
1/1

UNCLASSIFIED

F/G 4/1

NL





MICROCOPY

CHART

12

AFGL-TR-86-0034

MAGNETOSPHERIC PLASMA STUDIES USING DATA FROM THE DYNAMICS EXPLORER
HIGH AND LOW ALTITUDE PLASMA INSTRUMENTS

J. N. Barfield

Southwest Research Institute
P. O. Drawer 28510
San Antonio, TX 78284

Final Report
15 April 1982 to 31 December 1985

February 1986

Approved for public release; distribution unlimited


DTIC FILE COPY

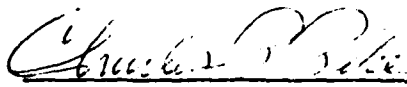
AIR FORCE GEOPHYSICS LABORATORY
AIR FORCE SYSTEMS COMMAND
UNITED STATES AIR FORCE
HANSCOM AFB, MA 01731

DTIC
ELECTE
JUN 30 1986
B

86 6 30 02 5

"This technical report has been reviewed and is approved for publication"


Roger P. Vancour
Contract Manager


Charles P. Pike
Branch Chief

FOR THE COMMANDER


RITA C. SAGALYN
Division Director

This report has been reviewed by the ESD Public Affairs Office (PA) and is releasable to the National Technical Information Service (NTIS).

Qualified requestors may obtain additional copies from the Defense Technical Information Center. All others should apply to the National Technical Information Service.

If your address has changed, or if you wish to be removed from the mailing list, or if the addressee is no longer employed by your organization, please notify AFGL/DAA, Hanscom AFB, MA 01731. This will assist us in maintaining a current mailing list.

Do not return copies of this report unless contractual obligations or notices on a specific document requires that it be returned.

6a. NAME OF PERFORMING ORGANIZATION Southwest Research Institute			6b. OFFICE SYMBOL (If applicable)		7a. NAME OF MONITORING ORGANIZATION Air Force Geophysics Laboratory		
6c. ADDRESS (City, State, and ZIP Code) P.O. Drawer 28510 San Antonio, TX 78284			7b. ADDRESS (City, State, and ZIP Code) Hanscom AFB Massachusetts 01731-5000				
8a. NAME OF FUNDING/SPONSORING ORGANIZATION		8b. OFFICE SYMBOL (If applicable)		9. PROCUREMENT INSTRUMENT IDENTIFICATION NUMBER F19628-82-K-0024			
8c. ADDRESS (City, State, and ZIP Code)			10. SOURCE OF FUNDING NUMBERS				
			PROGRAM ELEMENT NO 62101F	PROJECT NO 7661	TASK NO 10	WORK UNIT ACCESSION NO. AB	
11. TITLE (Include Security Classification) Magnetospheric Plasma Studies Using Data From the Dynamics Explorer High and Low Altitude Plasma Instruments							
12. PERSONAL AUTHOR(S) J. N. Barfield							
13a. TYPE OF REPORT FINAL REPORT		13b. TIME COVERED FROM 4/15/82 TO 12/31/85		14. DATE OF REPORT (Year, Month, Day) 1986 February		15. PAGE COUNT 84	
16. SUPPLEMENTARY NOTATION							
17. COSATI CODES			18. SUBJECT TERMS (Continue on reverse if necessary and identify by block number)				
FIELD	GROUP	SUB-GROUP					
			Magnetosphere Space Plasma				
			Ionosphere Environmental Specification				
			Substorm				
19. ABSTRACT (Continue on reverse if necessary and identify by block number)							
<p>The reported research focused primarily upon plasma processes in and near the plasma cusp. The following areas were studied:</p> <ul style="list-style-type: none"> - plasma injection and transport in the mid-altitude polar cusp; - observations of counterstreaming electrons at high altitudes, - observations of upward electron beams and their relationship to region-1 Birkeland currents; - observations of the electron population responsible for the 6300A SAR arc emission, - polar rain observations; - polar wind observations; and - observations of ion and electron acceleration events produced by parallel electric fields. <p>The primary observing platform for the research reported here was Dynamics Explorer 1 (DE-1). The DE-1 High Altitude Plasma Instrument (HAPI) consists of five electrostatic analyzers</p>							
20. DISTRIBUTION/AVAILABILITY OF ABSTRACT <input type="checkbox"/> UNCLASSIFIED/UNLIMITED <input type="checkbox"/> SAME AS RPT <input type="checkbox"/> DTIC USERS				21. ABSTRACT SECURITY CLASSIFICATION Unclassified			
22a. NAME OF RESPONSIBLE INDIVIDUAL Roger Vancour			22b. TELEPHONE (Include Area Code)		22c. OFFICE SYMBOL AFGL/PHK		

19.

mounted in a fan-shaped angular array at angles of 45° , 78° , 90° , 102° , and 135° , with respect to the spacecraft spin axis. Each analyzer makes differential measurements of electrons and positive ions over an energy/charge range of 5 eV/e to 32 keV/e. Energy stepping proceeds at commandable rates of up to 64/sec⁻¹, providing three-dimensional plasma distribution functions at the six-second spin rate of DE-1.

Approved
NTIS
ITC
JUN 30 1986

✓

DTIC
ELECTE
JUN 30 1986
S D
B

A-1



TABLE OF CONTENTS

	<u>PAGE</u>
I. INTRODUCTION	1
II. PLASMA INJECTION AND TRANSPORT IN THE MID-ALTITUDE POLAR CUSP	2
III. OBSERVATIONS OF COUNTERSTREAMING ELECTRONS AT HIGH ALTITUDES	8
A. Type 1 Counterstreaming Electrons	8
B. Type 2 Counterstreaming Electrons	11
C. Correlative Observations of Counterstreaming Electrons	13
D. Conclusions	28
IV. UPWARD ELECTRON BEAMS	33
A. Introduction and Observations	33
B. Electron Currents and Magnetic Perturbations	34
C. Acceleration Mechanism	35
D. Conclusions	38
V. OBSERVATIONS OF A HEATED ELECTRON POPULATION ASSOCIATED WITH THE 6300 A SAR ARC EMISSION	39
A. Introduction and Observations	39
B. Discussion	41
C. Summary	44
VI. POLAR RAIN OBSERVATIONS	46
VII. ACCELERATED POLAR WIND	54
VIII. OBSERVATIONS OF ION AND ELECTRON ACCELERATION EVENTS PRODUCED BY PARALLEL ELECTRIC FIELDS	61
IX. PUBLICATIONS SUPPORTED BY CONTRACT	67
X. PAPERS PRESENTED AT SCIENTIFIC MEETINGS	68
REFERENCES	

LIST OF ILLUSTRATIONS

<u>Figure</u>	<u>Page</u>
1 Computer energy/pitch-angle relationship for particles injected at geocentric radial distance R_i on the 78° dipole magnetic field line and observed at a later time at a distance of $4 R_E$ on the same field line. The shaded region is the 400 km loss cone. Data points denote the energy of peak ion energy flux observed during one full spin of DE-1 (dots for 0° to 180° and triangles for 180° to 0°).	4
2 Temporal development of computed energy/pitch angle relationship for H^+ ions injected at $R_i = 8 R_E$ and observed at $R = 4 R_E$.	5
3 Λ -MLT plot of ion flow vectors measured nearly simultaneously at $\sim 19,000$ km (DE-1) and ~ 500 km altitude (DE-2) on September 29, 1981. At 14:06 UT DE-2 was moving poleward at $\Lambda = 78.7^\circ$ and MLT = 11.14 hr. UT in hours and minutes is noted along the DE-1 orbital track.	7
4 Electron distribution function of type 1 counterstreaming electrons (measured by DE-1 and S3-3) and field-aligned electron beam (measured by ATS-6).	10
5 Electron phase space density contours (a) before, (b) during and (c) after a type 2 counterstreaming electron event.	12
6 Schematics of V-shaped potential contours with a potential island.	14
7 Energy-time spectrograms of electron energy fluxes at 0° pitch angle (top) and 90° pitch angle (bottom).	16
8 Number density and total energy flux integrated from 18 to 10,000 eV over the whole pitch angle range.	17
9 Energy-time spectrogram of electron (top) and Ion (bottom) energy fluxes. The detector's pitch angle is plotted in the center panel.	18
10 Phase-space density contours of the logarithm of the electron distribution function. A downward electron beam is displayed as a contour island centered on the positive $V_{ }$ axis.	20
11 Phase-space contours of constant distribution function during a type-1 counterstreaming electron event.	21
12 Three components of magnetic fields for the DE-1 pass shown in Figure 1.	22
13 STARE latitudinal profile of electron drift velocities versus time on day 261, 1981.	24

<u>Figure</u>		<u>Page</u>
14	Ground magnetograms in the northern auroral zone on 18 September (day 261), 1981.	26
15	Comparison of the current density deduced from the plasma data (top) and the current density deduced from the magnetic field data (center). The bottom panel gives the azimuthal magnetic field component from which the current density was deduced.	27
16	Ratio of current densities $I(<235 \text{ eV})/I_{\text{total}}$ versus I_{total} for downward currents. The current density $I(<235 \text{ eV})$ is integrated from the plasma data from 18 to 10,000 eV.	29
17	Ratio of $I(<235 \text{ eV})/I_{\text{total}}$ versus I_{total} for upward currents.	30
18	Electron distribution functions in the downward field-aligned direction.	31
19	Electron distribution functions in the upward field-aligned direction.	32
20	Field-aligned current densities computed from the measured hot-plasma distributions (top panel) and from the measured ΔB perturbations (bottom panel). Positive currents are upward, negative currents downward. The shaded regions of the downward current are identified as region-1 Birkeland currents.	36
21	Electron distribution-function contours in the v_{\parallel}, v_{\perp} plane averaged over two rotations of the DE-1 spacecraft. Also plotted is a hyperbola defined by eq. (2) for a potential drop, $V_0 = 30V$, with maximum altitude at 5870 km.	37
22	Contour plot of 6300Å emission as measured from Richland, WA. Contour intervals are 100 R. The path of DE-2, projected to 425 km altitude, is shown as a dashed line. The position of Richland, WA is depicted by the artificially produced contours at center of mapping.	40
23	Typical field aligned electron spectrum taken near 04:05:20 UT along with the corresponding 2-D phase space contour plot. The latter distinctly shows the field aligned flow velocity of the low energy electron population.	42
24	Profile of 6300Å emission (Rayleighs) along the DE-2 path from the Richland, WA (solid line) and Eureka, MT MASP (dashed line) units. Near 55°A the emissions are computed at a height of 300 km--typical of auroral 6300Å emission. Several values of the measured distribution function are overlayed over the emission plot. Shown is the distribution function at 6.7 eV (open circles), 8.8 eV (solid circles) and 20.4 eV (solid triangles). The length of the solid line connecting the 6.8 and 8.8 eV data give an indication of the plasma temperature. The 20.4 eV data gives an indication of the photoelectron density.	43

<u>Figure</u>	<u>Page</u>
25a Energy-time spectrogram of 8° pitch angle electrons and 45° pitch angle ions as observed at DE-2.	47
25b Energy-time spectrogram of 8° pitch angle electrons and 45° pitch angle ions as observed at DE-2.	48
26 Line plots of average energy, energy flux, and density of downcoming electrons.	49
27 Energy-time spectrogram of electrons and ions. The detector's pitch angle is plotted in the center panel.	50
28 Line plots of number density, energy flux, and average energy of downcoming electrons.	52
29 Electron energy spectra from DE-1 and DE-2 in the cusp region.	53
30a Energy-time spectrogram using same format as Figure 3.	55
30b Energy-time spectrogram using same format as Figure 3.	56
30c Energy-time spectrogram using same format as Figure 3.	57
31 Velocity space spectrum for DE-2.	58
32 Evolution of polar wind. Shown are isocontours of the distribution function in phase space.	60
33 Energy-time spectrograms for 180° pitch angle ions and 0° pitch angle electrons observed at DE-1.	62
34a Isocontours of the distribution function for ions at DE-1.	63
34b Isocontours of the distribution function for electrons at DE-1.	64
35a Isocontours of the distribution function for ions at DE-1.	65
35b Isocontours of the distribution function for electrons at DE-1.	66

I. INTRODUCTION

The research pursued under this contract focused primarily upon plasma processes in and near the polar cusp. The following sections will cover the seven basic areas studied: Plasma Injection and Transport in the Mid-Altitude Polar Cusp (Section II); Observations of Counter-Streaming Electrons at High Altitudes (Section III); Observations of Upward Electron Beams and Their Relationship to Region-1 Birkeland Currents (Section IV); Observations of the Electron Population Responsible for the 6300A SARarc emission (Section V); Polar Rain Observations (Section VI); Polar Wind Observations (Section VII); and Observations of Ion and Electron Acceleration Events Produced by Parallel Electric Fields (Section VIII).

Section IX details the publications supported by contract, and Section X presents papers presented at scientific meetings.

The primary observing platform for the research reported here was Dynamics Explorer 1 (DE-1). The DE-1 High Altitude Plasma Instrument (HAPI) consists of five electrostatic analyzers mounted in a fan-shaped angular array at angles of 45°, 78°, 90°, 102°, and 135° with respect to the spacecraft spin axis. Each analyzer makes differential measurements of electrons and positive ions over an energy/charge range of 5 eV/e to 32 keV/e. Energy stepping proceeds at commandable rates of up to 64 sec⁻¹, providing three-dimensional plasma distribution functions at the six-second spin rate of DE-1 (Burch et al., 1981).

II. PLASMA INJECTION AND TRANSPORT IN THE MID-ALTITUDE POLAR CUSP

Ion fluxes in the cusp often show a "dispersion" signature, in which the characteristic ion energy falls with increasing latitude (Shelley et al., 1976; Reiff et al, 1977). The dispersion signature occurs because poleward ($\mathbf{E} \times \mathbf{B}$) convection acts as a "velocity filter" on the incoming plasma. Particles with large parallel velocities arrive at the earth sooner (therefore, more equatorward) than particles with lower parallel velocities. Pitch angle effects on the velocity dispersion are not important at low altitudes (Reiff et al, 1977). This is not the case in the mid-altitude cusp (Frank, 1971; Gurnett and Frank, 1978), where the transit time from injection to observation of a particle of a given energy is a strong function of pitch angle. This fact enables us to obtain independent measurements of the injection altitude for each spin of the DE-1 satellite and to determine local flow velocities as low as ~ 10 km/s.

On a typical polar-cusp pass, as the satellite enters the cusp, ion fluxes first appear in higher (~ 1 -3 keV) energy channels clustered about 0° (downward) pitch angles (α). Then the energy of peak ion energy flux decreases systematically and the distribution spreads to larger pitch angles in a distinctive 'V' pattern, in which the peak energy flux occurs at higher energies for larger pitch angles. As this pattern continues to evolve, the 'V' signatures deepen to reach energies near 200 eV at 0° and spread through all downward pitch angles and a wide range of upward pitch angles. Eventually, strong ion fluxes are observed at all pitch angles except for the narrow loss cone ($\sim 7^\circ$) around $\alpha = 180^\circ$. Finally, a dropout develops at $\alpha \sim 0^\circ$ and spreads through all downward pitch angles so that only upward moving ions, which have mirrored below the spacecraft, are observed.

We have attempted to explain the ion energy/pitch-angle signatures observed by DE-1 in the mid-altitude cusp by application of a simple plasma-injection model in which cusp field lines are convected through a spatially restricted region of plasma injection and then into the polar cap. In a dipole magnetic field the guiding center approximation is used to compute an $E(\alpha, t)$ relationship for particles observed at a nominal geocentric distance of $4 R_E$ and a dipole invariant latitude of 78° . The relationship has the following form:

$$E(\alpha_o, t) = \frac{M}{2t^2} \left[\int_{s_1}^{s_0} \frac{ds}{1 - \sin^2 \alpha_o \left(\frac{B(s)}{B_o} \right)} \right]^2 \quad (1)$$

where,

ds is arc length along a dipole field line,

s_o, s_i are the observation and injection points,

M is the particle mass,

$B(s)$ is the magnetic induction along the field line,

B_o is the magnetic induction at the observation point,

α_o is the observed pitch angle,

t is the transit time.

For $\alpha_o > 90^\circ$, the integration is carried down to the mirror altitude and back up the field line to the observation altitude.

Since M and t appear only in the factor $\frac{M}{2T^2}$ in eq. (1), the shape of the

$\log E$ vs. α_o curve for given injection and observation points will be independent of transit time and will be applicable to ions of all masses as well as to electrons. Computed $\log E$ vs. α_o curves are plotted in Fig. 1 for injection radii of $6 R_E$, $8 R_E$, $12 R_E$, and $16 R_E$, and an observation radius of $4 R_E$. For ease of comparison the four curves are adjusted to coincide at $\alpha_o = 90^\circ$. Also plotted in Fig. 1 are the DE observations for a single spin covering the time period from 14:07:30 to 14:07:36 on September 29, 1981. The data points in Fig. 1 are strongly indicative of an injection distance in the neighborhood of $8 R_E$ (geocentric). Injection distances beyond $12 R_E$ would clearly not result in the strong (E, α_o) dependence that is observed at $\sim 4 R_E$ by DE-1.

As the observation point moves to lower altitudes, the model predicts that the $\log E$ vs. α_o dependence will rapidly become weaker, causing the disappearance of any significant 'V' shape at, for example, the typical DE-2 altitude of 900 km. This prediction is borne out by the DE-2 observations and by the fact that no other low-altitude spacecraft or sounding rockets have observed the 'V' shaped $\log E$ vs. α_o relationship.

Fig. 2 displays the computed time evolution of the $\log E$ vs. α_o relationship for H^+ with an injection point at $8 R_E$ and an observation point at $4 R_E$. All the curves in Fig. 2 have the same shape, with the vertical position of each curve determined only by the relationship $vt = \text{constant}$. The energy scale in Fig. 2 is arbitrarily truncated at just over 3 keV and at 100 eV to coincide approximately with the high and low energy limits of the observed ion fluxes. Fig. 2 then allows one to trace the $\log E$ vs. α_o relationship as a function of elapsed time after injection for an input H^+ spectrum that falls off rapidly at energies above 3 keV and below 100 eV. For heavier ions the elapsed times in Fig. 2 would be multiplied by $\sqrt{M/MH^+}$; for electrons the times would be smaller by a factor of 43.

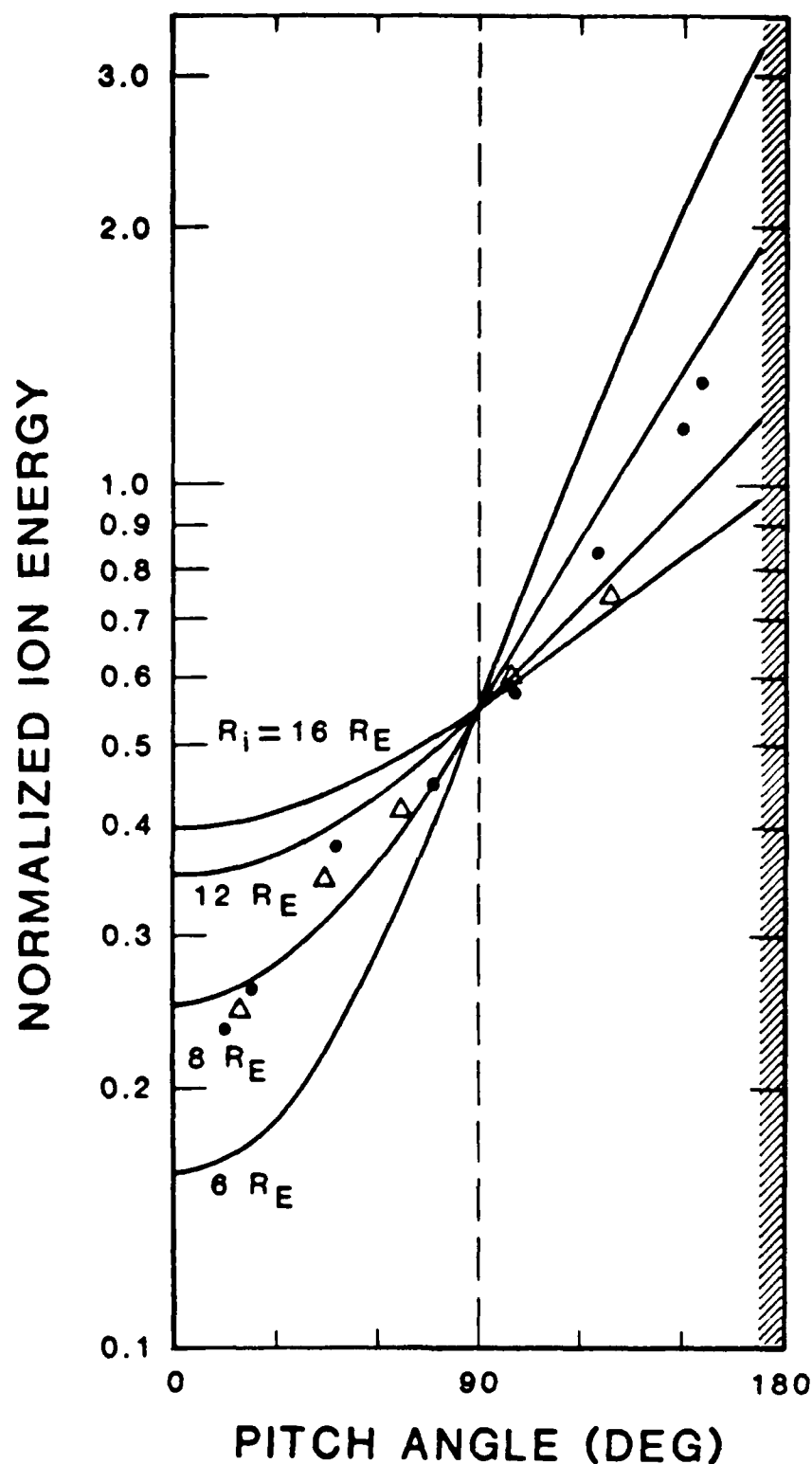


Figure 1. Computer energy/pitch-angle relationship for particles injected at geocentric radial distance R_i on the 78° dipole magnetic field line and observed at a later time at a distance of $4 R_E$ on the same field line. The shaded region is the 400 km loss cone. Data points denote the energy of peak ion energy flux observed during one full spin of DE-1 (dots for 0° to 180° and triangles for 180° to 0°).

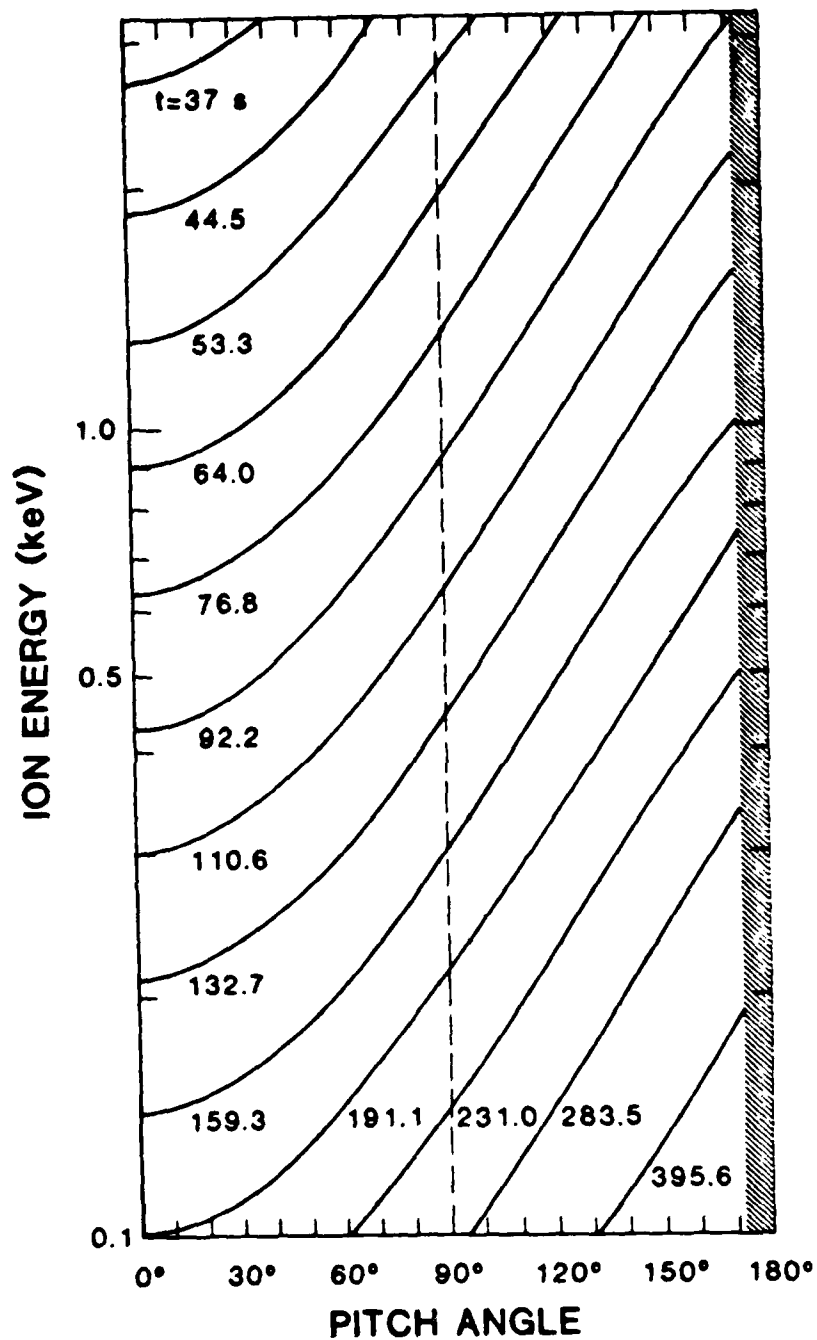


Figure 2. Temporal development of computed energy/pitch angle relationship for H^+ ions injected at $R_i = 8 R_E$ and observed at $R = 4 R_E$.

The time evolution of the $\log E$ vs. α_0 curves could result from the convection of cusp field lines through a restricted region of plasma injection or from a single impulsive injection event over the entire cusp. However, in the latter case, unless cusp ion injection is very infrequent (several minutes between injections) several of the curves of Fig. 2 would exist simultaneously, and the distinct 'V'-shaped E, α_0 signature would not appear. Time-dependent injection no doubt occurs (Carlson and Torbert, 1980) but, to be consistent with DE-1 data, must be confined to a restricted injection region located near the low-latitude edge of the cusp.

The cusp velocity filter effect allows us to observe a specific velocity at each pitch angle. The velocity selected by the filter is gyrotropic, i.e., independent of gyrophase angle, if one is in the rest frame of the magnetic field line. If the field line is convecting past the spacecraft, the convection velocity adds vectorially to the velocity selected by the filter effect. Since each detector observes 90° pitch-angle particles twice per spacecraft spin, one can construct a particle phase-space distribution for the plane perpendicular to the magnetic field direction, and have ten independent look directions in that plane. Each look direction will show the velocity filter effect, with a peak distribution function at a specific velocity within the uncertainty due to the logarithmic spacing of the energy steps. We can then fit an offset circle to the velocity of the peak distribution function. The magnitude of the offset gives us the locally measured flow velocity, and the direction of the offset yields the direction from which the plasma is flowing. The flow velocities determined in this way at DE-1 are plotted along with concurrent DE-2 flow measurements (Heelis et al, 1981) in Fig. 3 for a typical cusp pass. The agreement between the two flow patterns is fairly good, considering the difficulty and uncertainty in the high-altitude measurement. The magnitude of flows in a dipole field geometry should map upward along field lines approximately as $r^{3/2}$. The flow velocities at DE-1 should, therefore, be roughly six times as high as at DE-2. Fig. 3 shows that the measured flow velocities are more nearly 15 to 20 times the DE-2 flows. Possible reasons for the apparent enhancement of flow velocities at higher altitudes will be the subject of further study.

The cusp plasma injection model presented above predicts that the shape of the $\log E$ vs. α_0 curves should be the same for ions and electrons if the altitudes of injection and observation are equal. However, the progression of the curve down the energy axis of Fig. 2 will proceed 43 times as fast for electrons as for H^+ . Since cusp electron energies are generally between 10 eV and 200 eV, Fig. 2 shows that the entire progression will take place during a time interval between about 5 seconds and 20 seconds following injection. In the continuous injection model this prediction means that for the 'V'-shaped signatures to be observed in the electrons, the spacecraft must cross a field line within about 10 seconds of the time it convected out of the injection region. However, there are times when electron 'V's are observed. As expected, the 'V' signatures are observed in only one or two spacecraft spin periods just adjacent to the cusp equatorward electron boundary. The ion 'V's are observed to be displaced poleward from the electron 'V's, again as expected from the simple model of a spatially restricted injection region from which cusp plasma is convected into the polar cap.

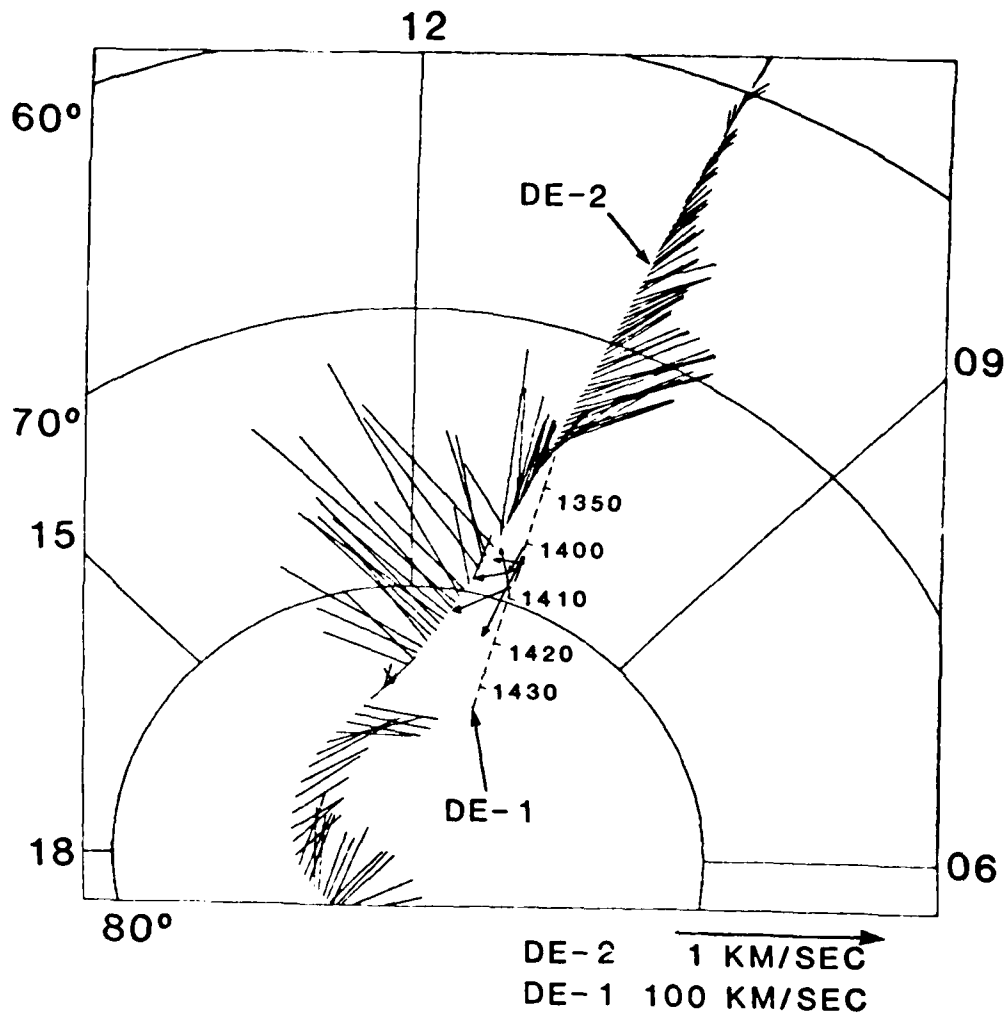


Figure 3. Λ -MLT plot of ion flow vectors measured nearly simultaneously at ~19,000 km (DE-1) and ~500 km altitude (DE-2) on September 29, 1981. At 14:06 UT DE-2 was moving poleward at $\Lambda = 78.7^\circ$ and MLT = 11.14 hr. UT in hours and minutes is noted along the DE-1 orbital track.

III. OBSERVATIONS OF COUNTERSTREAMING ELECTRONS AT HIGH ALTITUDES

Counterstreaming electrons have been observed by the High-Altitude Plasma Instrument (HAPI) on the DE-1 satellite. Previously, counterstreaming electrons have been detected by the S3-3 satellite as narrowly collimated beams of electrons with energies around one keV streaming both parallel and antiparallel to the magnetic field direction (Sharp et al., 1980). The S3-3 observations were made at altitudes between 4000 and 8000 km, while the present work pertains to observations of phenomena at higher altitudes ($\sim 2 R_E$).

Some features of counterstreaming electrons suggest that the mechanism responsible for electron acceleration is not associated with quasi-static electric fields (Sharp et al., 1980). For example, counterstreaming electrons have broad and unstructured energy spectra that can be fitted by Maxwellian functions with temperatures varying from 0.5 to 1 keV. Simultaneous measurements of conic ions of H⁺ and O⁺ in the pitch angle range of 90° to 125° during counterstreaming electron events also support the suggestion that a quasi-static electric field is not necessarily involved. However, the S3-3 satellite has occasionally detected peaks in the energy spectra of counterstreaming electrons.

Our survey of DE-1 HAPI data indicates that there are two distinct types of counterstreaming electron events. The first type of event is fairly stable and has broad and unstructured energy spectra not suggestive of acceleration by parallel electric fields. The second type is transient, and has beam-like distribution functions, which are consistent with acceleration by parallel electric fields. The first type is found to be similar to those frequently observed by the S3-3 satellite, while the presence of the second type is only hinted at in the S3-3 observations. These two types of events become quite distinguishable in the HAPI data because DE-1 has a faster spinning rate and the HAPI instrument is able to obtain the plasma distribution function at a higher time resolution as compared to the previous observations. We refer to the two types of events as type 1 and type 2 counterstreaming electron events respectively.

A. Type 1 Counterstreaming Electrons

A typical example of the electron distribution functions parallel and anti parallel to the field direction measured during a Type 1 counterstreaming event is presented in Figure 4 (with X symbols). An electron distribution function during one counterstreaming electron event observed by the S3-3 is deduced from Sharp et al (1980) and presented here for comparison (with triangle symbols). Except for a difference in the magnitude, these two distribution functions are very similar, as both can be approximated by a superposition of two Maxwellian functions. The temperature of the counterstreaming component is estimated to be about 200 eV, while the high energy isotropic component is estimated to have a temperature of about 1.5 keV. It appears that this type of event is related to the counterstreaming electron events reported by Sharp et al (1980).

The pitch angle range of counterstreaming electrons observed is about 30°, much wider than the local loss cone ($\sim 13^\circ$). The counterstreaming electron component is found to extend to larger pitch angles with smaller density; this might be considered as evidence of pitch angle scattering.

Figure 4 indicates that the distribution function of counterstreaming electrons is higher in the downward direction ($18^\circ < \alpha < 30^\circ$) than in the upward direction ($150^\circ < \alpha < 170^\circ$), more specifically, about four times higher at energies less than 2 keV. For this particular event, we found the downward enhancement to be about 2 for most times with an occasional enhancement in the opposite direction.

One type of counterstreaming electron frequently detected by the DE-1 HAPI instrument is an enhancement of field-aligned electron fluxes in both upward and downward directions. These counterstreaming electrons can be characterized by a Maxwellian distribution function with a temperature of about 200 eV. Their occurrence seems to be associated with isotropic precipitation of electrons with energies greater than 1 keV.

In Figure 4 we have also plotted two electron distribution functions of field-aligned electron beams measured by ATS-6 on the equatorial plane during substorm injection events (Lin et al., 1979; Moore and Arnoldy, 1982). It is interesting to notice that they are characterized by two Maxwellian functions as well. The magnetograms at local midnight are not available yet to learn if type 1 counterstreaming electrons occur during substorm injections, but the Kp magnetic activity index was certainly high (6-) for this event. It is possible that counterstreaming electrons and substorm injected electron beams are related.

A simple interpretation of type 1 counterstreaming electrons is that these electrons are produced at the topside ionosphere as thermal electrons heated to higher temperature through wave-particle interactions. The heated electrons appear as streaming particles as they move up along field lines. In order to explain the counterstreaming feature, the heating should take place continuously for long duration above both ionospheres. However, this interpretation does not explain the events described by Sharp et al (1980) which were much narrower than the loss cone.

Another possible interpretation is that type 1 counterstreaming electrons are secondary electrons produced by collisions of precipitating electrons with the atmosphere, as suggested for substorm-injected electron beams by Moore and Arnoldy (1982). Wave particle interactions then cause the electrons to be scattered outside the loss cone. The diffusion coefficient D can be estimated according to $(\Delta\alpha)^2/2\Delta t$, where $\Delta\alpha$ is the average pitch angle change and Δt is the interaction time. We estimate $\Delta\alpha$ to be about 12° and Δt to be the elapsed time for electrons of 500 eV to travel from the topside ionospheres to the satellite. We find D to be about $9 \times 10^{-3} \text{ sec}^{-1}$ for electrons originating from the northern hemisphere and $3 \times 10^{-3} \text{ sec}^{-1}$ for electrons originating from the southern hemisphere. The estimated D , which represents an upper limit, agrees in order of magnitude with the diffusion rate estimated for substorm-injected electron beams (Lin et al., 1979; Moore and Arnoldy, 1982).

We notice that the electron distribution function observed by the S3-3 is about one order of magnitude larger than the DE-1 measurement. This difference could be attributed to different events or instrumental effects. This difference might also be interpreted as an altitude dependence since the S3-3 altitude was much lower than the DE-1 altitude.

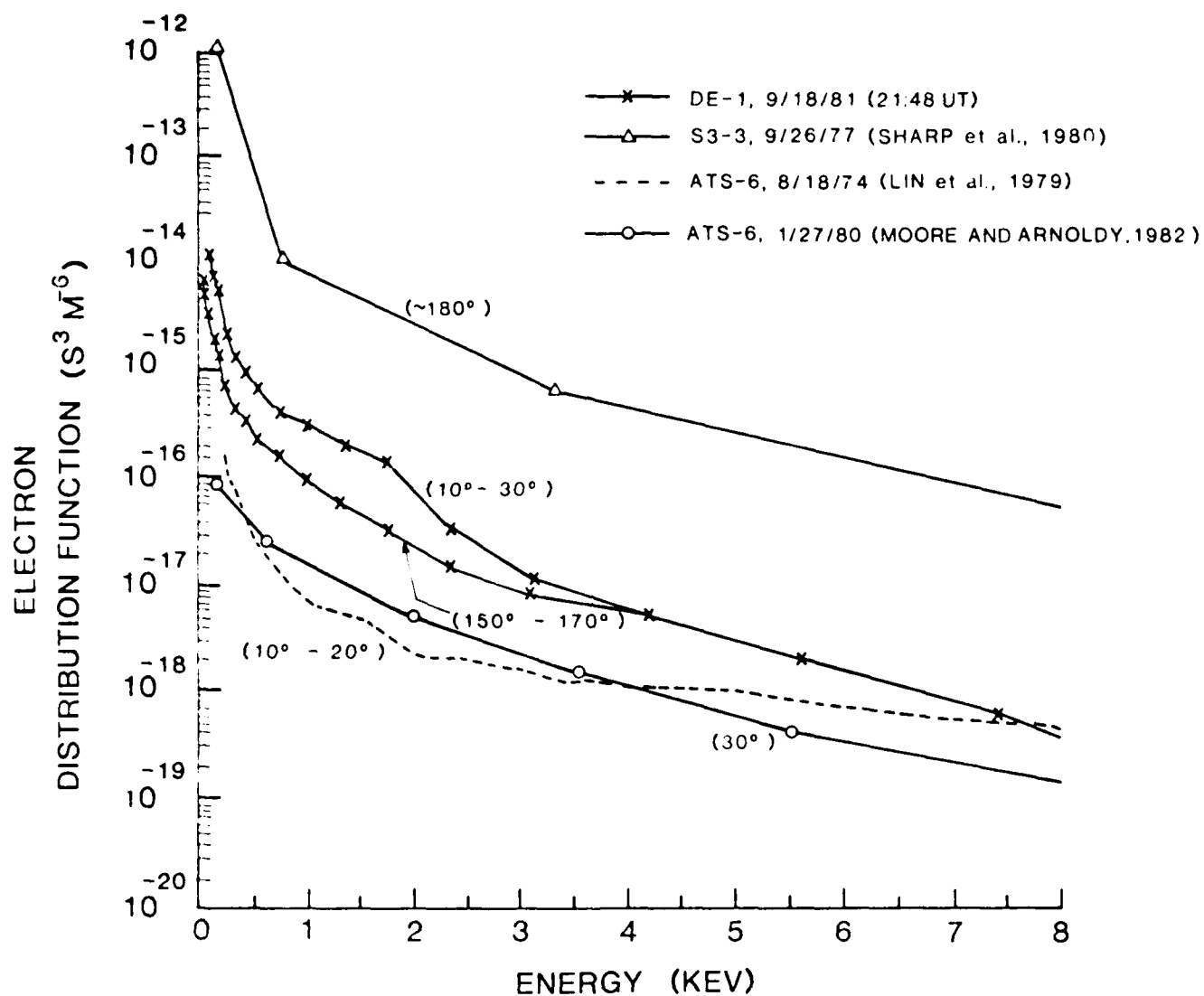


Figure 4. Electron distribution function of type 1 counterstreaming electrons (measured by DE-1 and S3-3) and field-aligned electron beam (measured by ATS-6).

B. Type 2 Counterstreaming Electrons

Contours of the logarithm of the electron distribution function are plotted in Figure 5 for three 6-second time intervals during a type 2 event: (a) before, (b) during and (c) after the counterstreaming electron event. In the figure, solid lines of circles and hyperbolas are theoretical predictions of the demarcation boundary between ionospheric and magnetospheric populations when a quasi-static electric field is assumed above and below the satellite (Chiu and Schulz, 1978; Mizera et al., 1981). Following Mizera et al. (1981), we infer the potential drop below the satellite to be the ion beam energy and the potential drop above the satellite to be the electron beam energy. The electron and ion beam energies are determined from the plot of the distribution function along the $V_{||}$ axis. The computed demarcation curves appear to characterize reasonably the phase space density contours before and after, but not during the event. More specifically, the hyperbolas in Figures 5a and 5c mark well the electron loss cone and the low energy core of presumably ionospheric electrons. Figures 5a and 5c indicate a slight enhancement of phase space density in the forbidden region between the circle and the hyperbola. These features resemble the S3-3 observations of electron phase space density contours during electrostatic shocks (e.g. see a review by Fennell et al., 1981). In contrast, the hyperbola in Figure 5b lies well inside the region of the low energy core. Furthermore, Figure 5b displays a distinct counterstreaming feature, an electron beam at an energy of 416 eV ($v_{||} = 12000$ km/sec) along the $+v_{||}$ axis and a weak electron beam at an energy of about 100 eV ($v_{||} = -5920$ km/sec) along the $-v_{||}$ axis. The phase space density contours show no loss cone feature and are very elongated along the $v_{||}$ axis up to about $v_{||} = 15000$ km/sec (or 800 eV). Figure 5b therefore cannot be explained by a simple potential drop that increases monotonically from the magnetosphere to the ionosphere.

The type 2 counterstreaming electron event is distinguished from type 1 events in several respects. First of all, the electron distribution function has beam-like structure. Second, the electron energy flux lacks a hot component (>1 keV). Finally, the ion energy fluxes observed during the type 2 event have pitch angles near 175° , much closer to the magnetic field direction than those of the conic ions detected in the type 1 events. The type 2 event may have been observed by the S3-3 satellite, since S3-3 occasionally detects energy spectra with beams during counterstreaming electron events (Sharp et al., 1980).

One unusual feature of type 2 counterstreaming electrons is the elongation of the phase density contours along the $v_{||}$ axis (see Fig. 5b). The elongated contours can be interpreted as electron beams reflected by a potential barrier. The HAPI measurement therefore suggests an upward electric field above the satellite and a downward electric field below the satellite. To produce such an oppositely-directed electric field, we suggest V-shaped potential contours imbedded with a potential island (valley). A schematic illustration is given in Fig. 6. This potential profile could explain the decrease of ion beam energy if the satellite passed through the transition region between the potential island and the V-shaped potential as shown in Fig. 6.

DE-1 HAPI ELECTRON DISTRIBUTION CONTOURS

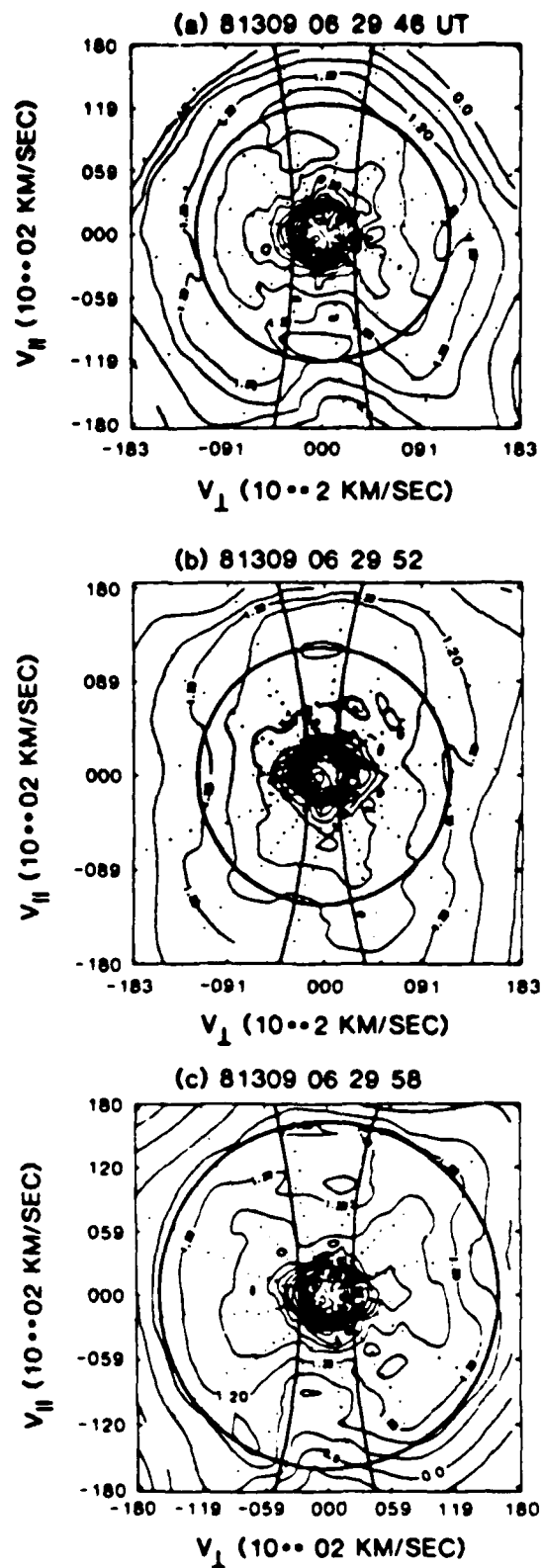


Figure 5. Electron phase space density contours (a) before, (b) during and (c) after a type 2 counterstreaming electron event.

Sharp et al (1980) suggested another interpretation of counterstreaming electrons in terms of a double layer with a potential drop of about 1 keV flickering its polarity about every 1 millisecond. To account for the HAPI observation, we estimate the flickering period to be at least 50 milliseconds since the counterstreaming portion of the electron spectra was detected successively for three energy steps. Low altitude satellite observations of auroral particle fluxes have not yet suggested flickering double layers of such long periods.

The observed sequence of the type 2 event presented in Figure 5 could be interpreted either as a spacecraft horizontally crossing a V-shaped potential structure or as a vertical motion of the structure passing the spacecraft along magnetic field lines toward the ionosphere. If DE-1 were detecting a spatial structure, the transverse width of the potential island could be as narrow as 16 km along the satellite path which corresponds to a North-South distance of about 1 km at the ionosphere. On the other hand, if DE-1 were detecting temporal variations, the potential island would be very transient, lasting only about one satellite spin period.

Potential contours with an island structure have recently been found in a computer simulation of two-dimensional double layers in which the effects of magnetic mirror force, trapped electrons and background plasmas are included (Wagner, 1980; Wagner et al., 1981). Recent laboratory experiments on double layers also indicate a similar structure (Iizuka et al., 1982). The condition for producing such a potential structure is not clear, although computer simulations by Wagner (1980) suggest strong wave trapping due to the Buneman instability. We notice that the potential profile in Figure 6 is very similar to the magnetic field and electric potential overshoots of the earth's bow shock which arise from reflections of a portion of the solar wind ion population (Russell and Greenstadt, 1979; Leroy et al., 1981). This analogy might be applied to the present case if we speculate that the potential well in Figure 6 is caused by reflection of ionospheric electrons.

Finally, we note that the width of the loss cone shown in Figures 5a and 5c is energy dependent (about 33° at 738 eV and about 40° at 416 eV). These loss cone widths are found to agree with the presence of a potential drop below the spacecraft according to the formula (Sharp et al., 1979)

$$\alpha = \sin^{-1} (B_s (E + eV) / B_i E)^{1/2} \quad (2)$$

where E is the energy, eV is the potential, B_s and B_i are the magnitudes of the magnetic field at the locations of the satellite and the top of the ionosphere respectively.

C. Correlative Observations of Counterstreaming Electrons

1. Plasma Measurement

The plasma data obtained by the High Altitude Plasma Instrument (HAPI) [Burch et al, 1981] on DE-1 are shown in Figures 12-16 for 18 September 1981 (day 261). Figure 12 is a spectrogram of electron energy fluxes for a 26-minute time interval from 2128 to 2154 UT. The top panel shows electron energy fluxes at 0° pitch angle (downward), and the bottom spectrogram shows electron energy fluxes at 90° pitch angle. The vertical scale is energy in a

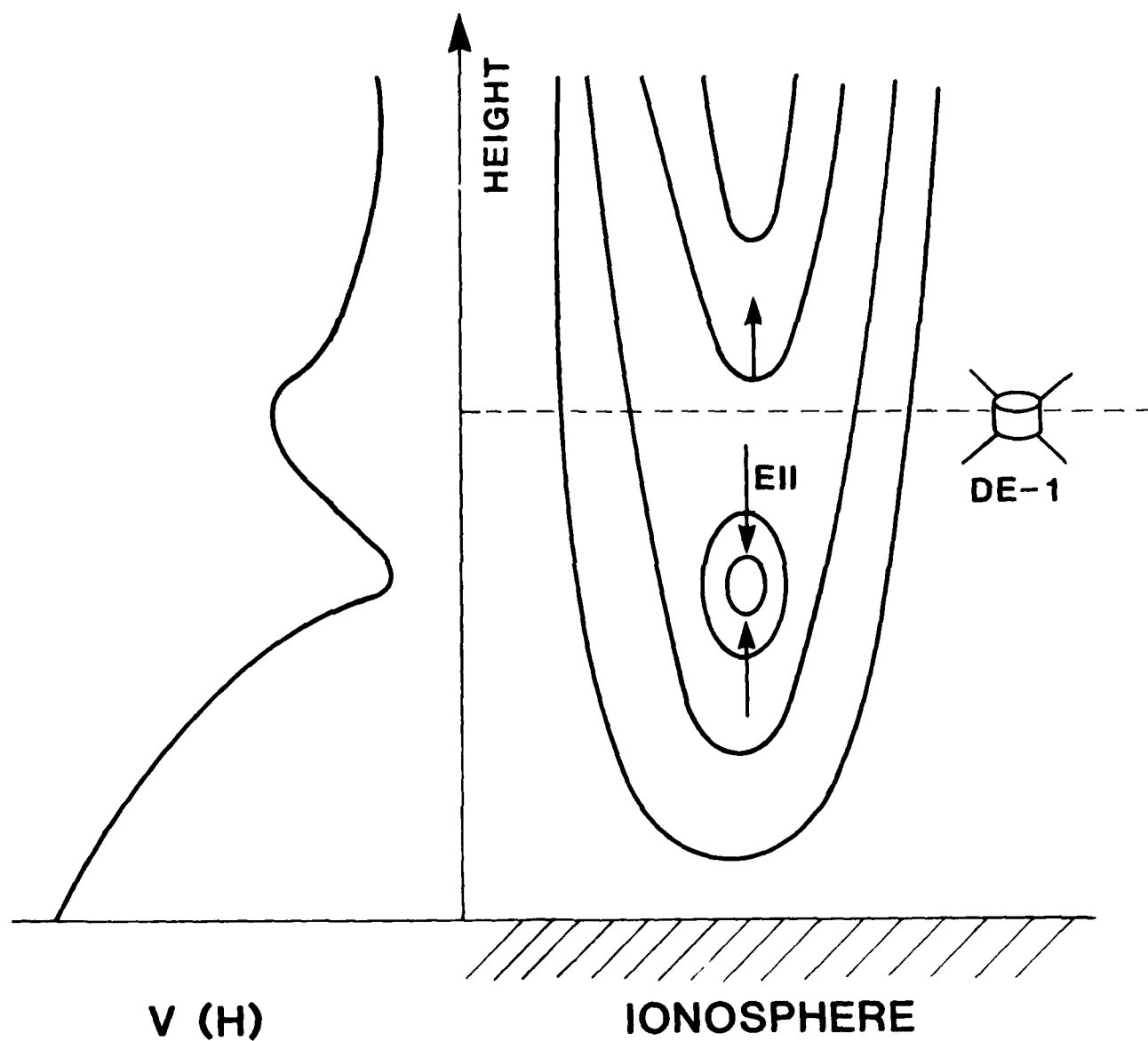


Figure 6. Schematics of V-shaped potential contours with a potential island.

logarithmic scale, and the horizontal scale is UT. The energy fluxes measured at both pitch angles were enhanced after 2133 UT, indicating that DE-1 encountered a plasma injection boundary. At this time, the spacecraft was at 67° invariant latitude, 2400 (MLT) and 14,000 km altitude, and moving equatorward near the midnight meridian plane. A second enhancement of energy flux occurred after 2146 UT. The energy flux remained at high levels until the data gap at 2154 UT.

This summary spectrogram shows two distinct populations of electron fluxes. At energies around several keV are the energetic precipitating electron fluxes that are believed to originate in the plasma sheet. At lower energies, from 10 to several hundred eV, enhancements of energy fluxes were detected sporadically around 2135, 2139, and 2148 UT. These low energy electron fluxes are enhanced in the field-aligned direction because the observed energy flux was larger at 0° pitch angle (top panel) than at 90° pitch angle (bottom panel). These enhanced electron fluxes in the field-aligned direction are similar to those observed at synchronous orbit during plasma injection events [Lin et al., 1979; Moore and Arnoldy, 1982].

In Figure 8, we show the electron density and energy flux integrated from 18 eV to 10 keV over the whole pitch angle range. Before the plasma injection around 2133 UT, the number density was about 1 cm⁻³ and the integrated energy flux was about 1 ergs/cm²-s. After the injection, the number density increased to about 10 cm⁻³ and the integrated energy flux increased to 10 ergs/cm²-s. Electrons with energy less than 1 keV contributed about 10% of the integrated energy flux and about 70% of the number density. Around 2148 UT, the integrated energy flux reached a peak value exceeding 100 ergs/cm²-s. We found this plasma injection event to be the most intense in the HAPI data that have been processed so far. The three-hour Kp index during this time was 6-.

The electron and ion energy fluxes for the full pitch angle range (0°- 180°) are presented in Figure 9 for one counterstreaming electron event during 2147-2150 UT. The DE-1 altitude in this time interval was about 11400 km. The energy fluxes shown are spin-modulated with a period of 6 seconds. The electron spectrogram (top panel) shows bright vertical stripes below 1 keV, indicating an enhancement of energy flux in that energy range. The center panel, which displays the detector pitch angle, shows that the detector measured enhanced energy fluxes only near 0° and 180°. Hence the measured low energy (<1 keV) electrons were counterstreaming along field lines. This counter streaming electron event is classified as type 1, because energetic electron fluxes above 1 keV were simultaneously detected.

Ion fluxes from approximately 10 to 100 eV were detected at the same time that counterstreaming electrons were observed (see the bottom panel of Figure 9). In conjunction with the enhancement of energetic electron fluxes, the energy of conic ions increased from about 10 eV to about 100 eV. These ion fluxes are identified as conic ions because their pitch angles lay between 110° and 160°. The absence of field-aligned ion fluxes suggests that the observed conic ions are not accelerated by parallel electric fields below the spacecraft.



Figure 7. Energy-time spectrograms of electron energy fluxes at 0° pitch angle (top) and 90° pitch angle (bottom).

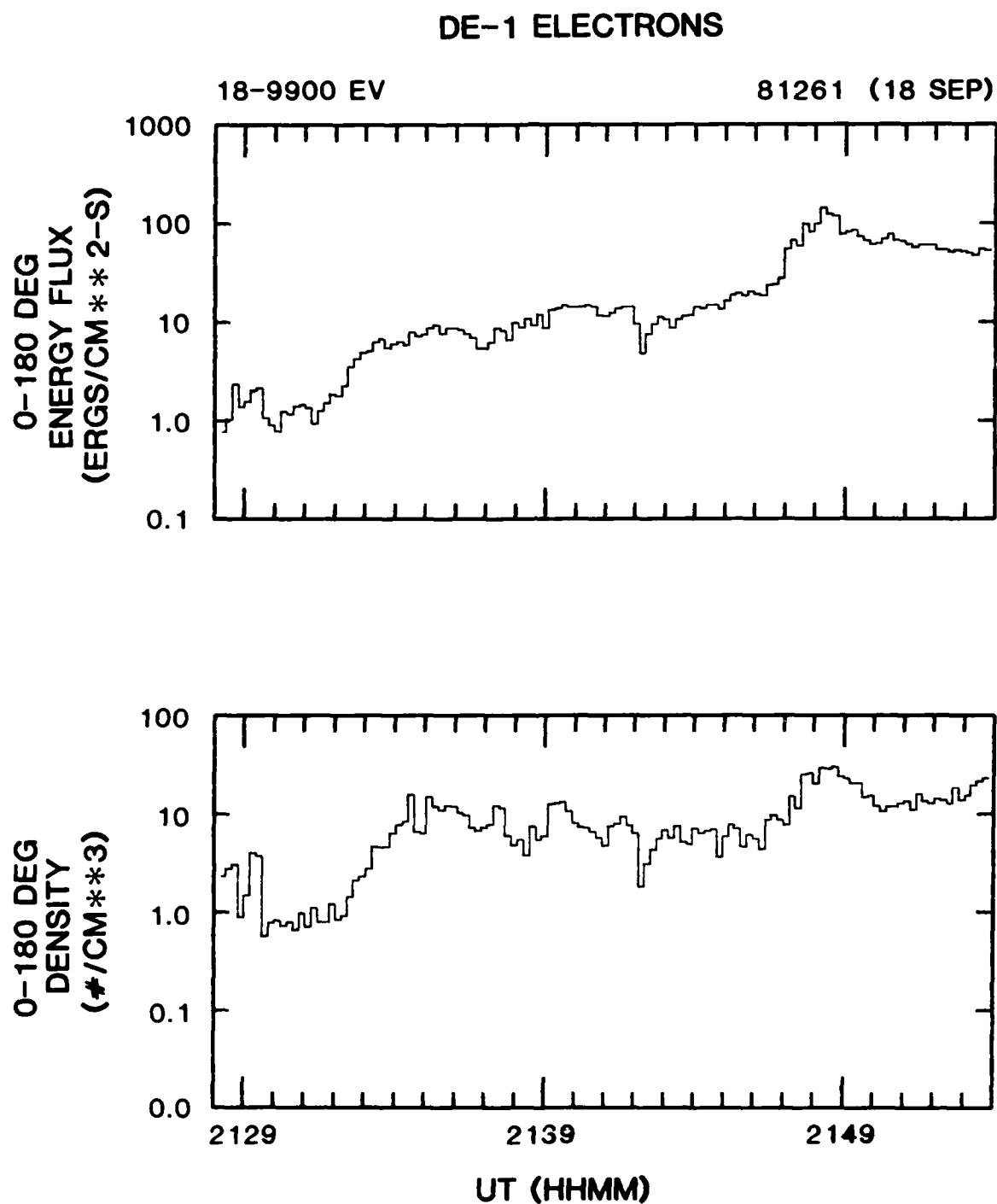


FIGURE 8. Number density and total energy flux integrated from 18 to 10,000 eV over the whole pitch angle range.

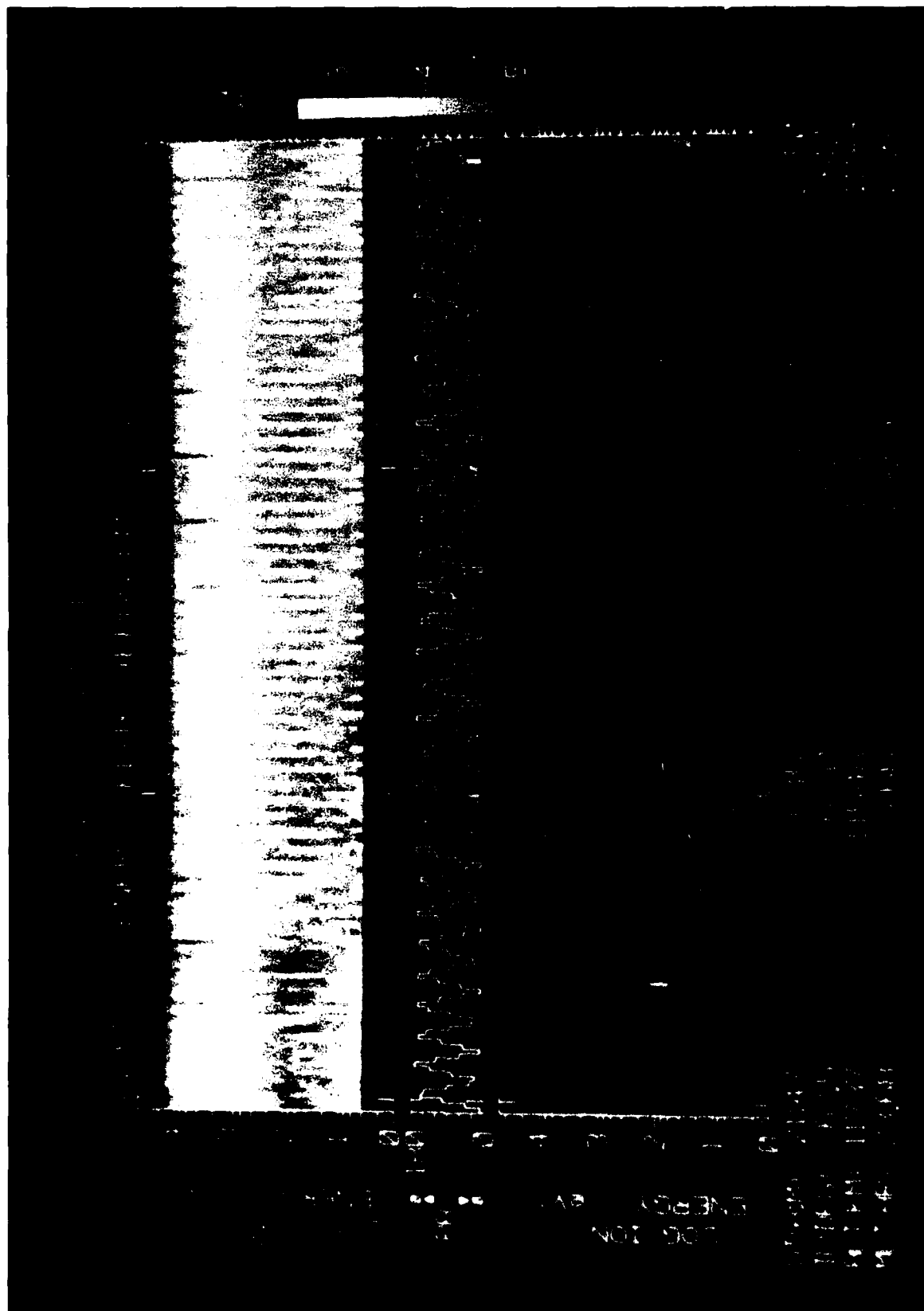


Figure 2. Energy-time spectrogram of electron (top) and ion (bottom) energy fluxes. The detector's pitch angle is plotted in the center panel.

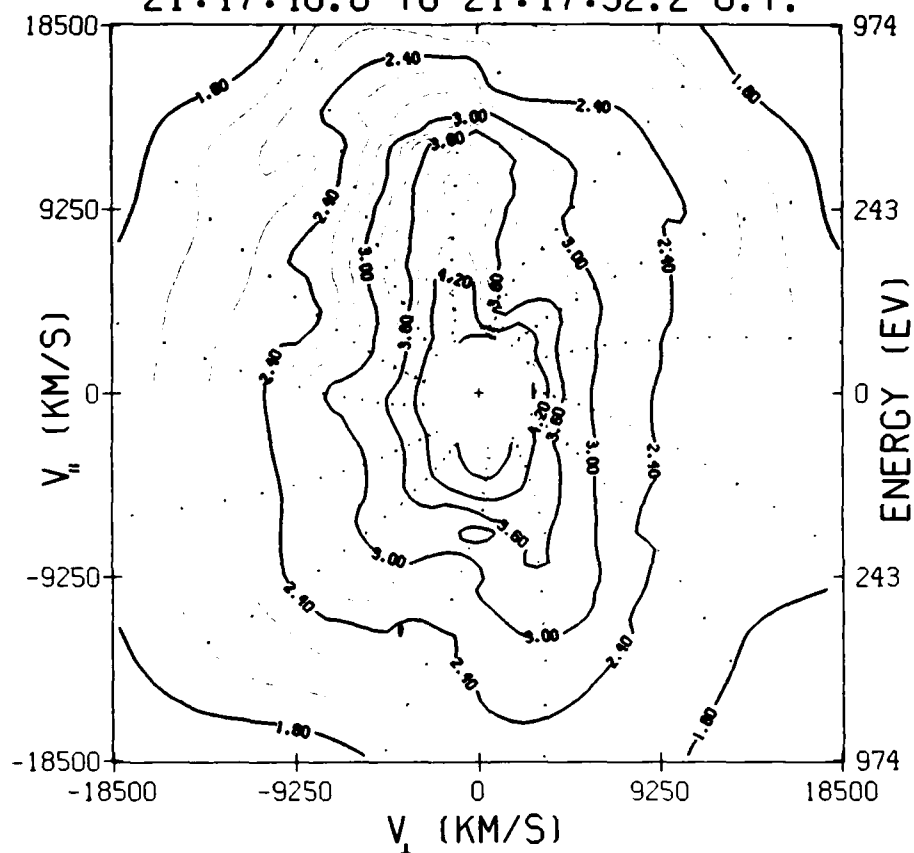
In Figure 10, we present contours of constant distribution function for a 12-second interval (2147:40-2147:52 UT) during which the counterstreaming electron flux was intense. The contour plots are prepared from a two full spin period of data. The locus of the sampled data in the phase space starts at the upper right corner and is shown as dot. The contours at energies less than 1 keV are elongated along the V_{\parallel} axis. An island contour at $V_{\parallel} \approx 9250$ km/s indicates a downward-moving beam at an energy of about 250 eV (positive velocity downward). As in this case, electron beams are sometimes found when counterstreaming electron fluxes are intense. But when counterstreaming electron fluxes are weak, electron beams are generally not observed. Because the plasma data are dominated by spacecraft photoelectrons below 15 eV, we cannot determine whether counterstreaming electrons have a beam energy less than 15 eV.

In Figure 11 we show two consecutive contour plots of constant distribution function that might be considered as representative for counterstreaming electron events. The two contour plots are in time sequence, and each plot is composed of the plasma data during a two-spin period. The consistent feature is that the contours are elongated along the V_{\parallel} axis. Figure 11 differs from Figure 10 in that the contours do not show electron beam. In general, electron beams are found only when counterstreaming electron fluxes are intense. Figure 11 also shows that the contours are less elongated than the contours shown in Figure 10 which covers a time period about 10 seconds earlier. This result suggests that the angular width of field-aligned electron fluxes can vary in time. From the intersections of contours of constant distribution with the two velocity axes, we note that the contours in Figure 16 are slightly more elongated in the direction of positive velocity (toward the ionosphere). From a survey of contour plots, we conclude that the counterstreaming electron fluxes can be slightly enhanced in either upward or downward direction.

The magnetic field measurements during the counterstreaming electron events on day 261, 1981, are shown in Figure 12. The magnetic field instrument was described in detail by Farthing et al., [1981]. The earth's internal field has been subtracted from the observed magnetic field. The residual field components were then transformed into DBR, DBTHETA, and DBPHI in geomagnetic dipole coordinates, where DBR is on the radial direction. DBTHETA is perpendicular to the radius of the meridian plane, and DBPHI points toward the west. The magnetic field data plotted is 1/2-second averaged. The magnetic field disturbance, which was mainly in the DBPHI component, began around 2132 UT.

2. Magnetic Field Measurements

Figure 7 indicates three counterstreaming electron events occurring in the intervals 2134-2136, 2138-2140 and 2147-2150 UT. Magnetic field perturbations in the azimuthal direction were associated with these three events. During the counterstreaming electron event (2147-2150 UT), DBPHI decreased by 200 nT in 20 seconds starting from 2147:15 UT (Figure 12). This steep decrease of DBPHI represents field-aligned currents flowing into the ionosphere. From 2148 to 2149 UT, DBPHI slowly recovered to its unperturbed value. The energy flux of counterstreaming electrons was most intense (2147:30 -2148 UT) when DBPHI was at its minimum, rather than at its steep gradient.

DISTRIBUTION CONTOURS LOG F (SEC³/KM⁵)

```

LAT (DI) 62.1
MLT (MA) 23.7
ALT (KM) 11572
GLAT (DI) 40.3
GLONG (DI) 16.2

```

VPR (KM/S)	PC (MMOS)	HC (MMOS)
5.69E+01	N/A	N/A

FIGURE 10. Phase-space density contours of the logarithm of the electron distribution function. A downward electron beam is displayed as a contour island centered on the positive V_{\parallel} axis.

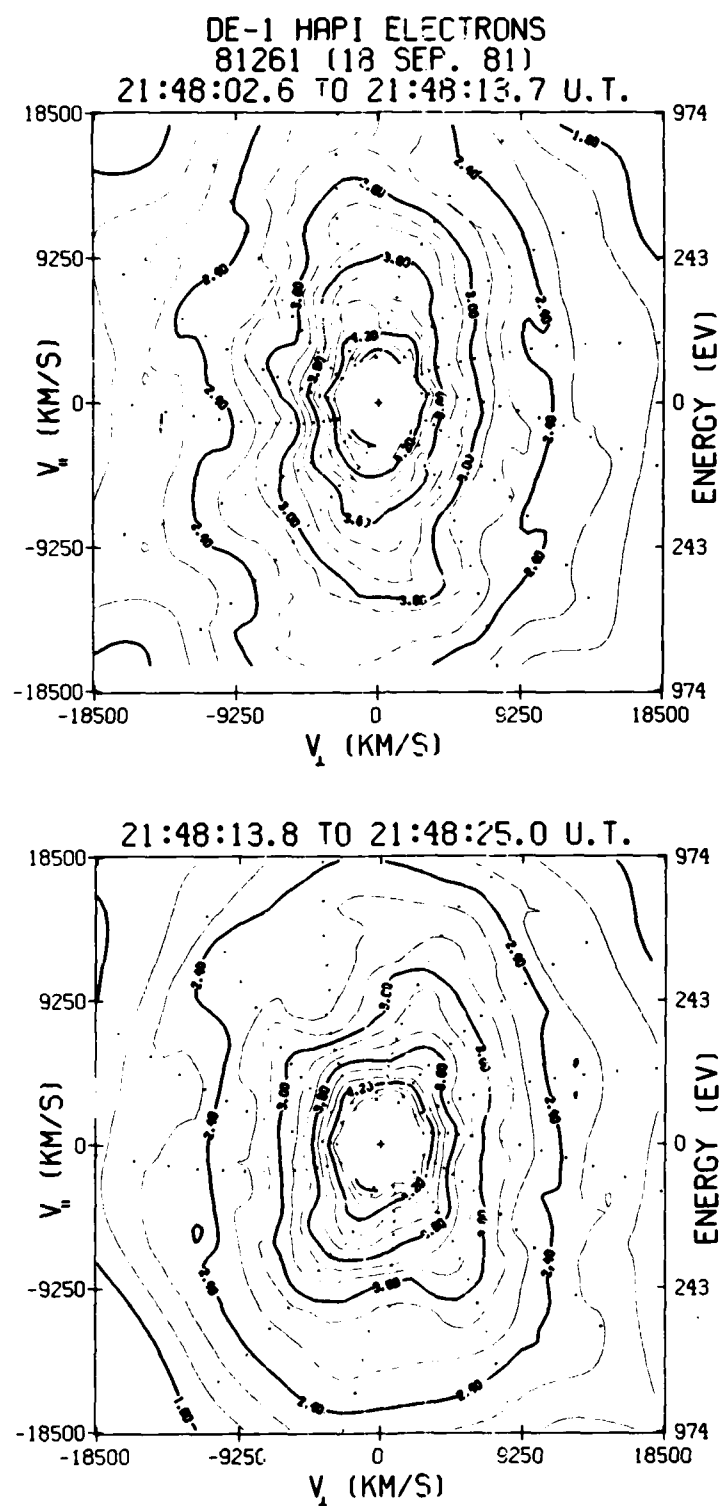


FIGURE 11. Phase-space contours of constant distribution function during a type-1 counterstreaming electron event.

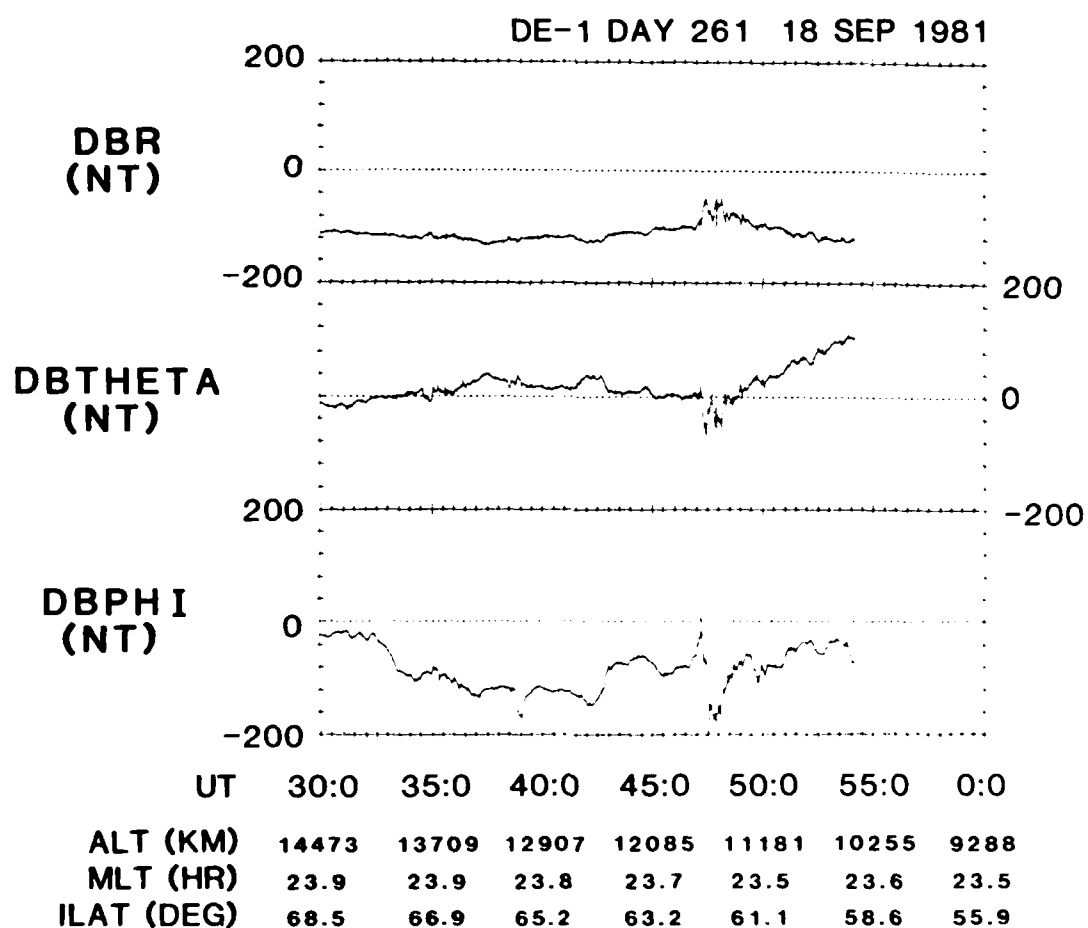


FIGURE 12. Three components of magnetic fields for the DE-1 pass shown in Figure 1.

3. STARE Measurements

On this pass, DE-1 was magnetically conjugate with STARE. STARE's geographic longitude is 16° east, very close to the DE-1 orbital plane. The STARE radars recorded the intensity and Doppler shifts of radio waves scattered by E-layer electron density irregularities [Nielsen and Greenwald, 1979]. By combining the Doppler shifts observed from two separate radars, one then estimates the electron $\underline{E} \times \underline{B}$ drift velocity of the E-layer irregularities.

Figure 13 illustrates the latitudinal profile of electron drift velocities observed by the STARE system from 2120 to 2143 UT. The electron drift velocities are plotted in a format that has geomagnetic latitude as the vertical coordinate and UT as the horizontal coordinate. Each vector represents a one-minute average of radar measurements. The electron drift velocity started to increase at about 2130 UT in the region equatorward of 68° geomagnetic latitude, about three minutes before the plasma injection boundary was detected by DE-1. Because DE-1 was slightly southward of STARE, this observation can be interpreted by an equatorward motion of the plasma injection boundary. Since most drift vectors were directed eastward, the electric field ($\underline{E} = -\underline{V} \times \underline{B}$) was directed equatorward. This suggests that a Pedersen current was flowing in the equatorward direction. The magnitude of the Pedersen current increased with latitude because the drift velocity increased with latitude. The increase of Pedersen current with latitude suggests an upward field-aligned current flowing in the observation area of STARE after 2130 UT.

The field-aligned current density is estimated from STARE data. Assuming a homogeneous Pedersen conductivity of 1 mho, we estimate that the upward field-aligned current density at 2133 UT was about $0.1 \mu\text{A}/\text{m}^2$. At 2148 UT, the field-aligned current was upward but flanked by downward currents. The magnitude of field-aligned current density is estimated to be about $0.4 \mu\text{A}/\text{m}^2$ for a homogeneous Pedersen conductivity of 1 mho. Due to uncertainties on the electric field magnitude derived from STARE data, the current density estimates are very rough. However, the directions of field-aligned current deduced from STARE are usually reliable.

4. Ground Magnetograms

The H-components recorded by five ground magnetograms in the northern auroral zone are shown in Figure 14. These magnetograms indicate that a magnetic substorm started around 1940 UT at the stations in Scandinavia. Near 21 hr UT, all magnetograms recorded active magnetic disturbances. According to the Abisko and Tromso stations at about 2° east of the DE-1 orbital plane, the H component began to recover after 2130 UT and returned to its pre-substorm value after 22 hr UT at Tromso and after 23 hr UT at Abisko. We conclude that the plasma injection event observed by DE-1 occurred during the recovery phase of a magnetic substorm.

5. Computation of Current Density

We compute field-aligned current density from the magnetic field data and from the plasma data. Assuming a series of field-aligned infinite current layers that are locally normal to the dipolar meridian plane, the

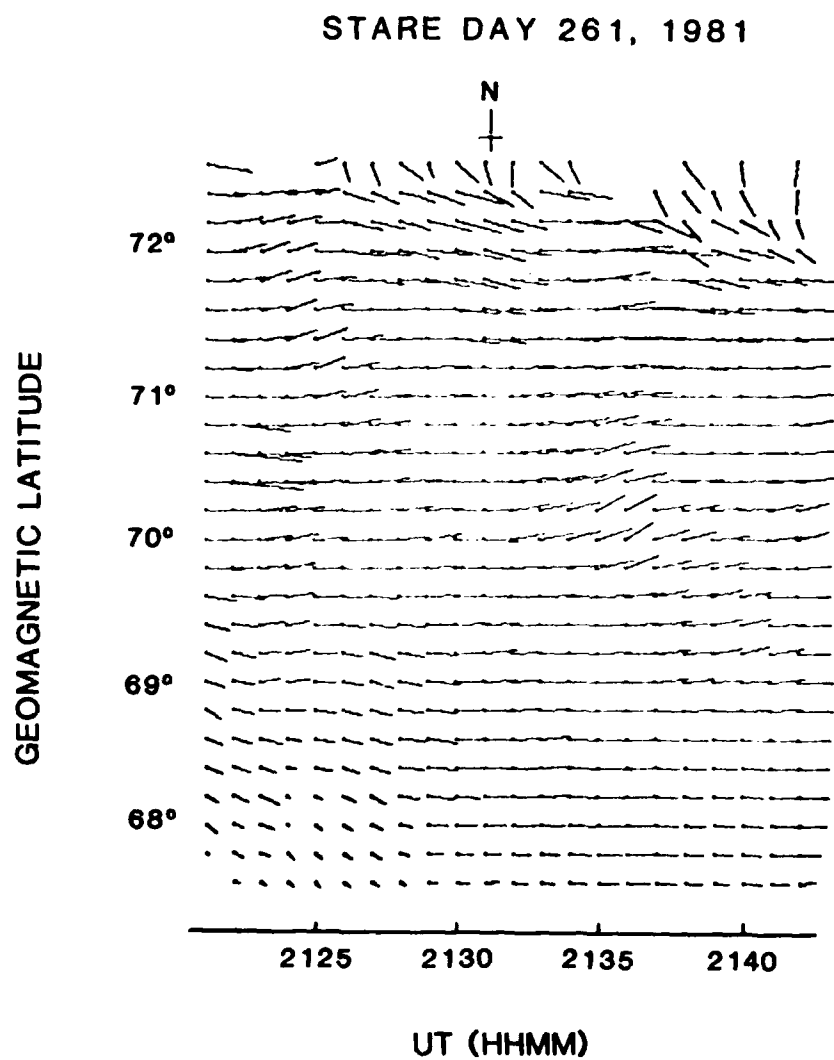


FIGURE 13. STARE latitudinal profile of electron drift velocities versus time on day 261, 1981.

azimuthal (east-west) component of the magnetic field DBPHI is differentiated to yield the current density. The differentiation of the magnetic field is made with respect to the distance normal to the current sheets. From the measured electron distribution $f(v, \alpha, \phi)$, the field-aligned current density is calculated by

$$I = e \int_0^{2\pi} \int_0^\pi \int_{v_{\min}}^{v_{\max}} v_{\parallel} f v_{\perp} dv d\alpha d\phi \quad (3)$$

where α is pitch angle, e is electron charge, v_{\parallel} and v_{\perp} are the velocities parallel and perpendicular to magnetic field B , v_{\min} and v_{\max} are the velocity limits on the measurement, and d is the azimuthal angle about B . We set v_{\min} equal to the velocity of an 18 eV electron to avoid the spacecraft photoelectrons, and set v_{\max} equal to the velocity of a 10 keV electron. The time interval to acquire the electron distribution function over the whole pitch angle range is 6 seconds for the normal mode operation of the plasma instrument.

Figure 15 illustrates the current density computed for the interval corresponding to Figure 9. The current density computed from plasma data is given in the top panel and the current density computed from magnetic data is given in the center panel. The azimuthal component of the magnetic field is also presented at the bottom panel for comparison. The plasma data suggest a downward current density with a peak value of $1.5 \mu\text{A}/\text{m}^2$ occurring at 2147:15 UT. The peak current density derived from the magnetic field data is about $2 \mu\text{A}/\text{m}^2$. Integrated over the current layer, the total current densities deduced from both methods are in good agreement and are approximately 0.1 A/m within 10%.

The magnetic field data indicate upward currents on both sides of the downward current with a peak current density around $0.5 \mu\text{A}/\text{m}^2$. This current density is consistent with the estimate based on the STARE data, but the plasma data suggest a large upward current around 2148 UT with a peak density of about $5 \mu\text{A}/\text{m}^2$, about ten times larger than current density computed from the magnetic data. The disagreement could mean that the upward current was a filament or that the upward plasma current was partially neutralized by cold electrons moving in the upward direction.

The contribution of field-aligned current density by counterstreaming electrons was investigated statistically. We surveyed the available DE-1 plasma data that have been processed so far, and found a total of 18 counterstreaming electron events. These events were observed in the evening auroral zone, where their magnetic local times were between 20 and 24 hr, and their invariant latitudes varied from 60° to 72° . These events occurred at altitudes between 9000 km and 14500 km.

We computed differential current density below 235 eV, $I(<235 \text{ eV})$, and the total current density, I_{total} , from the plasma data. The stepped energy of 235 eV was chosen as the threshold because the energy of counterstreaming electrons is found to be less than 250 eV for most events.



FIGURE 14. Ground magnetograms in the northern auroral zone on 18 September (day 261), 1981.

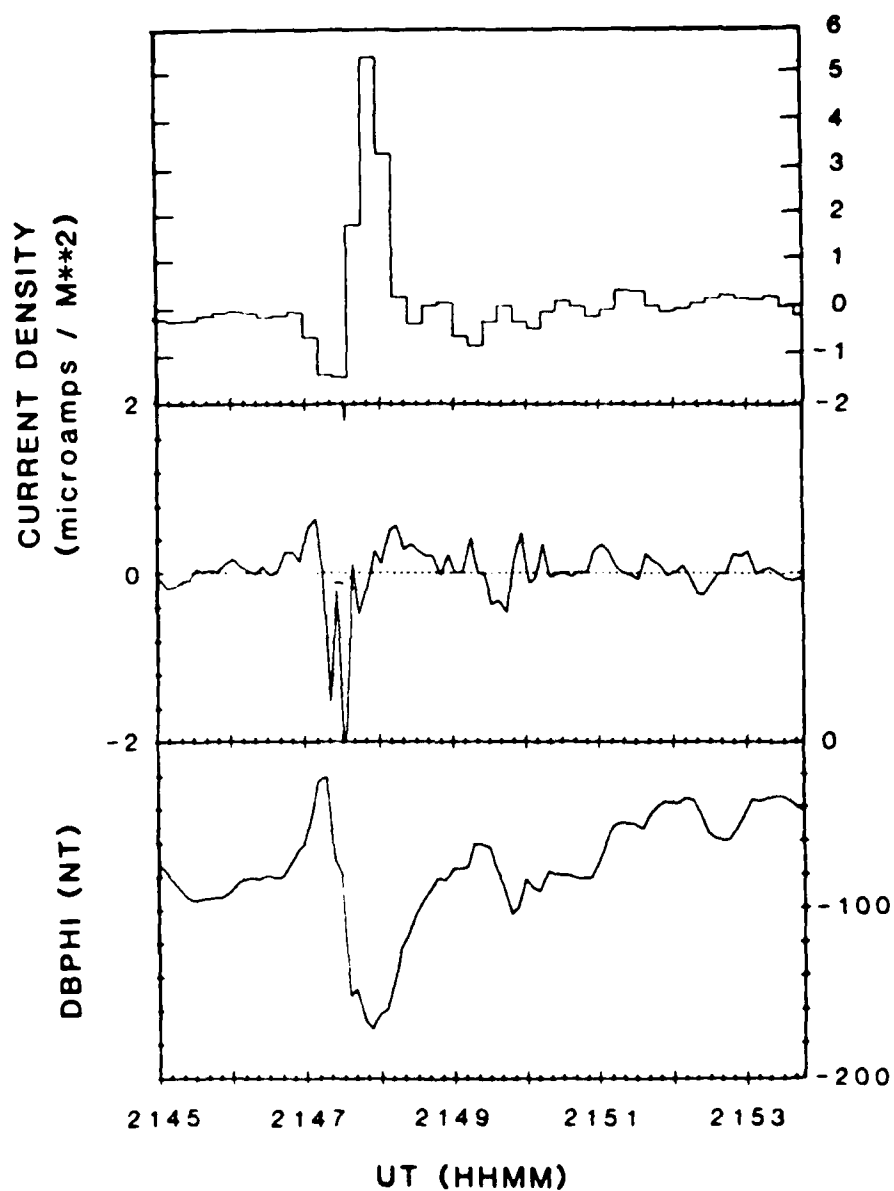


Figure 15. Comparison of the current density deduced from the plasma data (top) and the current density deduced from the magnetic field data (center). The bottom panel gives the azimuthal magnetic field component from which the current density was deduced.

The survey of S3-3 data also indicates that 70% of electron beams were detected below 240 eV [Collin et al., 1982]. The largest current density found was $5 \mu\text{A}/\text{m}^2$ on day 81261. Most counterstreaming electron events had a total current density less than $2 \mu\text{A}/\text{m}^2$. The total current density was smaller than $0.25 \mu\text{A}/\text{m}^2$ for only two events. For those events with I_{total} greater than $0.25 \mu\text{A}/\text{m}^2$, we plot the ratio $I(<235 \text{ eV})/I_{\text{total}}$ versus I_{total} in Figures 16 and 17. For the downward current (open circle), $I(<235 \text{ eV})$ was greater than 40% of the total current density (Figure 16). For the upward current (solid circle), $I(<235 \text{ eV})$ was smaller than 50% of the total current density (Figure 17).

6. Energy and Pitch Angle Distributions

In this section, we examine the properties of electron distribution functions during type 1 counterstreaming electron events. We present line plots of distribution functions with small pitch angles ($<25^\circ$) in the energy range of 20-1000 eV during the interval from 2147:30 to 2149 UT (Figure 18). To the first order approximation, these distribution functions can be represented by Maxwellian functions, but weak electron beams with energy less than 200 eV were also detected, most distinctly in Figure 23b, c, and g. These electron beams moved in the downward direction and were observed in the region of upward field-aligned currents (Figure 20). The distribution functions for electrons with pitch angles greater than 155° for the interval 2147 -2149 UT are shown in Figure 19. Only two out of the eight distribution functions shown contain weak electron beams with energies around 300 eV (Figure 19 and c). These upward electron beams appeared to be insignificant in determining the direction of field-aligned current because they were detected in the region of upward field-aligned currents (Figure 15).

D. Conclusions

Type 1 counterstreaming electrons are apparently the type of electron event first reported by Sharp et al. (1980), and may be related to the field-aligned electron beams observed by the ATS-6 satellite at synchronous orbit during substorm injections (Lin et al., 1979; Moore and Arnoldy, 1982). Type 2 counterstreaming electrons are a new and unusual phenomenon that DE-1 has detected within acceleration regions. The main feature distinguishing these two types of event is that the electron distribution function of type 1 is composed of two Maxwellian distributions while the distribution function of type 2 is characterized by electron beams.

The presence of two distinct types of counterstreaming electron events indicates the possibility of two distinct mechanisms of electron acceleration operative at high altitudes in the auroral zone. Type 1 events appear to involve wave-particle interactions whereas type 2 events seem to result from direct acceleration by oppositely-directed electric fields pointing toward the satellite along magnetic field lines.

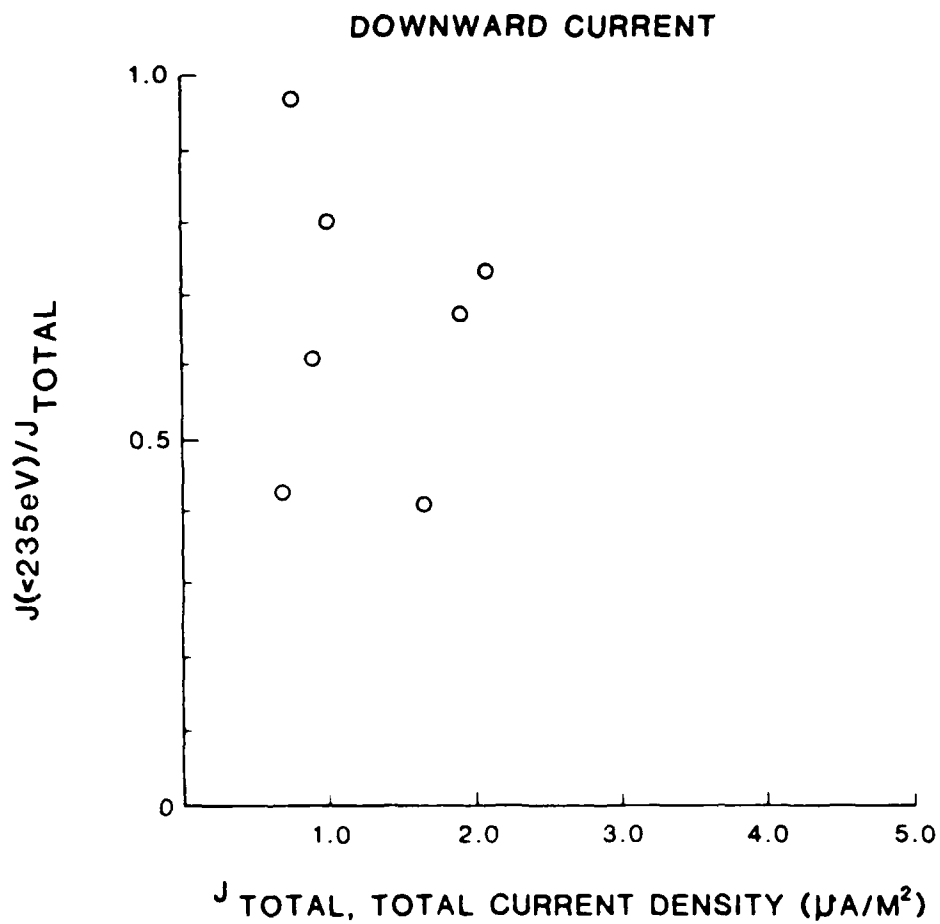


Figure 16. Ratio of current densities $I(<235\text{eV})/I_{\text{total}}$ versus I_{total} for downward currents. The current density $I(<235\text{eV})$ is integrated from the plasma data from 18 to 10,000eV.

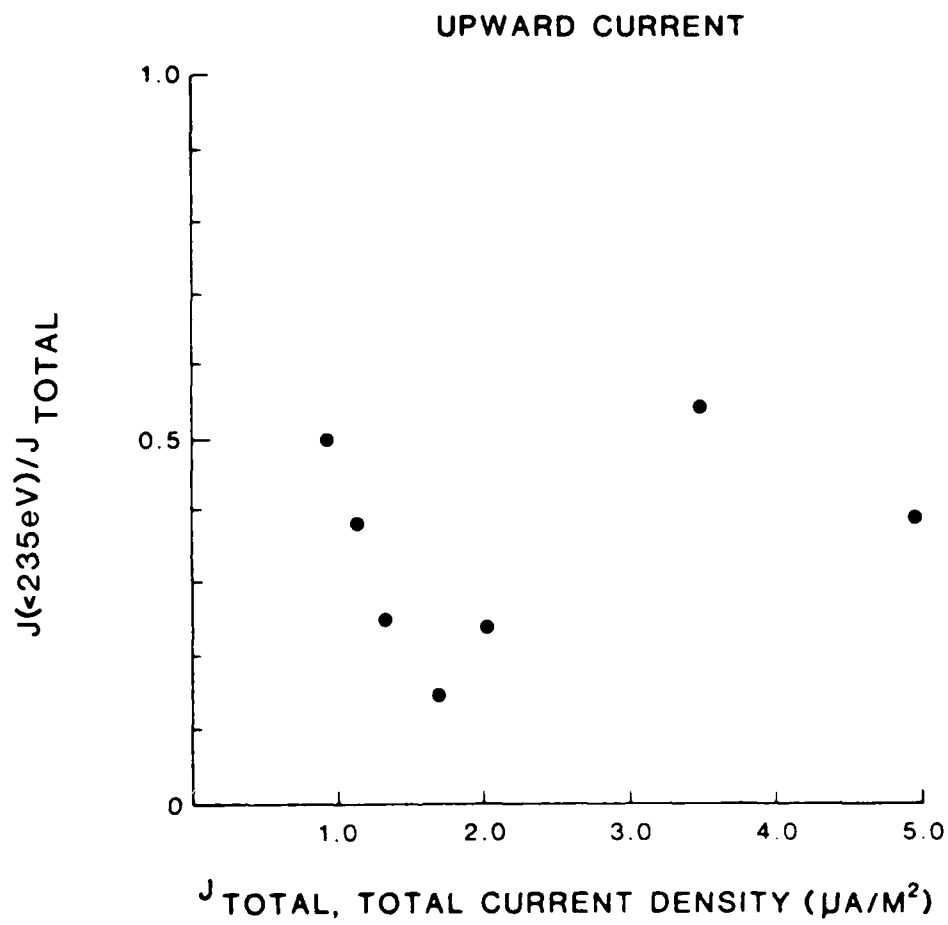


Figure 17. Ratio of $I(<235\text{eV})/I_{\text{total}}$ versus I_{total} for upward currents.

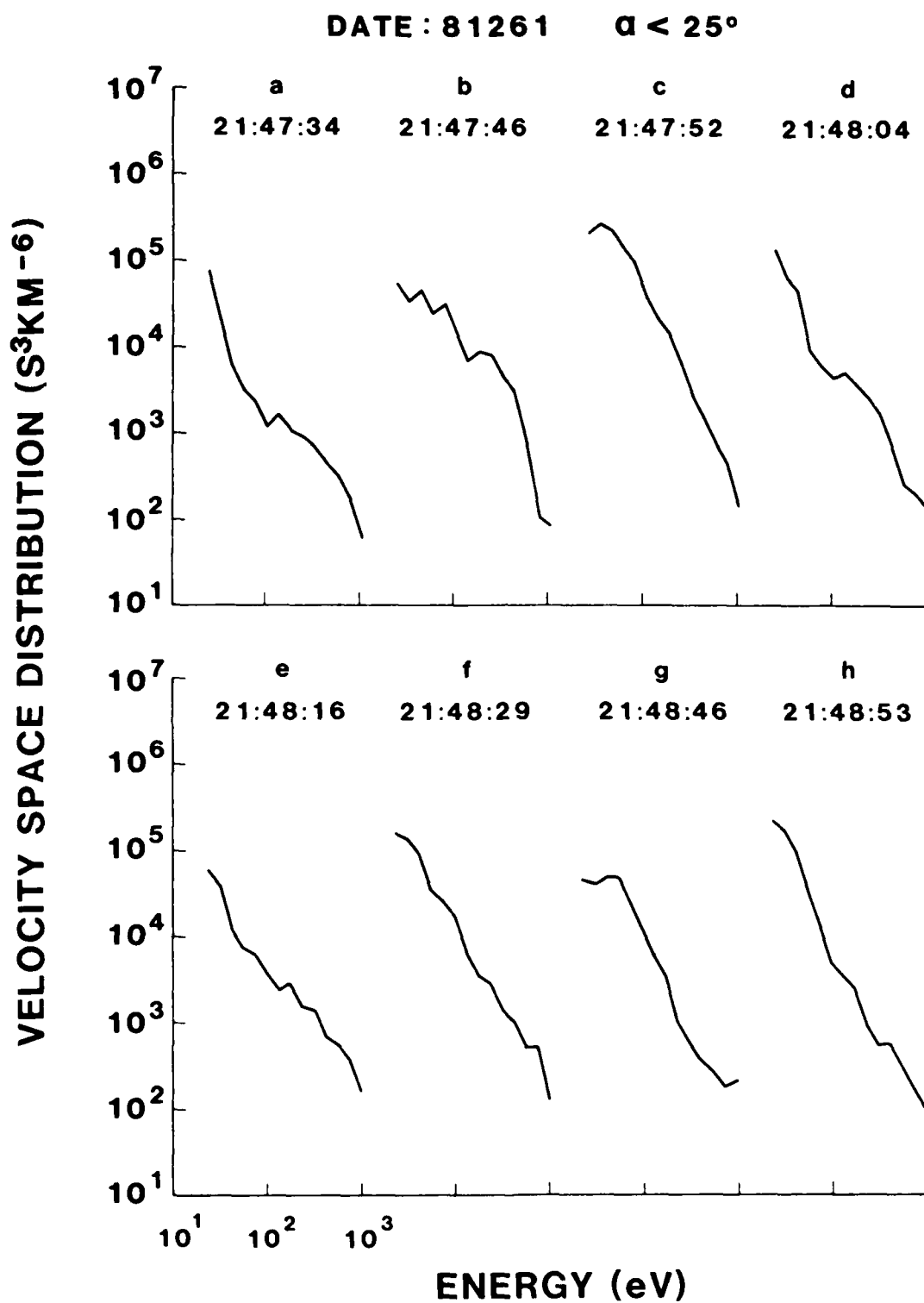


FIGURE 18. Electron distribution functions in the downward field-aligned direction.

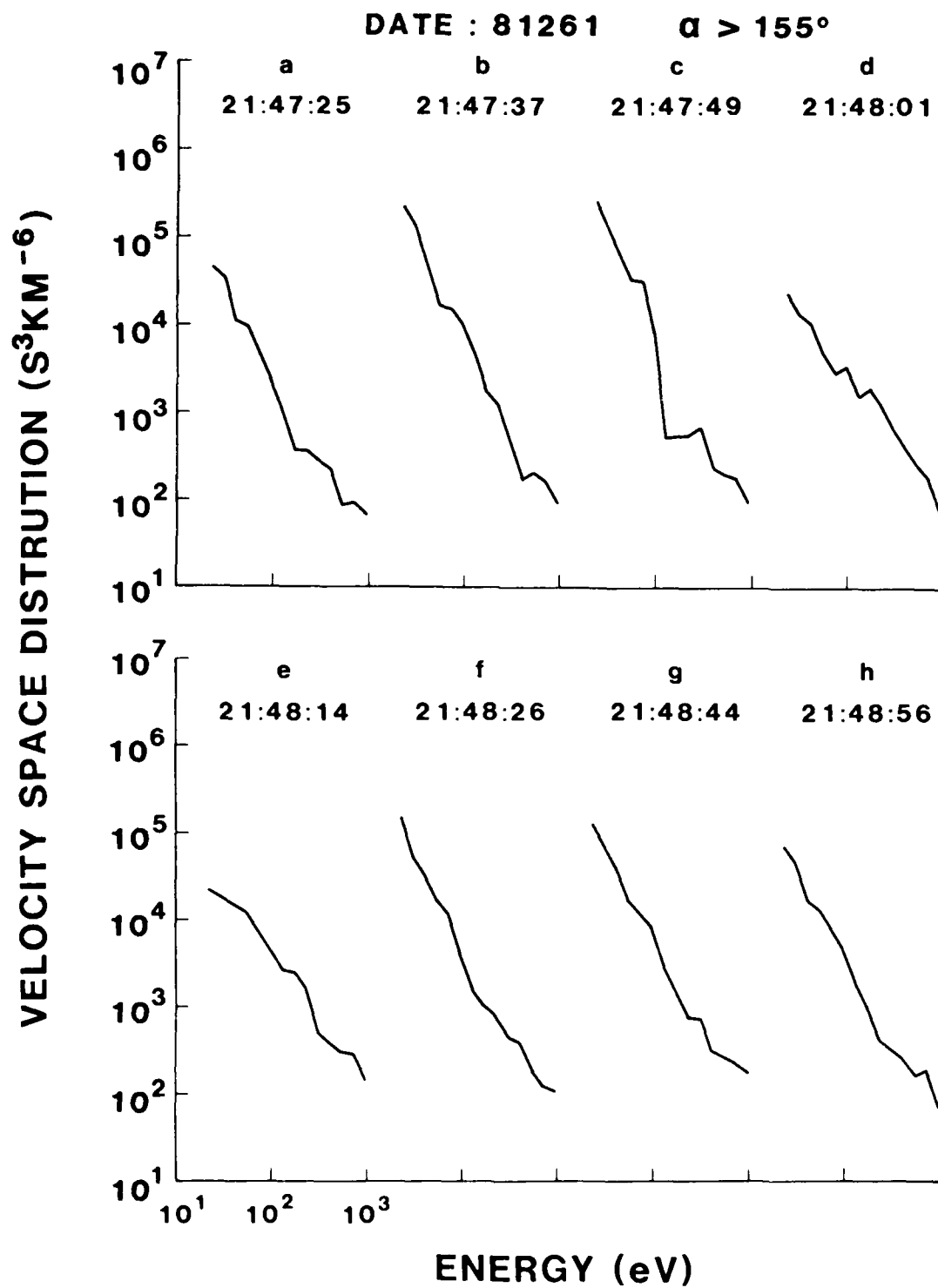


FIGURE 19. Electron distribution functions in the upward field aligned direction.

IV. UPWARD ELECTRON BEAMS

A. Introduction and Observations

The carriers of the large-scale Birkeland currents linking the ionosphere and the magnetosphere have typically been thought to be upward-moving thermal electrons in the downward-current regions and precipitating auroral electrons in the upward-current regions (Anderson and Vondrak, 1975; Klumpar, 1979). However, the problem is complex, and both populations can coexist in regions of upward or downward net current. For example, in the duskside plasma sheet where the current is typically downward, the upward flux of cold ionospheric electrons must be larger than that inferred from in situ magnetometer measurements, since it must also balance the upward current caused by the precipitation of energetic electrons. Similarly, intense auroral electron precipitation is often accompanied by upward fluxes of near-thermal and low-energy (50 eV) electrons whose current can balance roughly half of the primary upward current (Maier et al, 1980). These low-energy electrons are probably secondaries produced by the auroral beam itself (Evans, 1974; Pulliam et al, 1980).

Narrowly-collimated electron beams also can contribute significantly to the total current balance. Unlike the substantially isotropic auroral electron precipitation, downward beams are often seen at the edges of auroral arcs (Anderson, 1979), at energies below the parallel potential drop within "inverted V's" (Burch et al, 1979; Lin and Hoffman, 1979) and in the cusp (Zanetti et al, 1981). Upward-flowing and counter-streaming electron beams have recently been observed by Lin et al (1982) and by Sharp et al (1980). Sharp et al attributed their S3-3 results to fluctuating double layers, and reported that the width in pitch angle of the upward electron beams increases with increasing electron energy. We have found that this property is a consequence of a parallel potential drop below the spacecraft and that the amount of spread is related to the altitude of the top of the potential drop.

Similar upward electron beams were reported at lower (1400 km) altitudes by Johnstone and Winningham (1982) and by Klumpar and Heikkila (1982). The latter study showed that the upward beams were imbedded in a much larger region of downward Birkeland current. Using S3-3 data, Collin et al (1982) showed that the occurrence frequency of upward beams is roughly eight times higher above 6000 km than below 3000 km. Thus, one can infer a sporadic low-altitude mechanism and a more stable mechanism near $1 R_E$.

The DE-1 spacecraft is an ideal platform from which to study these phenomena for three reasons: (1) The spacecraft moves slowly enough through the acceleration regions that spin aliasing is not a problem, as it was in the Maier et al and Klumpar and Heikkila studies; (2) The apogee ($\sim 5 R_E$ geocentric) is high enough that effects from both the low-altitude and $\sim 1 R_E$ acceleration regions can be observed, as well as any regions in the $1-4 R_E$ altitude range; and (3) the presence of upward electron acceleration mechanisms below the DE-1 altitude brings the cold ionospheric electrons that carry the downward current at low altitudes up into the suprathermal energy range where they can readily be detected.

Upward electron beams have been observed at altitudes above 15,000 km on DE-1. These observations were made primarily near the equatorward edge of the morningside polar cusp (statistically a locus of downward current) and sporadically throughout the cusp region. Upward electron beams are seen all through the region of downward current, and the magnitude of the currents carried by the 15 eV to 17 keV electrons are more than adequate to reproduce the east-west magnetic perturbations measured concurrently in both the upward and downward current regions. The beams, as in other studies (Sharp et al, 1980; Klumpar and Heikkila, 1980; Collin et al, 1982), are associated with ion conics. The association of these beams with electrostatic hiss is established in another related paper (Lin et al, 1983).

The High Altitude Plasma Instrument (HAPI) on Dynamics Explorer 1 (DE-1) made differential flux measurements of electrons and positive ions over an energy/charge range of 5 eV/e to 31 keV/e. Details of the instrument and its various operating modes can be found in Burch et al (1981). For the first few months after launch the 4.7 R_E apogee of DE-1 was just poleward of the pre-noon polar cusp. A common feature of the HAPI plasma data acquired during this time period is the appearance of upward-travelling electron beams with energies from a few tens of eV to a few hundred eV. Although both upward and downward electron beams are observed in and near the cusp region, we have consistently observed a region of predominantly upward beams that overlaps the equatorward boundary of the cusp electron population.

The systematic appearance of upward electron beams near the equatorward cusp boundary, their absence in the heart of the cusp, and subsequent appearance near the cusp poleward boundary, raise the question of to what extent the electrons measured on DE-1 are charge carriers for dayside region 1 and cusp-region Birkeland currents. This question is answerable to some degree by suitable correlations between the HAPI data and data from the DE-1 magnetometer (Farthing et al, 1981). The results of the correlations for a typical pass are presented in the next section.

B. Electron Currents and Magnetic Perturbations

The parallel (field-aligned) current density carried by a measured electron distribution $f(v, \alpha, \phi)$ is given by

$$I_{\parallel} = e \int_0^{2\pi} \int_0^{\pi} \int_{v_{\min}}^{v_{\max}} v_{\parallel} f v v_{\perp} dv d\alpha d\phi, \quad (4)$$

where α is pitch angle, e is electron charge, v_{\parallel} and v_{\perp} are the velocities parallel and perpendicular to \underline{B} , v_{\min} and v_{\max} are the velocity limits on the measurement, and ϕ is the azimuthal angle about \underline{B} . Since the electron fluxes at energies below about 15 eV are dominated by spacecraft photoelectrons, we set v_{\min} equal to the velocity of an 18 eV electron (the next energy step above 15 eV) in the current calculations. In each case, v_{\max} was set to correspond to the maximum energy sampled by the HAPI instrument.

If the spacecraft potential ϕ_0 is nonzero, the above calculated current is an overestimate, since the measured electron velocity is larger than the actual velocity. For the analyzer viewing perpendicular to the spin axis (therefore also normal to the spacecraft surface) the velocity v in Eq. (4) should be replaced by $(v^2 + 2q\phi_0)^{1/2}$, where $q = -e$ for electrons (ions). For a potential ϕ_0 of roughly 15V, and a total potential drop of 30 V (magnetospheric and spacecraft), we can overestimate the current by no more than a factor of 2.8 and most likely less.

Calculation of the electron current was performed as follows. A differential current, dI/dv , was first obtained for each energy sampled by assuming a gyrotropic distribution and applying a spline integration over α . Next, the total current was obtained by integrating over v with the same technique. Ion current was also computed. However, in all cases the ion current amounted to less than 1% of the electron current.

The results of the current calculations for a cusp pass on October 6, 1981, are plotted in Figure 20, in which upward currents are plotted as positive values. Also plotted in Figure 20 are the currents determined from the magnetic perturbations (δB_z) measured by the DE-1 magnetometer, assuming current sheets that are greatly extended in longitude and oriented perpendicular to the local dipole magnetic meridian. The agreement between the computed and measured values of the current argues strongly that electrons with energies above 15 eV are the primary charge carriers of the downward region-1 currents, the upward cusp-region currents, and another region of downward current located near the poleward boundary of the cusp in the pre-noon hours at altitudes near 20,000 km. These same three current systems, and corresponding electron populations have been observed in all four cusp passes that we have examined in detail to date.

C. Acceleration Mechanism

Detailed study of the velocity-space distributions of the observed upward electron beams points to an acceleration region consisting of a downward field-aligned potential drop below the spacecraft. An example of the $f(v_{\parallel}, v_{\perp})$ distribution observed by the HAPI 0° analyzer on October 6, 1981, is plotted in Figure 21. To obtain optimum sampling in velocity space, Figure 21 contains $\log_{10} f$ contours for two successive spacecraft rotations. The dots in Figure 8 identify the $(v_{\parallel}, v_{\perp})$ values that were sampled by the 0° analyzer during the two rotations. To accentuate the features of the low energy beam, Figure 8 contains data only for energies up to 500 eV.

As shown by Knight (1973), conservation of energy and of the first adiabatic invariant require that electrons originating in the ionosphere satisfy the inequality where V_0 is the electrostatic potential difference between the ionosphere and the point of observation, and B_0 and B represent the magnetic induction at the top of the potential-drop region and at the point of observation, respectively. This inequality defines a region within a hyperbola with origin at (0,0) and "semi-axes" $\sqrt{(2e/m)V_0}$ (intercept along the v_{\parallel} axis) and $\sqrt{(2e/Am)V_0}$, where $A = (B_0/B) - 1$ (asymptotes $v_{\perp} = v_{\parallel}/A^{1/2}$). Shown in Figure 21 is such a hyperbola for a potential drop (V_0) of 31 V extending to a maximum altitude of 5870 km. The interior of this hyperbola, or one nearly like it, does in fact define approximately the region occupied by the upward electron beam. Examination of a number of upward beams shows that

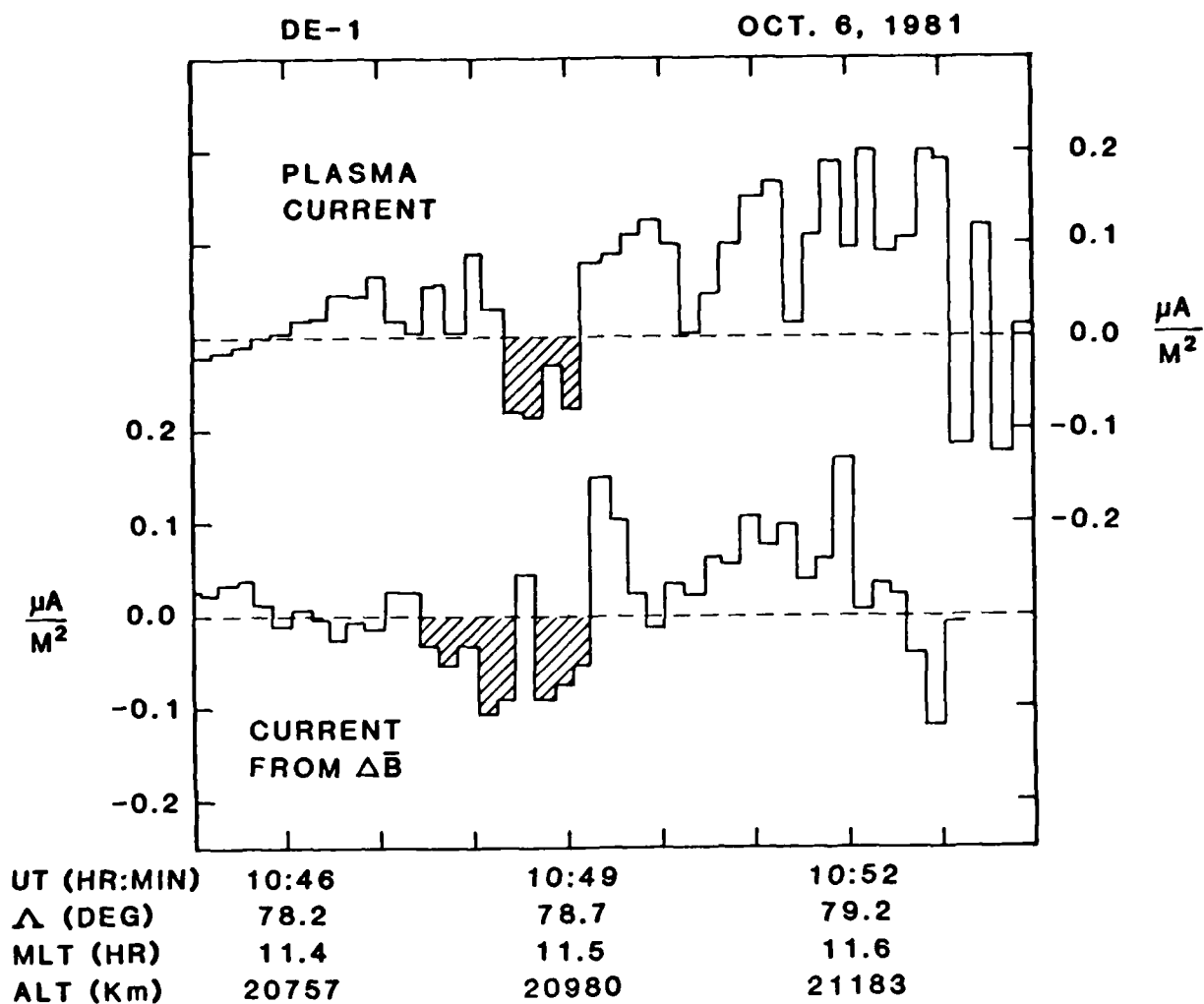


Figure 20. Field-aligned current densities computed from the measured hot-plasma distributions (top panel) and from the measured ΔB perturbations (bottom panel). Positive currents are upward, negative currents downward. The shaded regions of downward current are identified as region-1 Birkeland currents.

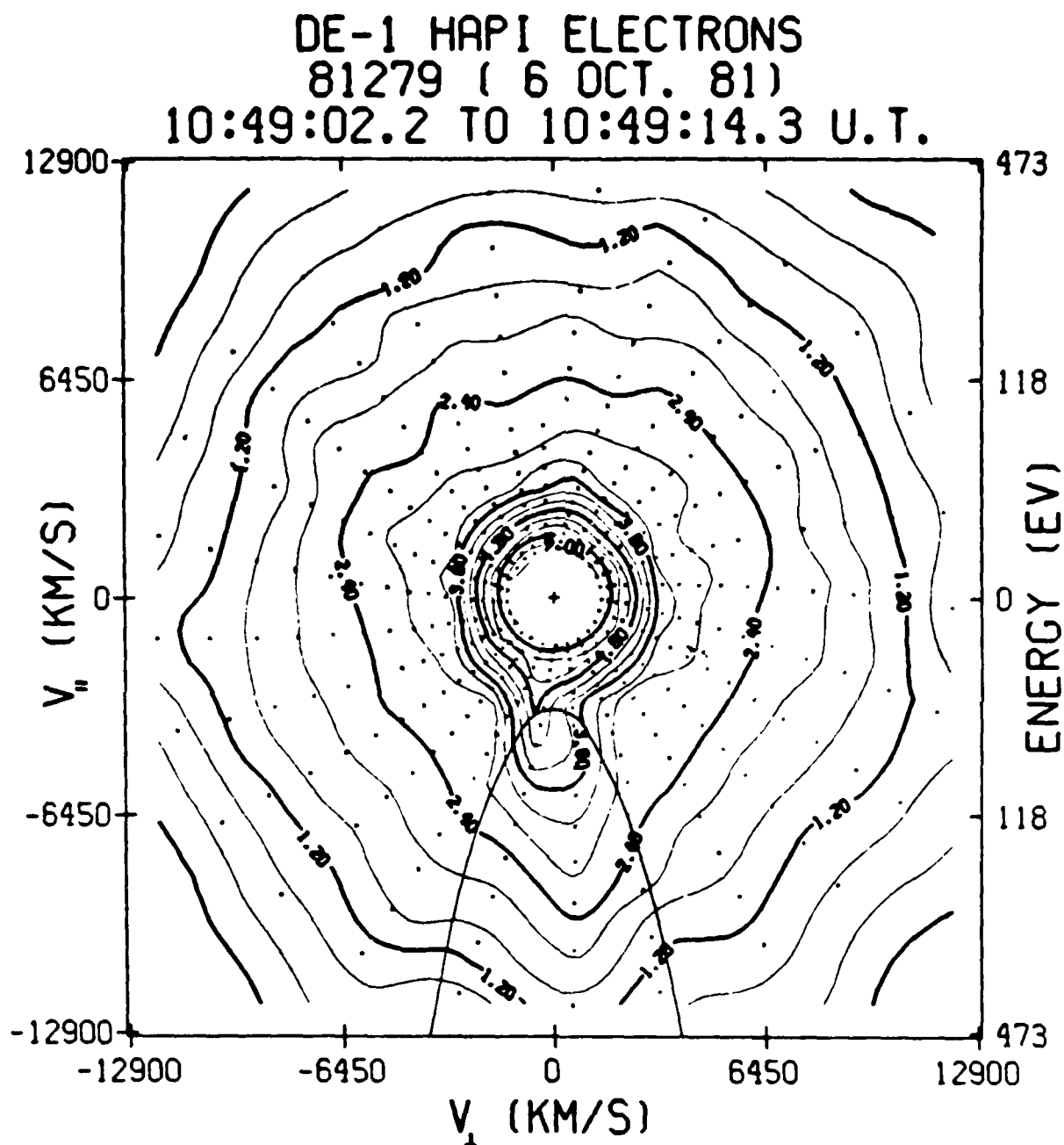


Figure 21. Electron distribution-function contours in the v_{\parallel} , v_{\perp} plane averaged over two rotations of the DE-1 spacecraft. Also plotted is a hyperbola defined by eq. (2) for a potential drop, $V_0 = 31$ V, with maximum altitude at 5870 km.

these values for V_0 and the altitude of the top of the potential drop region are typical. A nonzero spacecraft potential ϕ_0 will subtract from the inferred accelerating potential V_0 .

D. Conclusions

Upward electron beams are observed to be a common phenomenon in regions of downward Birkeland current at altitudes above $\sim 1 R_E$. The electron velocity space distributions are consistent with parallel potential drops of a few tens of volts located near $1 R_E$ altitude, or if there is a distributed potential drop instead of a double layer, the upper boundary is at about $1 R_E$ and the lower boundary is unknown.

In the cusp region, electric current densities calculated from the measured electron distribution functions over the energy range 18 eV - 17.5 keV are in very good agreement with the current inferred from the onboard magnetometer for both downward and upward currents. Uncertainties in the orientation of the current sheet and in the spacecraft potential can readily explain the small differences. Thus, while at lower altitudes downward currents are typically carried by near-thermal upgoing electrons (with only occasional upward beams), at altitudes above $\sim 1 R_E$ the current is typically carried by upward beams of electrons that have been accelerated to suprathermal energies by potential drops of a few tens of eV. Computations of field-aligned currents from hot-plasma distributions observed in numerous orbits of DE-1 in both the dayside and nightside auroral zones and in the polar cap indicate that at altitudes near and above 10,000 km the majority of the current carriers are electrons within the energy range of the HAPI instrument.

V. OBSERVATIONS OF A HEATED ELECTRON POPULATION ASSOCIATED WITH THE 6300 Å SAR ARC EMISSION

A. Introduction and Observations

It was not until the IGY period that the existence of Stable Auroral Red (SAR) arc features was first reported (Barbier, 1958). As implied, identification of these subauroral arcs using ground-based instrumentation relies primarily on the stability and monochromatic nature of the emissions at 6300 Å, a result of the $1D \rightarrow 3P$ transition of atomic oxygen.

Attention was directed toward the ring current as a potential source of energy for maintenance of the emission when early findings of Rees and Akasofu (1963) indicated a strong correlation between the presence of SAR arcs and stormtime enhanced Dst indices. Thermal conduction models, first proposed by Cole (1965), rely on the preferential excitation of atomic oxygen to the $1D$ state by electrons in the high energy tail of a Maxwellian distribution. High temperatures within the ionospheric electron gas are then maintained via conduction of heat along magnetic field lines threading the plasmapause-ring current region. Several mechanisms have been suggested for the actual energy transfer. These include the model of Cole (1965) which uses coulomb collisions between ring current protons and plasmaspheric electrons; that of Cornwall et al. (1971) which predicts the production of ion cyclotron wave turbulence within the ring current and its transfer to plasmaspheric electrons; and the more recent concept of Hasegawa and Mima (1978) that introduces kinetic Alfvén waves to precipitate directly low energy electrons into the SAR arc region.

Recent observations by the Dynamics Explorer-2 plasma experiment have for the first time provided measurements of the heated electrons responsible for the production of the 6300 Å SAR arc emissions. In this paper we will present data for a single SAR arc event centered at 04:05 UT on day 296 (23 October) of 1981. The event was selected for early analysis for two reasons: 1) DE-1 and DE-2 were magnetically conjugate at this time; 2) the satellite track was within the window of the Pacific Northwest Scanning Photometer (MASP) network allowing detailed comparisons between the 6300 Å SAR emission and the particle fluxes. It is in no way a unique event.

On October 23, 1981, following four days of variable SAR arc activity as monitored by the MASP network, the path of DE-2 took it over a distinct SAR arc during a period and at a location being viewed by a MASP unit located at Richland, WA (46.4°N , 240.4°E). Presence of the SAR arc was confirmed by additional sightings by MASP units located near Eureka, MT and Boulder, CO. Due to weather conditions and the orbital position of DE-2, we will utilize data primarily from the Richland, WA site in this paper. A detailed description of the MASP operation is found in Kleckner et al (1981).

Fig. 22 presents contours of 6300 Å emission intensity as measured from Richland at 04:00 UT, near the time of DE-2 passage. Standard triangulation procedures with the MASP unit located near Eureka indicate a region of maximum emission at an altitude of 425-450 km. Compensation for slant path viewing of the SAR arc feature and atmospheric extinction have been applied accordingly. Also included in Figure 22 is the DE-2 track indicated by the dashed line. The small set of circular contours near the center of the

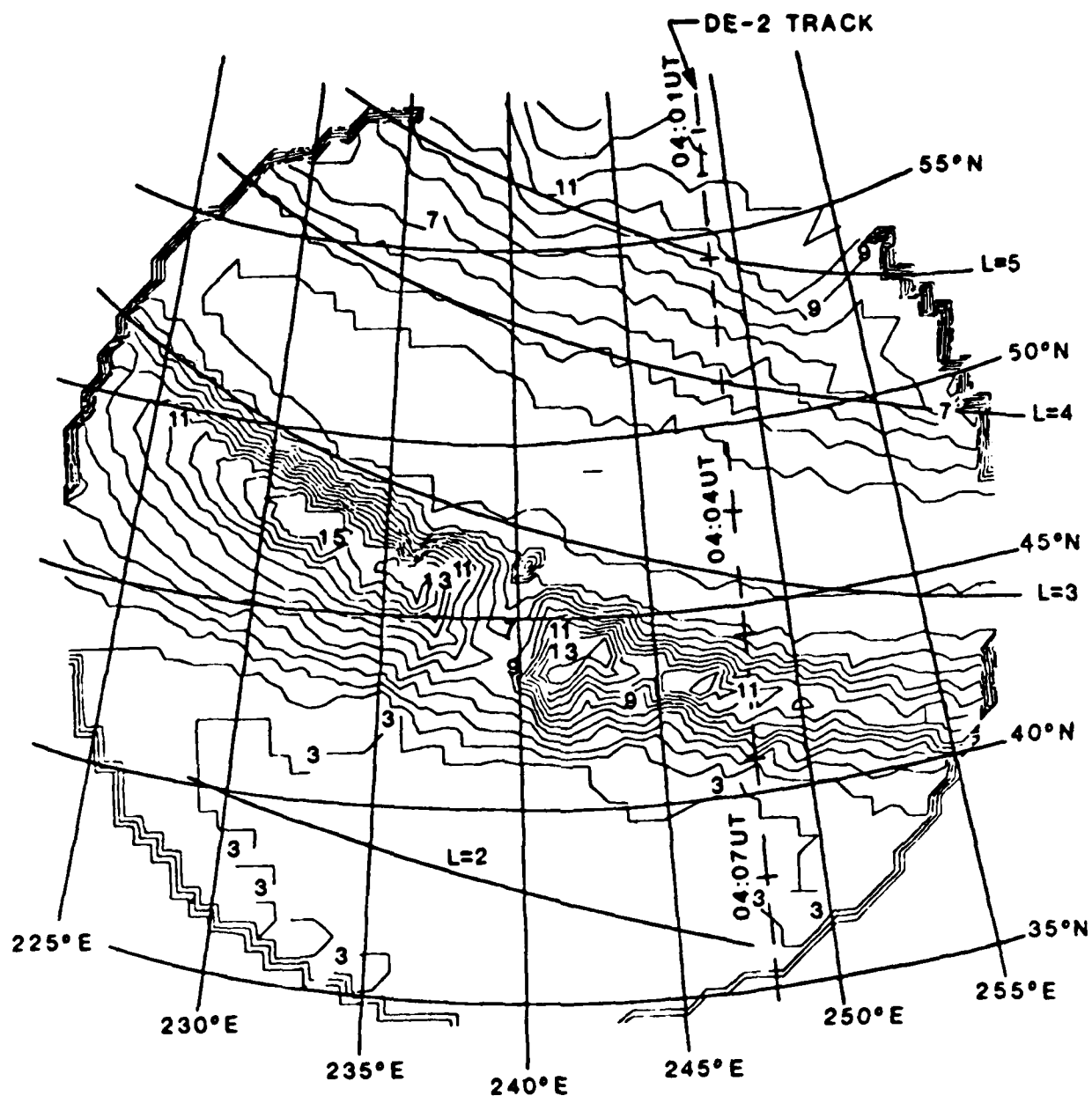


Figure 22. Contour plot of 6300Å emission as measured from Richland, WA. Contour intervals are 100 R. The path of DE-2, projected to 425 km altitude, is shown as a dashed line. The position of Richland, WA is depicted by the artificially produced contours at center of mapping.

plot are artificial, serving only to locate the Richland site. The SAR arc is clearly distinguished by the band of 6300 emission lying just below $L=3$. Aurora poleward of the SAR arc can be seen beginning near $L=4$.

DE-1 and DE-2 were magnetically conjugate during the traversal of the SAR arc, giving a two point simultaneous plasma measurement at 850 and 6000 km. The plasma experiments on board both satellites are identical in instrumentation and response--differing only in configuration. The DE-2 plasma experiment is a family of 15 electron and 15 ion sensors mounted on a single axis, magnetically oriented scan platform allowing each detector to be held approximately fixed in pitch angle. The DE-1 plasma instrument consists of 5 electron and 5 ion detectors which scan in pitch angle with satellite rotation. A complete description of both instruments is found in Winningham et al. (1981) and Burch et al. (1981).

Many of the more important plasma features of the low energy electrons during the SAR arc can be seen in Fig. 23. The upper panel shows a typical field-aligned electron distribution function plotted in the plasma rest frame. The electron population responsible for the SAR arc is located below 8 eV. The fact that the distribution can be characterized by a linear relationship in this region suggests that a Maxwellian fit to give both temperature and density may be applied. The lower panel shows the complete electron distribution function (out to 50 eV). The presence of a field-aligned flow is indicated by the offset of the inner four contours. Use of the offset (about 275 km/sec in this case) allow for individual spectra to be plotted in the plasma rest frame. Calculations of both the temperature and heat flux necessitate a transformation into the plasma rest frame. Neglecting this transformation could result in significant errors.

B. Discussion

The identification of the low energy electron population in Fig. 23 as the particles responsible for the 6300A SAR arc emission is based primarily on the correlation between the MASP photometer data and the DE-2 particle data. Fig. 24 shows the profile of the 6300A emission along the satellite track (solid line from the Richland, WA MASP unit and dashed line from Eureka, MT unit) in Fig. 22 along with coincident particle data. The MASP data clearly show the SAR arc centered at $52^\circ\Lambda$. The more poleward aurora, beyond $56^\circ\Lambda$, is shown assuming a 300 km emission height, typical of O(1D) emissions in the auroral zone (dashed line) and at a SAR emission height of 420 km (solid line). The particle data are shown in Fig. 24 as the log of the electron distribution function (7.5° pitch angle) at 6.7 eV (open circle), 8.8 eV (solid circle) and 20.4 eV (solid triangle). In the rest frame of the plasma the lower two energies are approximately 4.0 and 5.7 eV respectively. Changes in the 6.7 eV values can be interpreted as changes in density while changes in the 6.7-8.8 eV separation as changes in the plasma temperature. The latter, of course, assumes a Maxwellian low energy electron population and as such may not be valid outside the general SAR arc region.

The correlation between the photometer and low energy electron data is unmistakable. The distribution function at 6.7 eV tracks the 6300A emission almost one to one. The large 6.7-8.8 eV separation within the SAR arc itself suggests a very cool electron population. Computation of the electron temperature near $52^\circ\Lambda$ latitude (taking into account the plasma flow

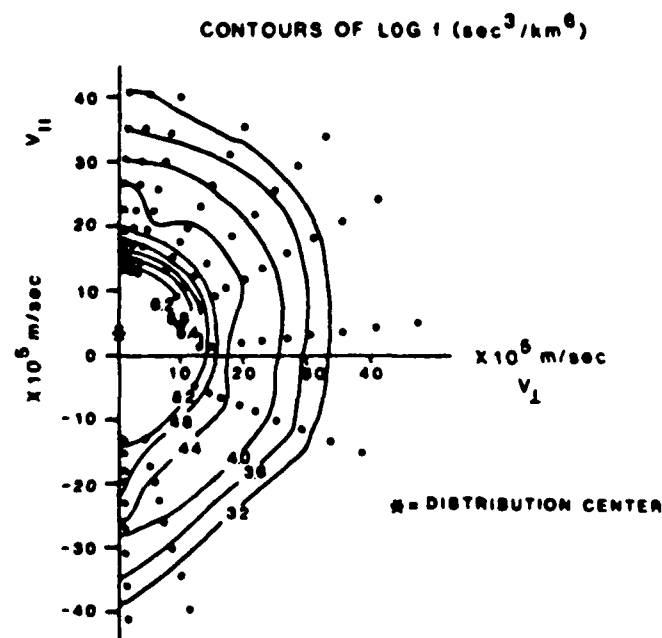
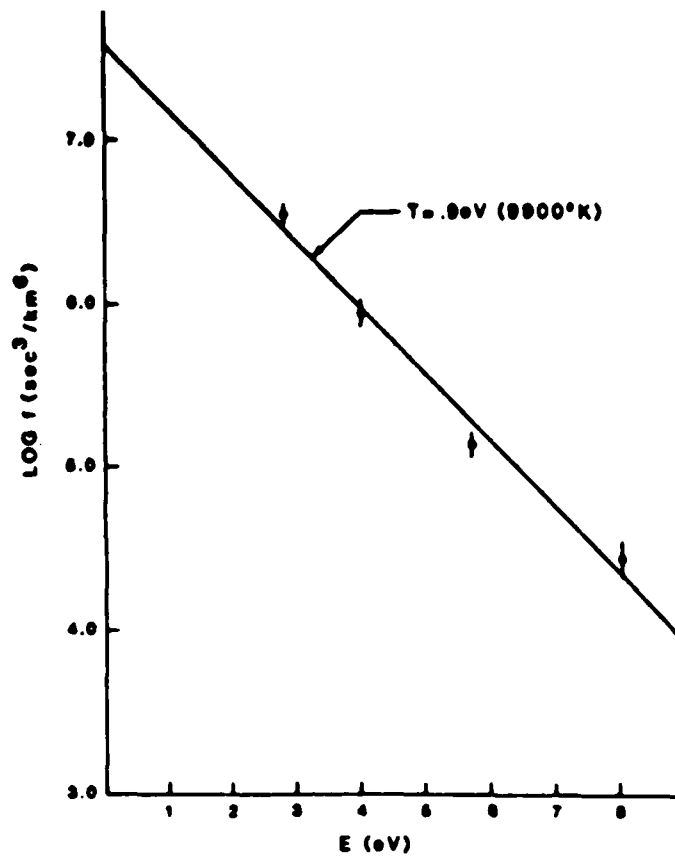


Figure 23. Typical field aligned electron spectrum taken near 04:05:20 UT along with the corresponding 2-D phase space contour plot. The latter distinctly shows the field aligned flow velocity of the low energy electron population.

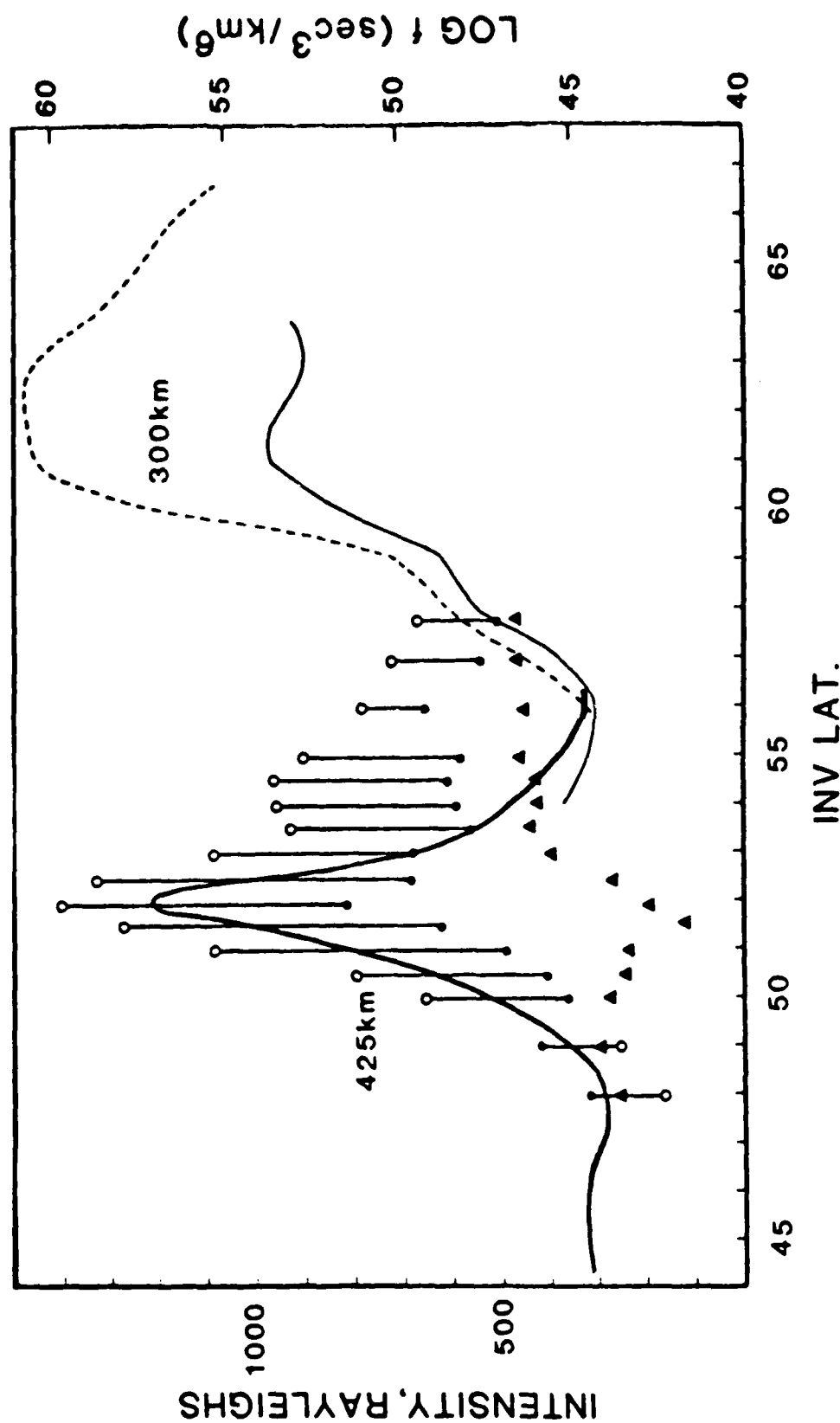


Figure 24. Profile of 6300Å emission (Rayleighs) along the DE-2 path from the Richland, WA (solid line) and Eureka, MT MASP (dashed line) the emissions are computed at a height of 300 km-- typical of auroral 6300Å emission. Several values of the measured distribution function are overlaid over the emission plot. Shown is the distribution function at 6.7 eV (open circles), 8.8 eV (solid circles) and 20.4 eV (solid triangles). The length of the solid line connecting the 6.8 and 8.8 eV data give an indication of the plasma temperature. The 20.4 eV data gives an indication of the photoelectron density.

velocity) gives values of $9900 \pm 110^\circ \text{ K}$. Corresponding computations of the density using a satellite potential of -1.7 ± 0.1 volts (R. Heelis, private communication) gives a density of $250 \pm 50 \text{ cm}^{-3}$ for this particle population.

It should be noted that there is nearly a 500 km difference between the measurement of the particles and the measurement of the 6300/ emission altitude. Some degradation of the particles in moving to the emission altitude is expected. With a single measurement, the amount of degradation cannot be determined directly without a model. Without resorting to a specific model, however, we can make some positive statements concerning the electron transport. Between days 288 and 324 of 1981 more than 75 distinct particle populations with characteristics similar to those presented in this paper have been identified. When ground observations exist to support the satellite observations these electron populations have been found to be associated with SAR arcs. The satellite observations extend from above 900 km to 400 km which indicates the ability of this electron distribution to exist over a considerable length of the flux tube.

The day 296 SAR arc contains several features which may yield important information as to the production mechanisms responsible for the low energy electrons. In Fig. 24 one finds a decrease in the conjugate photoelectron intensity within the SAR arc. Photoelectrons give a measure of the coupling between the northern and southern hemispheres. Lee et al (1980) have postulated that such decreases might be due to enhancements in the thermal electrons within the local flux tube. This shielding phenomena has been noted in many of the SAR arc cases (both visual and subvisual) we have investigated.

There appears to be no corresponding ion precipitation accompanying the low energy electron enhancement. This is contrary to the Cornwall et al (1971) prediction of precipitating ions on the order of $10^8/\text{cm}^2\text{-sec}$. This fact in conjunction with the lack of a definite low energy electron signature or enhancement during this time period, might suggest a lower altitude production for the thermal electrons. Both of these facts would seem to point to a production mechanism in line with the Hasagawa and Mima (1978) work.

C. Summary

The low energy electrons observed by the DE-2 plasma experiment are associated with the 6300A SAR arc emission. The following features have been noted:

1. The heated electrons have a significant field aligned flow velocity.
2. There is no corresponding electron population observed by the DE-1 plasma instrument located at 6000 km above the SAR arc.
3. The SAR arc occurs at the plasmasheet-plasmasphere overlap boundary, identified by the drop out of the plasmasheet particles observed at DE-1.
4. The heated electron component appears fairly Maxwellian with temperatures of about 0.9 eV, which is not significantly different than predicted by several theories.

5. The absence of observable precipitating ring current ions within the SAR arc, which may point to mechanisms not involving ring current ions.
6. The decrease in the conjugate photoelectron intensities, indicating a partial shielding of one hemisphere from another.
7. Modeling of the energy deposition and degradation of the observed electrons should include the possibility of a continual driving source along the total flux tube.

VI. POLAR RAIN OBSERVATIONS

Winningham and Heikkila (1974) first described polar rain, using data from the ISIS 1 satellite. Polar rain is the most common type of particle precipitation over the polar caps. This broad and relatively structureless electron precipitation can often fill the entire polar cap. The precipitating electrons typically have thermal energies on the order of 100 eV and are isotropic over the downcoming hemisphere. The energy flux carried by the particles is of the order of 10^{-3} to 10^{-2} erg cm⁻²sec⁻¹ (Burke, 1982). The spectral distribution of the polar rain electrons has the same shape as that of cusp electrons, but is lower in intensity, suggesting that polar rain originates in the magnetosheath and travels to the polar ionosphere via the lobes of the magnetotail.

Figures 25a and 25b show differential energy flux from the LAPI instrument aboard DE-2 for a portion of a polar pass on day 295 (22 October) of 1981. The top panel shows data for 8° pitch angle electrons, and the bottom panel shows 45° pitch angle ion data. The upper center panel shows 90° and 0° pitch angle electron data from the GM tube. The data are coded according to the color bars at the right. Satellite ephemeris is shown at the bottom. In this particular pass, DE-2 passed through the northern polar cusp at approximately 1306-1307 UT and into the polar cap. The polar rain can be seen clearly as a bright band in the electron panel over the energy range ~60-600 eV. The electron flux intensity remained fairly constant in intensity until just after 1309 UT when it abruptly decreased. Notice the lack of ion fluxes over the polar cap.

Figure 26 shows line plots of the average energy, energy flux, and density of the downcoming electrons for 1306-1311 UT. These parameters are obtained by integrating distribution functions over energy from 5 eV to 20 keV. During the entire interval, the average electron energy and density remained roughly constant. The average energy was about 100 eV and the density of downcoming electrons was in the range of 1-5 cm⁻³. These values of energy and density are representative of the polar rain. After exit from the cusp at about 1307 UT, the energy flux increased very slightly toward the pole until just after 1309 UT when it decreased by approximately 50%.

Figure 27 shows a DE-1 high-altitude polar pass approximately three hours after the DE-2 pass shown in Figure 25. During the interval 1617-1619 UT, DE-1 traversed the magnetic local time and invariant latitude corresponding to those of DE-2 just poleward of the cusp in Figure 25a. The format is the same as for Figure 25, except for the absence of GM tube data. The polar rain may be seen as a band in the spectrogram over the energy range ~100-600 eV. Bracketing the polar rain are counterstreaming energetic ($E > 600$ eV) electron beams at 0° and 180° pitch angle and upward-moving low-energy ($E < 100$ eV) electron beams. The source of the energetic counterstreaming electrons is open to question and presently under study by Gurgiolo and Burch (1982). Two possibilities for the source would be reflection by a potential barrier at the magnetopause (Foster and Burrows, 1976) or direct access of solar electrons. Upstreaming ion conics may be seen in the lower panel.

Comparing Figure 25 and Figure 27, it is interesting to note that the polar rain is of the same spectral nature at both altitudes, suggesting the

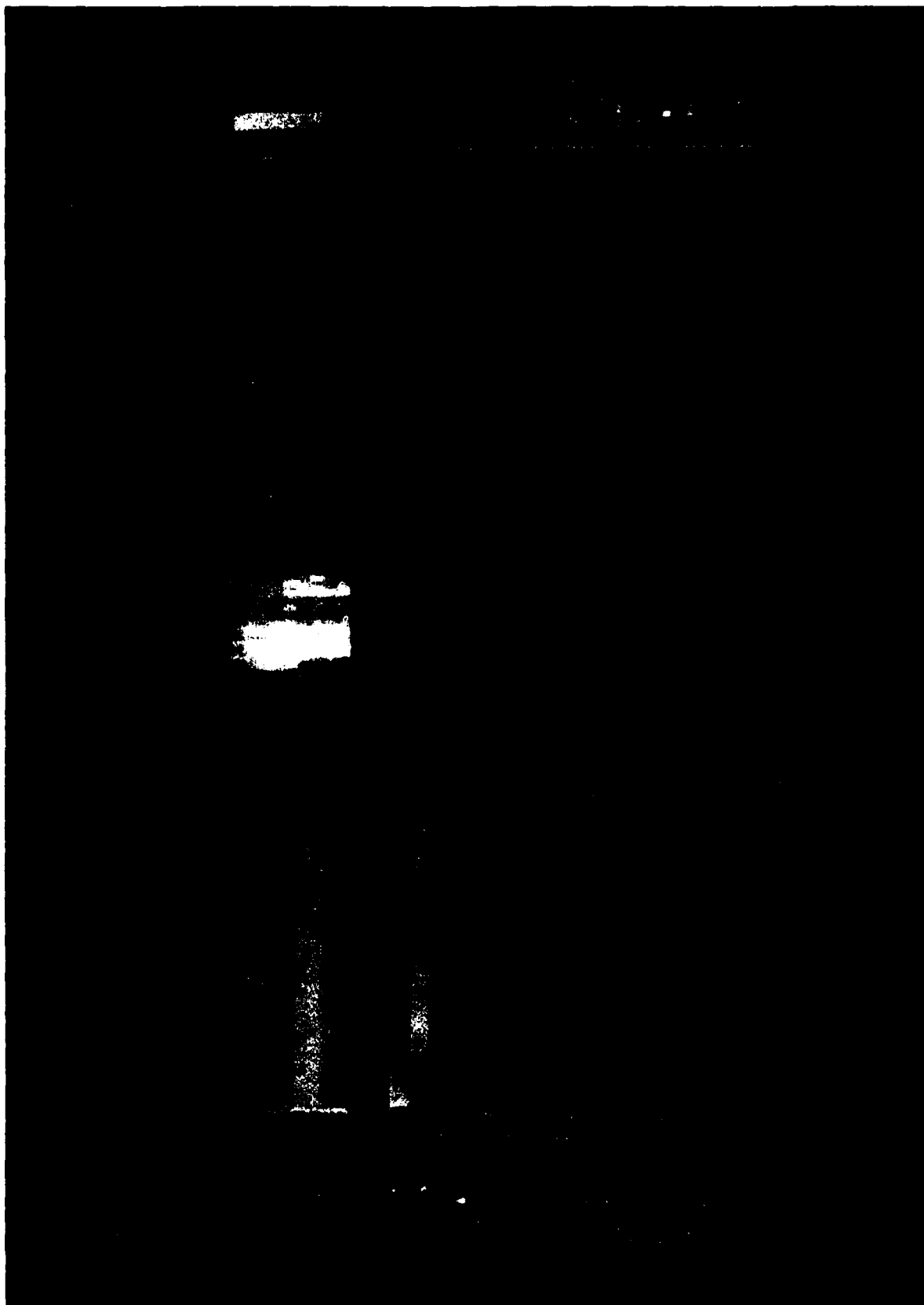


Figure 25a. Energy-time spectrogram of 8° pitch angle electrons and 45° pitch angle ions as observed at DE-2.

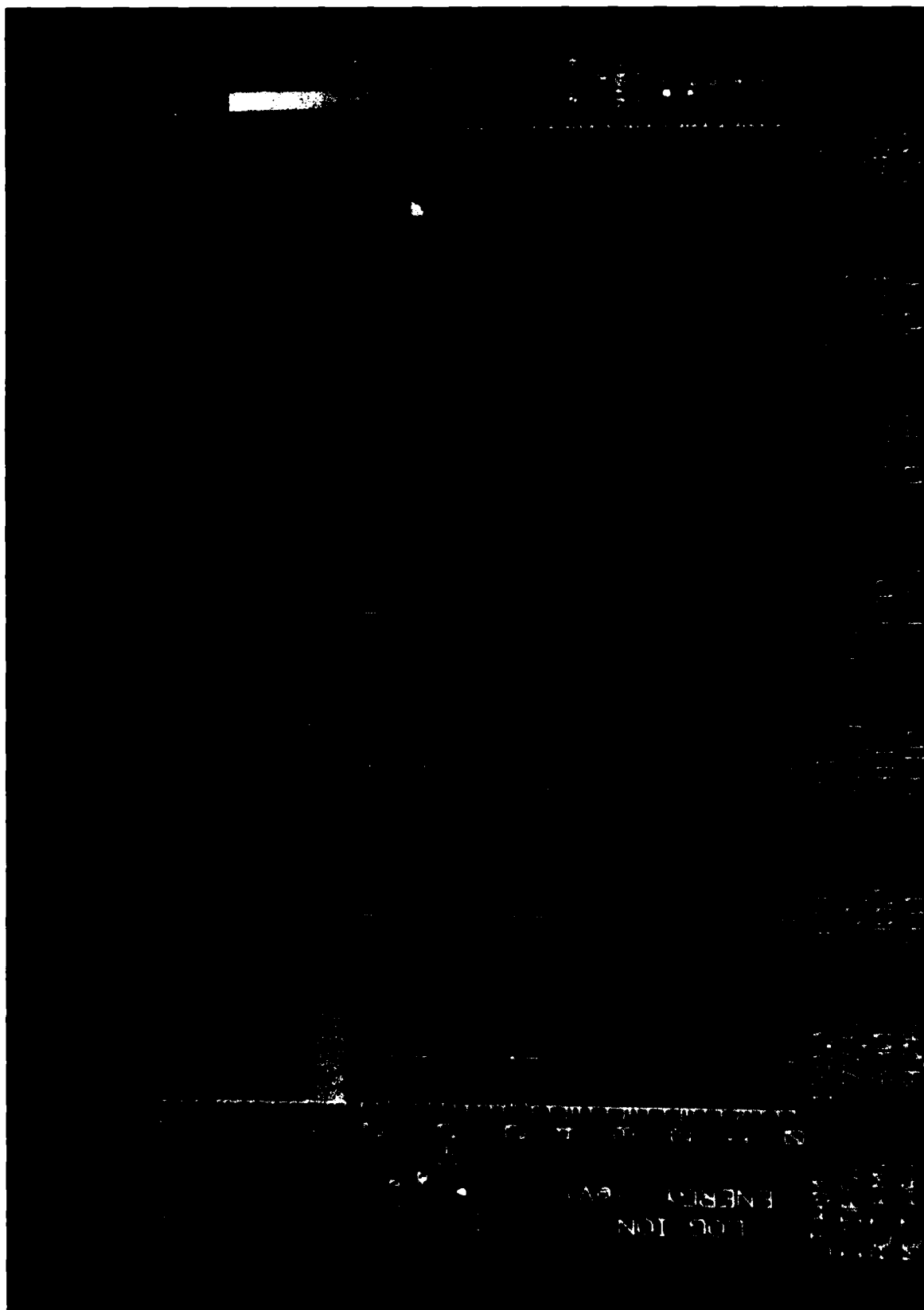


Figure 25b. Energy-time spectrogram of 8° pitch angle electrons and 45° pitch angle ions as observed at DE-2.

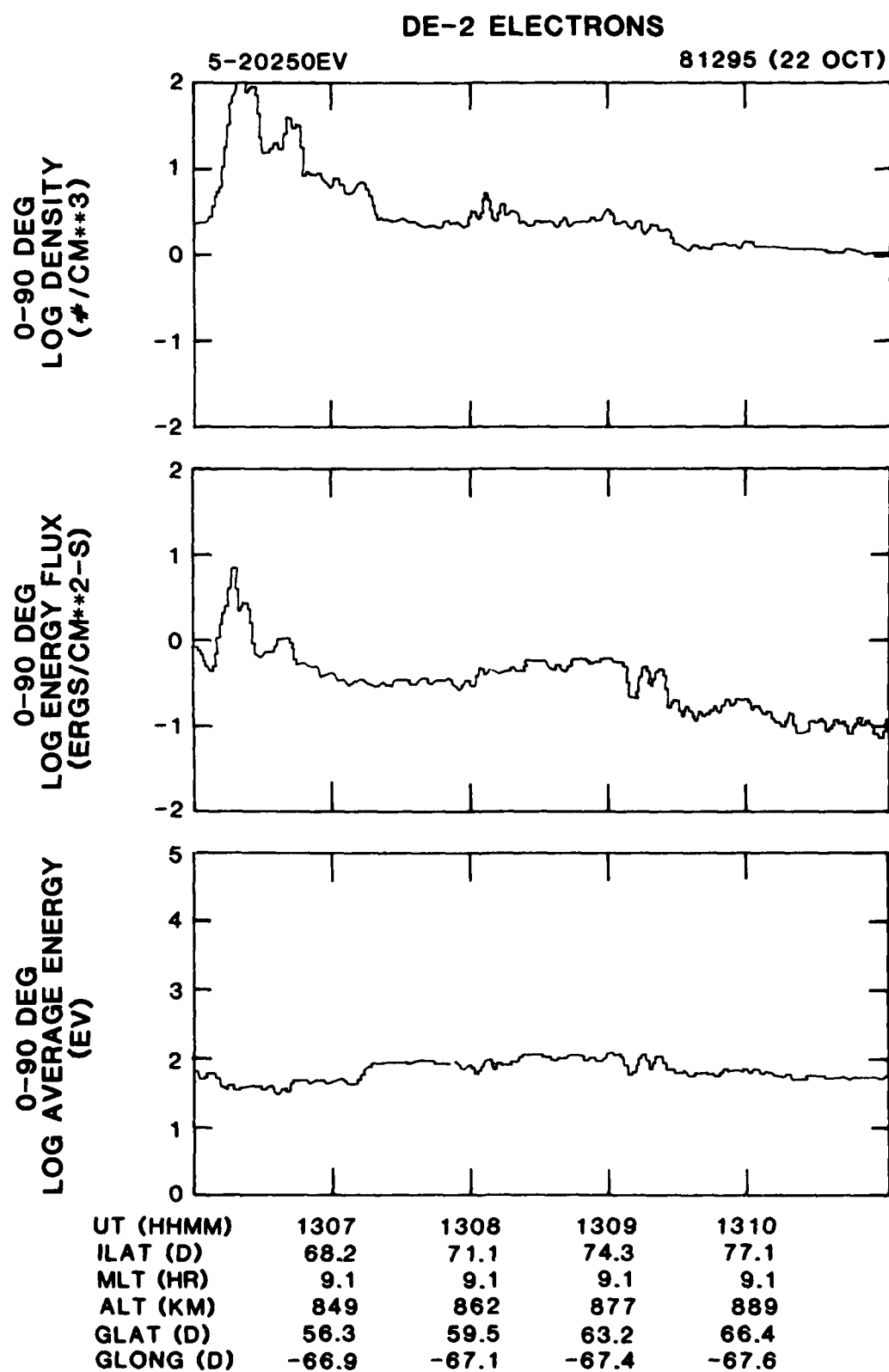


FIGURE 26. Line plots of average energy, energy flux, and density of downcoming electrons.

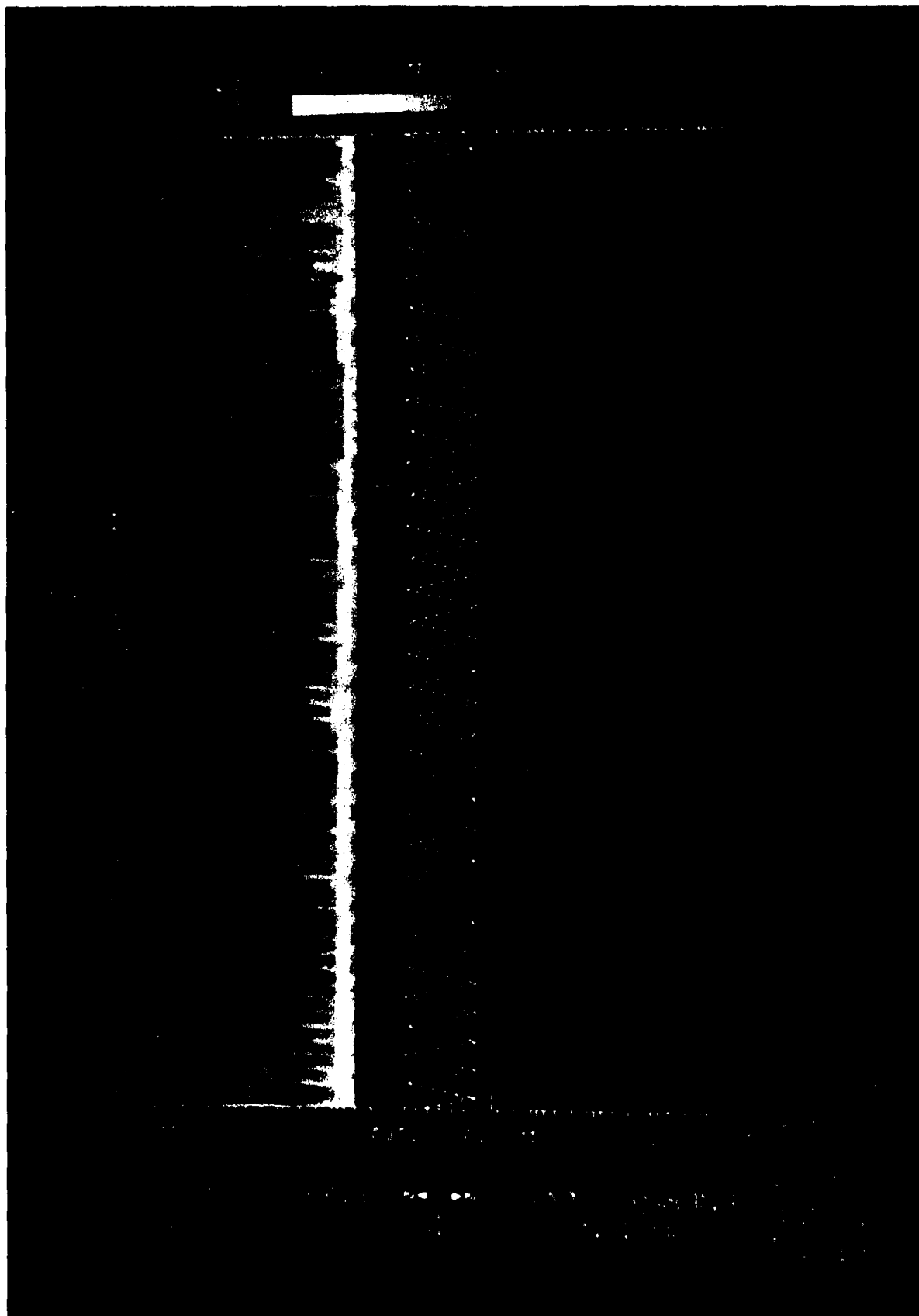


Figure 27. Energy-time spectrogram of electrons and ions. The detector's pitch angle is plotted in the center panel.

absence of any significant acceleration between the two satellite locations. To demonstrate further the similarity between the electrons at the two satellites, Figure 28 shows number density, energy flux, and average energy at DE-1 for the period 1614-1619 UT. The average energy was ~ 100 eV, density was $\sim 1 \text{ cm}^{-3}$ and the energy flux was $0.8 \text{ ergs cm}^{-2}\text{s}^{-1}$. The corresponding values at lower altitudes were ~ 100 eV, $\sim 2 \text{ cm}^{-3}$, and $\sim 0.8 \text{ ergs cm}^{-2}\text{s}^{-1}$.

A detailed look at the near-field-aligned electron populations at the two satellite locations is provided in Figure 29. Shown are three data sets - two single energy sweeps from LAPI, one just at the poleward edge of the cusp and one approximately 10° poleward of the cusp, and a single energy sweep from HAPI at a location which maps to near the location of the first LAPI spectrum. From Figure 27, we first can see that above photoelectron energies the LAPI population can be represented by a Maxwellian, allowing the temperatures to be estimated. Near the cusp a least squares fit gives a temperature of 92 eV, while farther poleward the temperature is 99 eV. The HAPI spectrum appears well-fitted by two Maxwellians above photoelectron energies. The low-energy population has a least-squares fit temperature of 65 eV, while the higher energy population has a temperature of 141 eV.

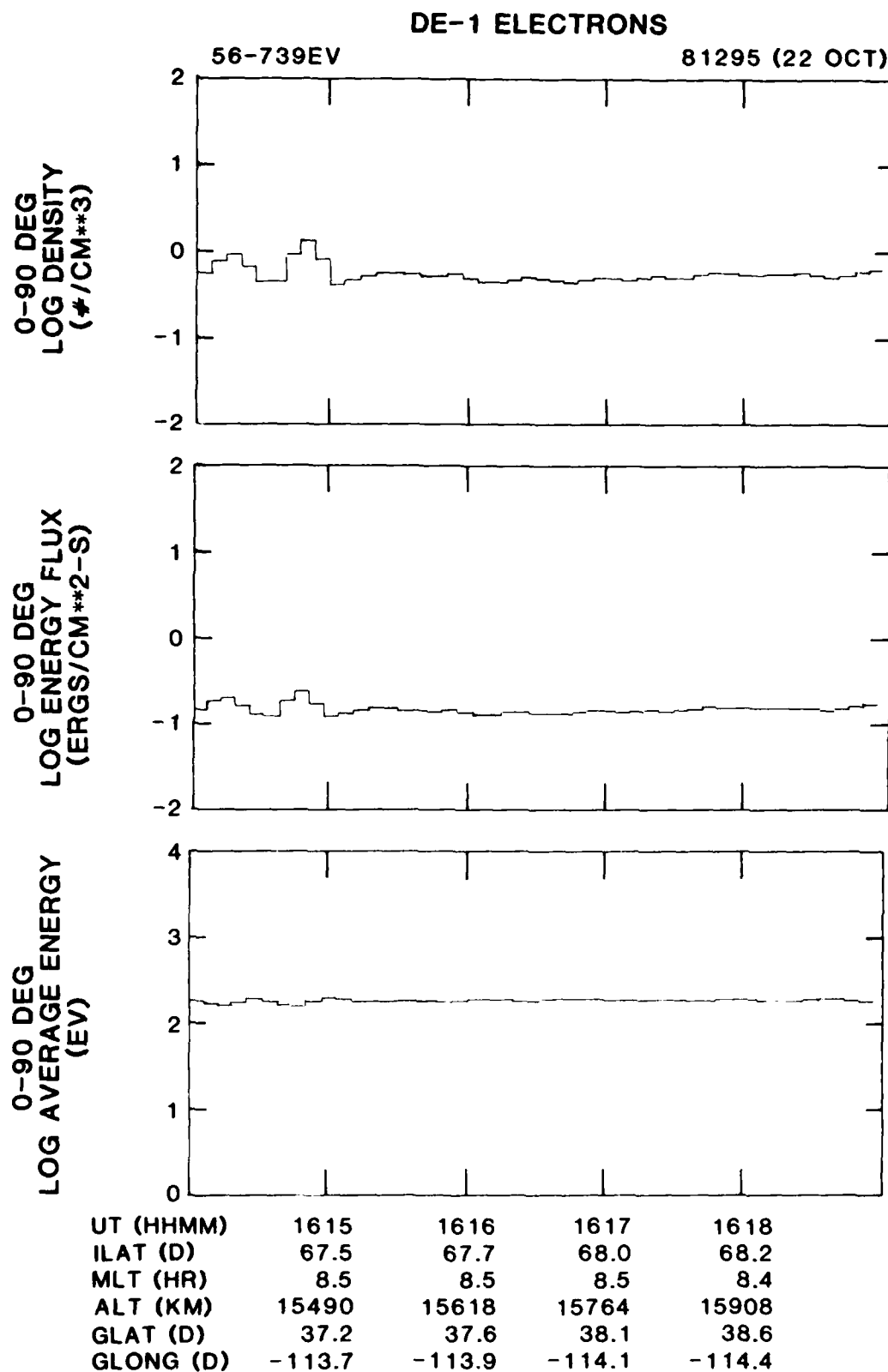


FIGURE 28. Line plots of number density, energy flux, and average energy of downcoming electrons.

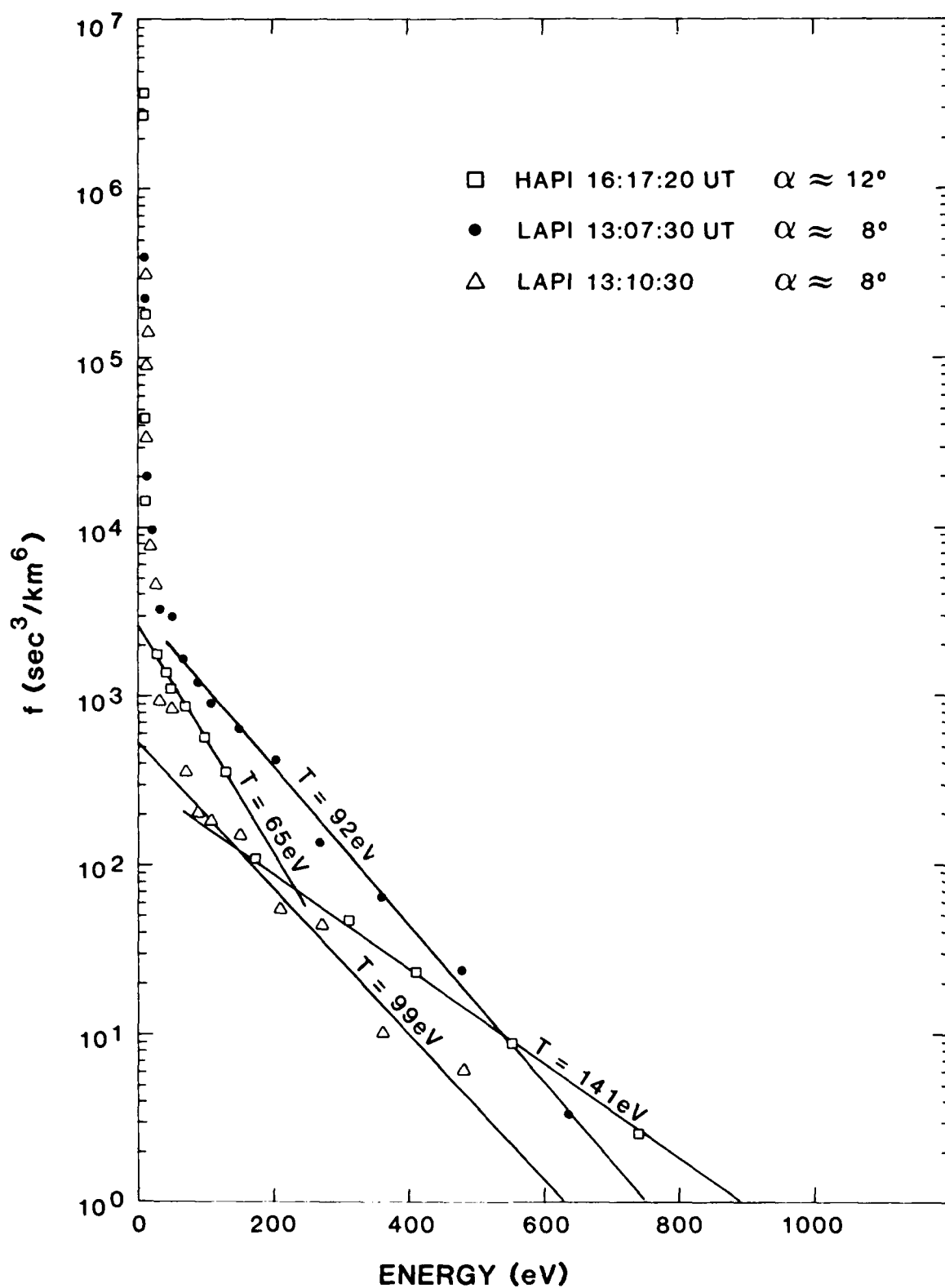


FIGURE 29. Electron energy spectra from DE-1 and DE-2 in the cusp region

VII. ACCELERATED POLAR WIND

The polar wind refers to the continual escape of ionospheric plasma from the polar ionosphere along open magnetic field lines. This escape of particles has consistently been observed to lead to a depletion of light ionospheric ions (ref. 7) and electrons in the upper polar ionosphere. Until recently, observations of the polar wind in the literature were limited to the low-altitude observations of Hoffman and Dodson (1980). They reported a continual upward flow of H^+ and He^+ over the polar caps in the range 1-5 km/sec and 1-3 km/sec, respectively. The low energy of these particles precluded most instruments from directly obtaining a distribution function. However, as pointed out by Gurgiolo and Burch (1982), polar-wind models predict that the particle velocity should increase with altitude (Schunk and Watkins, 1982). Thus, the high altitude satellite DE-1 is an ideal platform from which to study the polar wind.

Plasma data from DE-1 polar passes indicate that ions with peak differential energy fluxes in the 5 to 100 eV range are continually flowing out of the dayside cusp and polar cap. The flows have both a field-aligned and a conic component. The field-aligned component is unmistakably the polar wind. Gurgiolo and Burch (ref. 5) concluded that the conics observed in conjunction with the polar wind are polar-wind ions that have been perpendicularly heated.

The polar-wind observations to be discussed were made during a polar pass on day 272 (September 29) of 1981. Figure 30 consists of 3 sets of particle spectrograms on the same format as Figure 3. Each spectrogram displays the differential energy flux for the particle detectors which lie closest to the plane containing the local magnetic field vector.

Figure 30 shows a continuous band of upward flowing ions (near 180° pitch angle). The satellite was inside the cusp during the interval covered in Figure 30a. At 1411 UT, the satellite passed through the poleward cusp boundary. The upward ions showed a gradual increase in energy throughout and slightly poleward of the cusp, then they begin to decrease steadily, the peak in the differential energy flux eventually dropping below the lowest energy channel of HAPI. Within the cusp, the conic and field-aligned ions appear as "tuning forks" in the spectrograms. In the polar cap the conics become less and less apparent, as the energy and angular separation of the conic and field-aligned ions decrease. In the polar cap, there also is a shift in the field-aligned ions from 180° pitch angle to 165° , indicating an antisunward flow.

Figure 31 shows a detailed view of the field aligned ion population. Two data sets are shown, each of which was averaged over four satellite revolutions to improve counting statistics. Each of the distributions was transformed to the rest frame of the plasma prior to averaging (except for S/C charging which was about 20V). The two data sets were taken beginning 1434:05 UT (solid circles) and 1434:54 UT (open circles). In Figure 31 Maxwellian distributions are straight lines, with the slope being proportional to the plasma temperature and the intercept with the distribution axis being proportional to the plasma density.

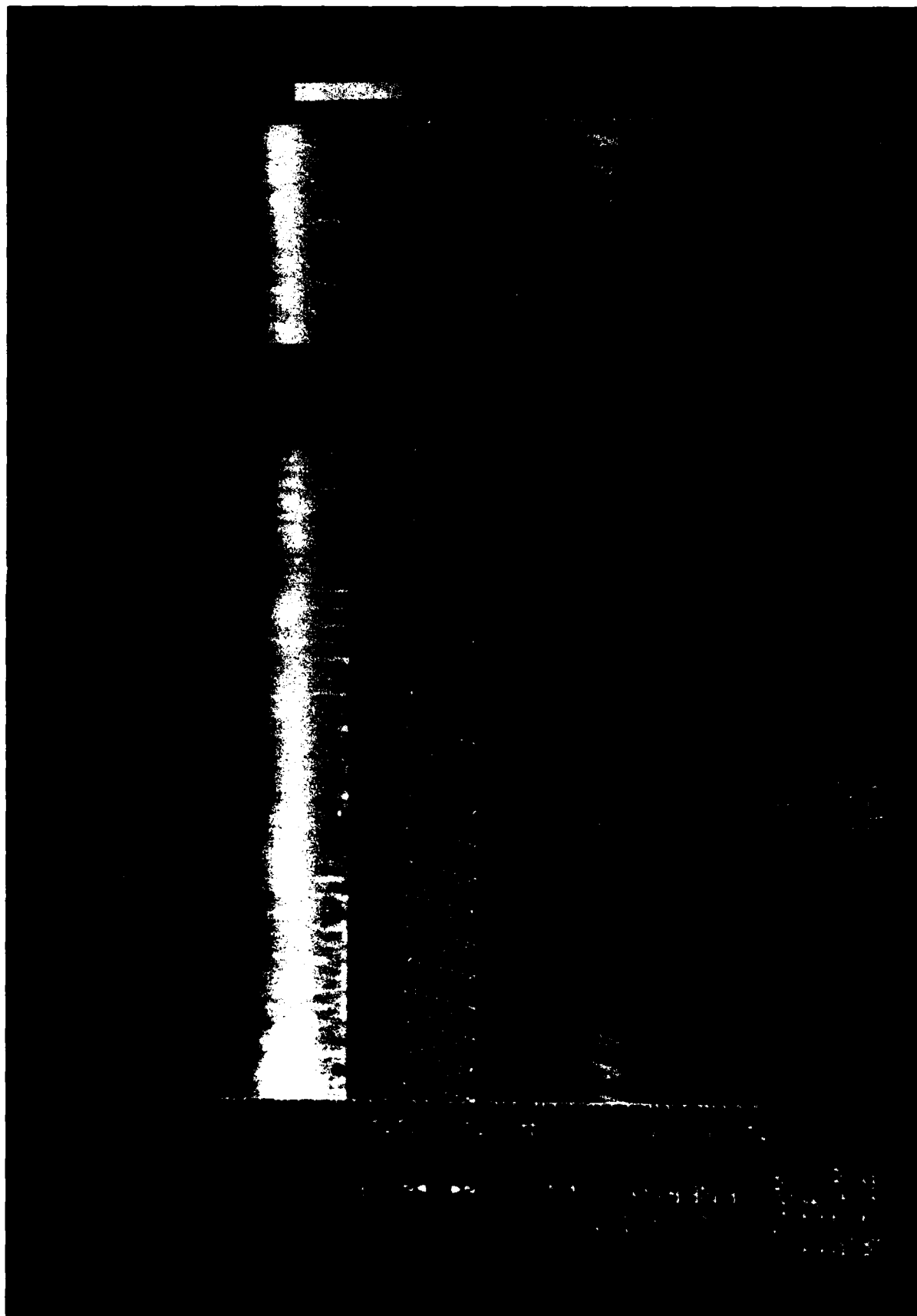


Figure 30a. Energy-time spectrogram using same format as Figure 3.

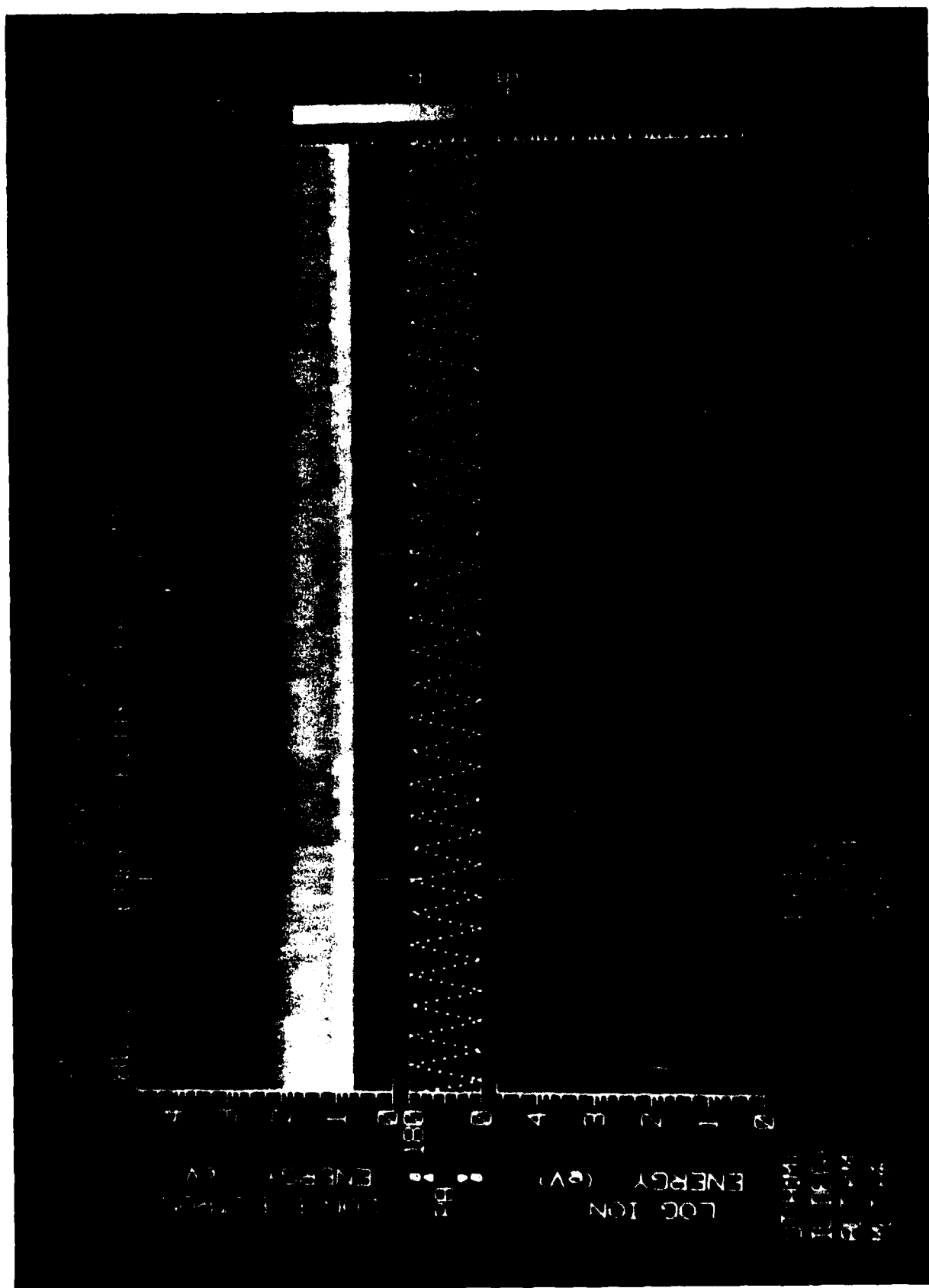


Figure 30b. Energy-time spectrogram using same format as Figure 3.

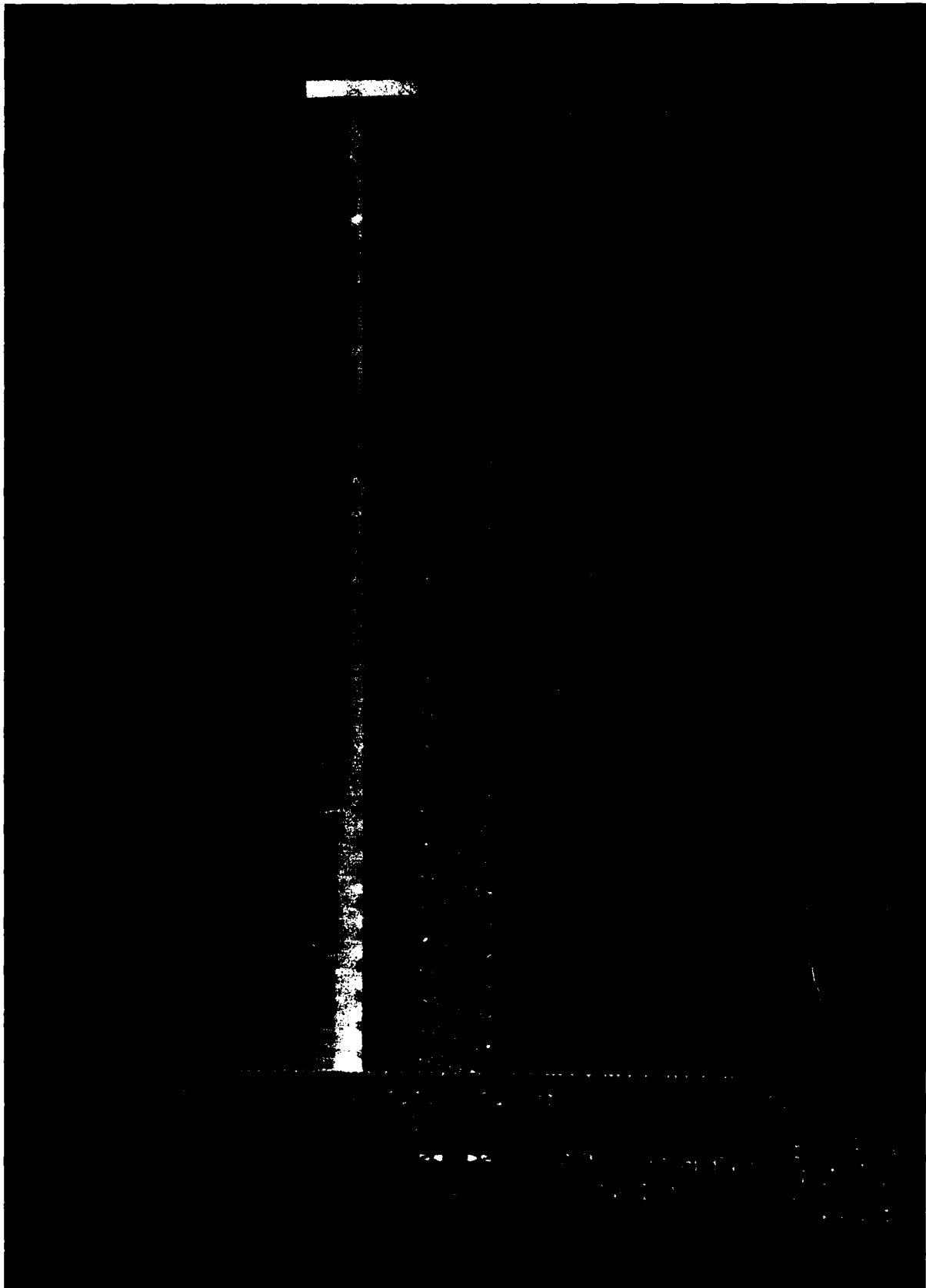


Figure 30c. Energy-time spectrogram using same format as Figure 3.

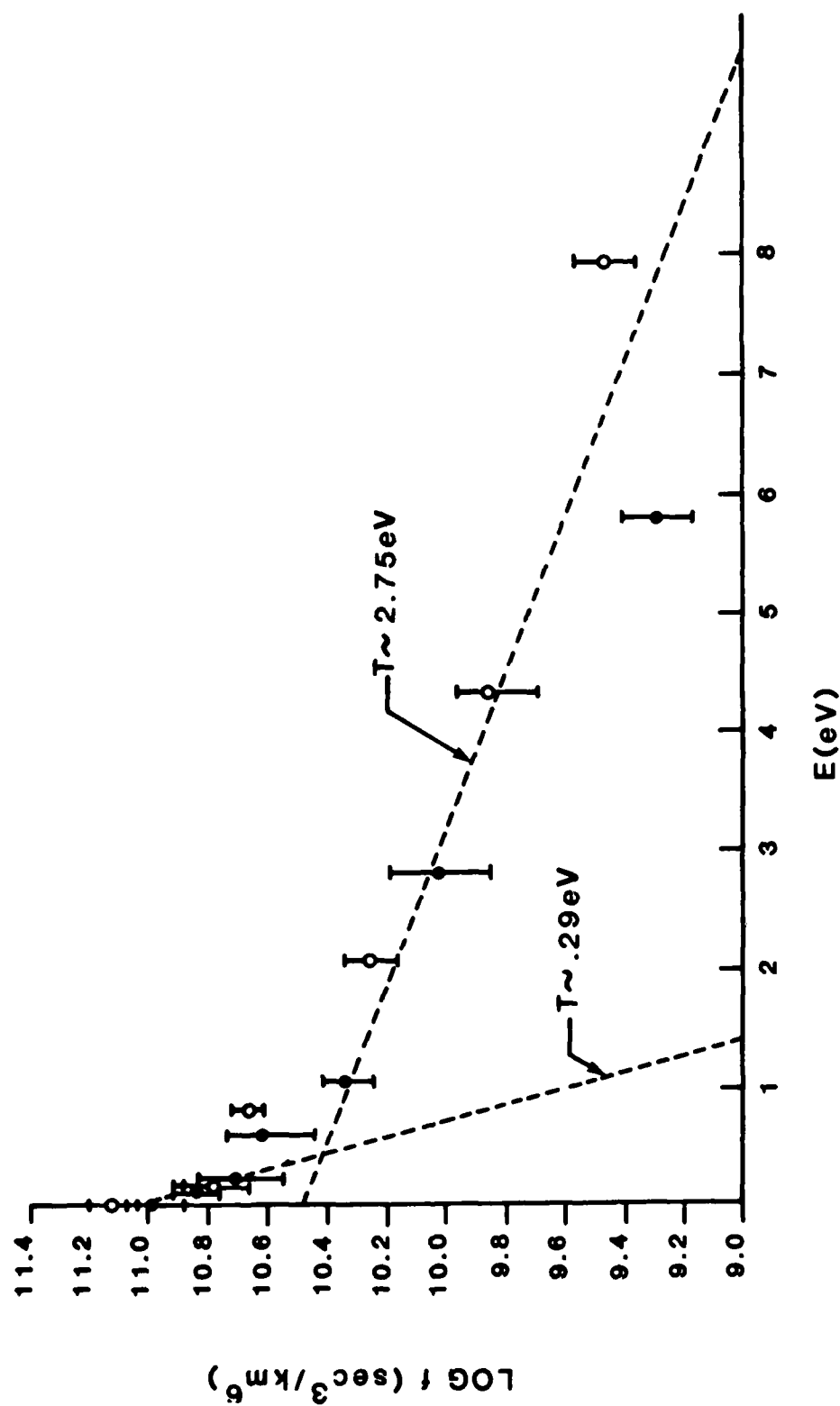


FIGURE 31. Velocity space spectrum for DE-2

From Figure 31 we can see that the field-aligned ion component observed in the polar regions is comprised of two ion populations--a low energy component with temperature below 0.5 eV and a high energy tail with temperature above 1.5 eV. Both ion populations would appear to be well represented by a Maxwellian distribution, allowing the estimates of the temperatures to be made. A least squares fit to the low-energy population of Figure 7 gives a temperature of 0.29 ± 0.16 eV ($3200^\circ\text{K} \pm 1800\text{K}$). The corresponding temperature of the high energy plasma population in Figure 7 is found to be 2.7 ± 0.7 eV. The peak at about 1 eV may be due to an ion heavier than H^+ .

There is little doubt that the lower energy, field-aligned ions constitute the "classical" polar wind. The high energy tail, however, is not a feature predicted by polar-wind models. It is likely that this hotter plasma is the result of a perpendicular heating of polar-wind ions. Assuming that all ions in the polar wind are of equal temperature, Figure 7 gives heating on the order of 4 to 10.

We envision a scenario as shown in Figure 32 occurring during the polar wind escape along magnetic field lines. At low altitudes the generation of the polar wind occurs and ionospheric ions begin to escape along the open polar cap and cusp field lines (Figure 32a). The presence of ion perpendicular heating along the open field lines produces the characteristic conic signature (Figure 32b). The distribution above the heating region can be considered a two-component plasma consisting of unheated and heated polar-wind particles. The unheated polar wind is still field aligned, while the heated ions have large velocities in the direction perpendicular to \mathbf{B} . As the distribution travels upward, the perpendicular arms of the distribution will begin to collapse toward the magnetic field direction in accordance with the first adiabatic invariant, and a field-aligned high energy tail to the polar wind should develop (Figure 32c). Figure 32d shows contours of a typical conic/polar-wind population measured in the cusp on day 272.

Ion conics have been reported by numerous people (Ungstrup et al., 1979; Gorney et al., 1981). Theories as to the production of the conic ion distribution have favored a perpendicular heating by electrostatic ion-cyclotron waves (Dusenberry and Lyons, 1981; Lysak et al., 1980), although recently (Chang and Coppi, 1981) it has been proposed that a heating by lower hybrid waves may also be a viable conic generation mechanism. The problem is, however, that most of these theories are applicable only at low altitudes in the auroral zone. Adaptations of the theories to the environment of the polar cap must be made to explain these observations.

Using the observed conic pitch angle distribution, the altitude of the observation and an assumed value for the initial conic pitch angle, it is possible through the first adiabatic invariant to estimate the altitude of the conic generation. In general the initial conic pitch angle for such computations is assumed to be 90° ; however, if the source plasma already has a significant V_ϕ , as the polar wind does, then the initial conic pitch angle is expected to shift to lower values. Using a dipolar magnetic field approximation and estimating the values of the initial conic pitch angle through energy conservation arguments (which assume that V_ϕ does not change between the observation height and the conic height) we estimate the heating to occur at an altitude of about 12,000 km--constant throughout both the cusp and polar cap. By using an initial conic pitch angle of 90° we can place a lower limit to the heating altitude at 8000 km.

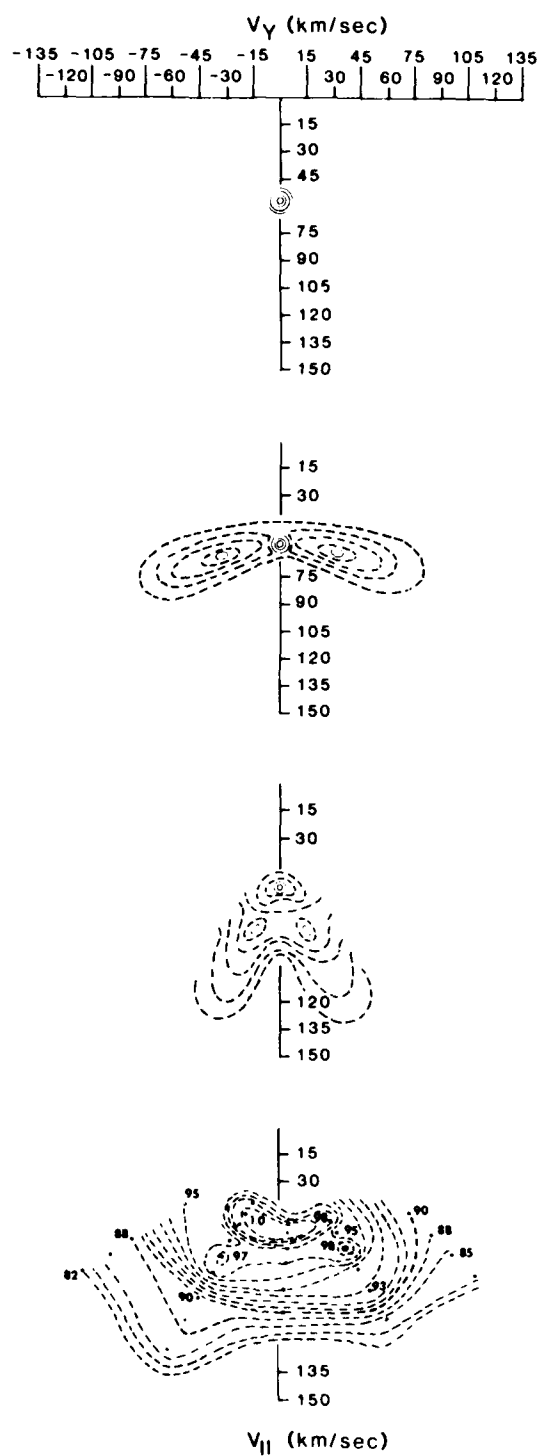


FIGURE 32. Evolution of polar wind. Shown are isocontours of the distribution function in phase space

VIII. OBSERVATIONS OF ION AND ELECTRON ACCELERATION EVENTS PRODUCED BY PARALLEL ELECTRIC FIELDS

The electrical coupling between the high-altitude and low-altitude regimes of the polar cap is an important aspect of magnetosphere-ionosphere interactions. The unique placement of the Dynamics Explorer orbits with respect to each other has afforded an excellent opportunity to investigate this coupling between the two regimes. Frequently, DE-1 and DE-2 observe signatures of field-aligned acceleration of ions and electrons above the polar cap. In this section, we briefly present observations made on October 17, 1981 (day 81290) above a "theta aurora" signature.

Figure 33 shows a spectrogram of 180° ions and 0° pitch angle electrons from HAPI. The satellite crossed the polar-cap arc field lines during the interval 1630-1650 UT. Two intervals of intense electron fluxes below 1 keV were seen: ~1631:30-1633:15 UT and ~1642-1649 UT. Figure 34 shows contour plots of the log of the distribution functions of ions (Figure 34a) and electrons (Figure 34b) for the interval 1632:45-1632:57 UT. The ions showed a strong upgoing beam at approximately 100 eV. The electron fluxes were isotropic except for a loss cone. Thus, the combined electron and ion observations indicated that an approximately 100 eV potential drop lay below the satellite altitude.

Figure 35 shows contours in the same format as Figure 34, for the interval 1646:30 to 1646:36 UT. By this time the ions had become isotropic, while the electrons showed a downcoming beam of 100 eV. Thus, the acceleration region appears now to be above the satellite altitude (17313 km) while remaining at ~100 eV.

The plasma characteristics described above are very similar to those observed by DE-1 in the high altitude ($>15,000$ km) nightside auroral zone, except that the energy of the polar cap acceleration events is lower. Correlation studies by Hardy et al. (1982) have already noted that the plasma signatures of polar cap acceleration events at low altitudes are similar to those of evening discrete arcs. The parallel electric field responsible for the polar-cap acceleration could be produced by the same process as the evening auroral arcs.

Satellite observations of convection and electron precipitation at low altitudes (<1000 km) have indicated that convective electric fields point toward the region of polar-cap acceleration ($\nabla \cdot \mathbf{E} < 0$) (Burch et al., 1979). The polar cap acceleration region is therefore a region of negative space charge. Burke et al. (1982) used the simultaneous electric field, magnetic field and electron flux measurements of the S3-2 satellite to demonstrate that upward Birkeland currents were embedded in regions of polar cap acceleration. These observations suggest that field-aligned potentials develop as a result of imperfect mapping of magnetospheric convective electric fields to the ionosphere (Hardy et al., 1982; Burke et al., 1982).

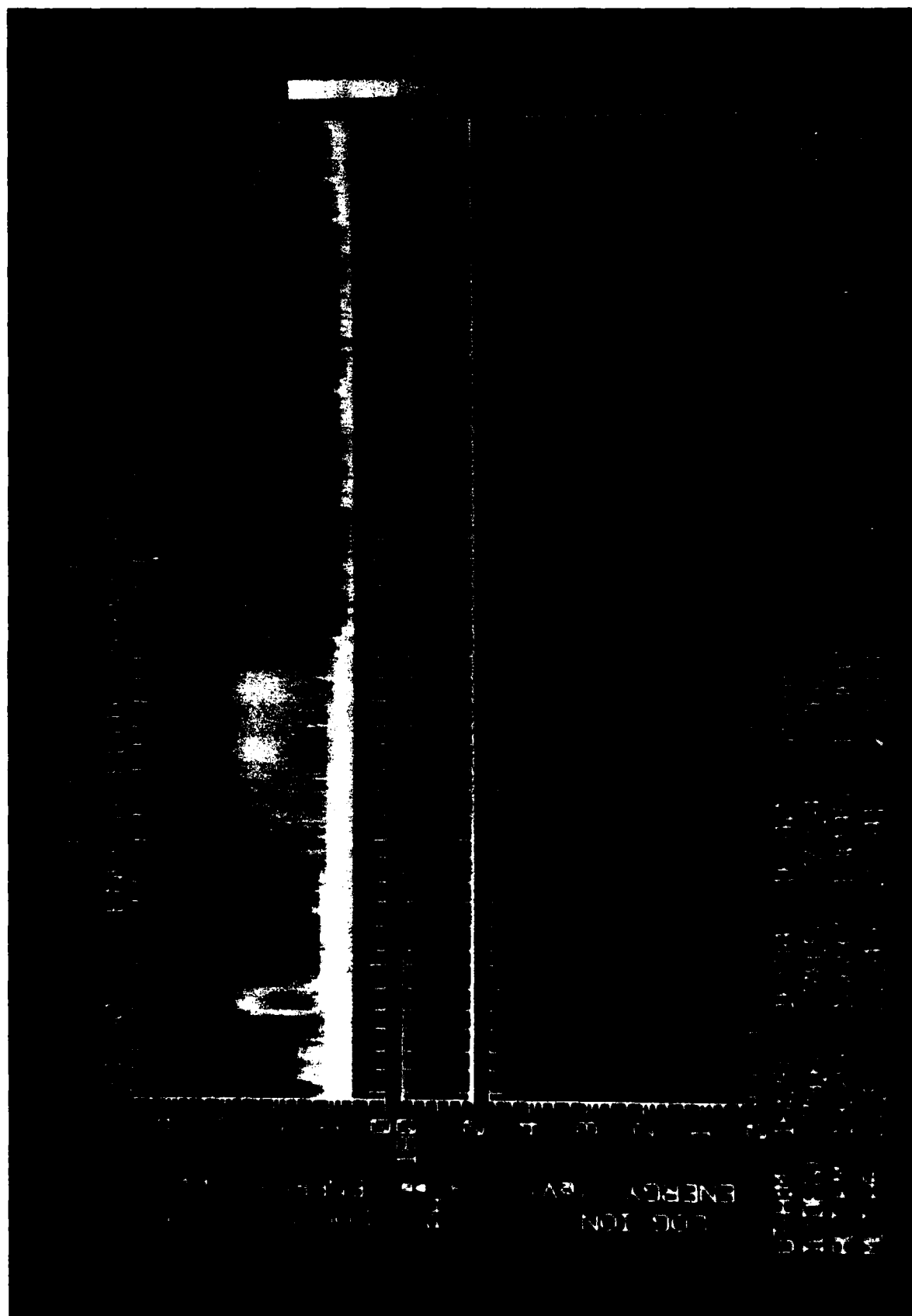
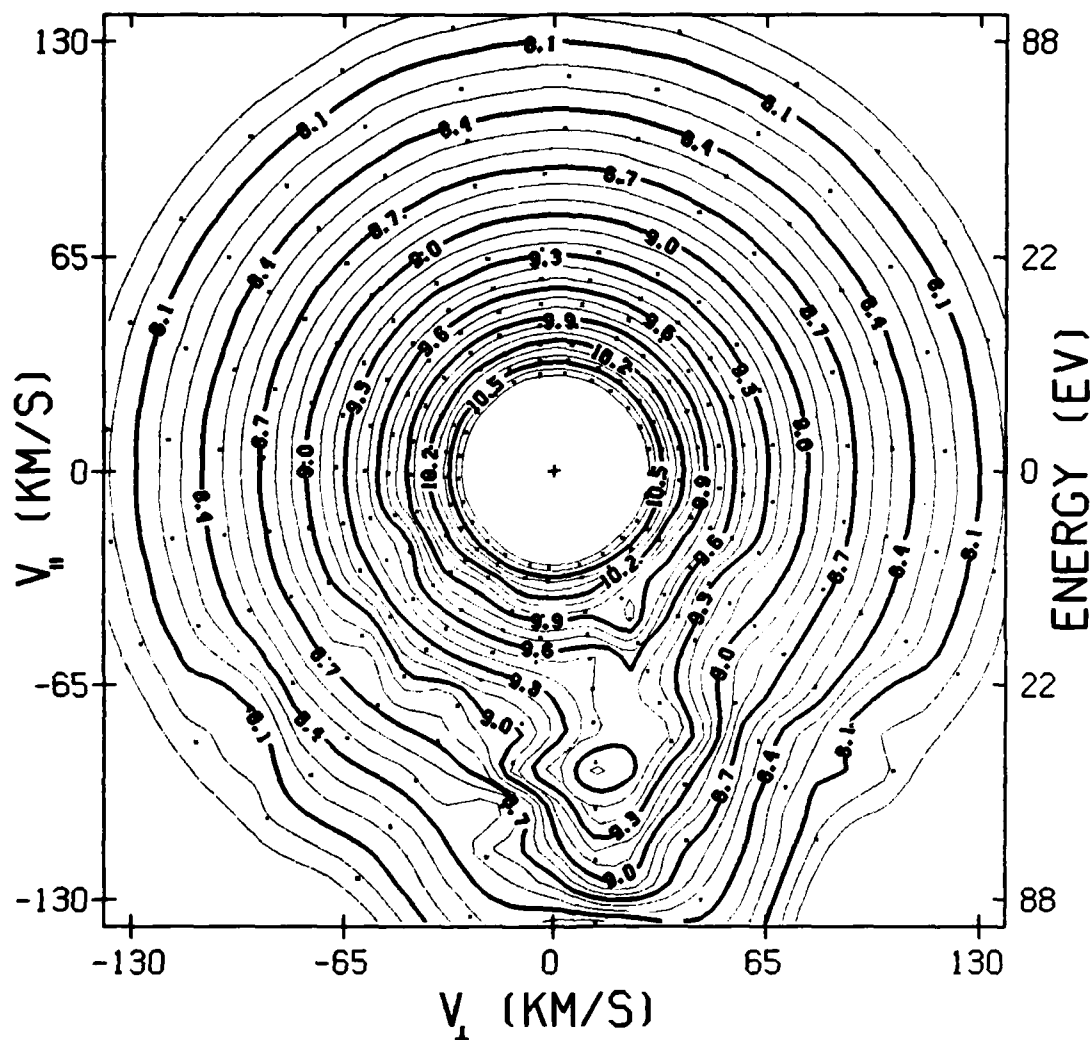


Figure 33. Energy-time spectrograms for 180° pitch angle ions and 0° pitch angle electrons observed at DE-1.

DE-1 HAPI IONS
81290 (17 OCT. 81)
16:32:45.1 TO 16:32:57.1 U.T.



ILAT (D) 78.8
MLT (HR) 22.6
ALT (KM) 18819
GLAT (D) 75.9
GLONG (D) 66.3

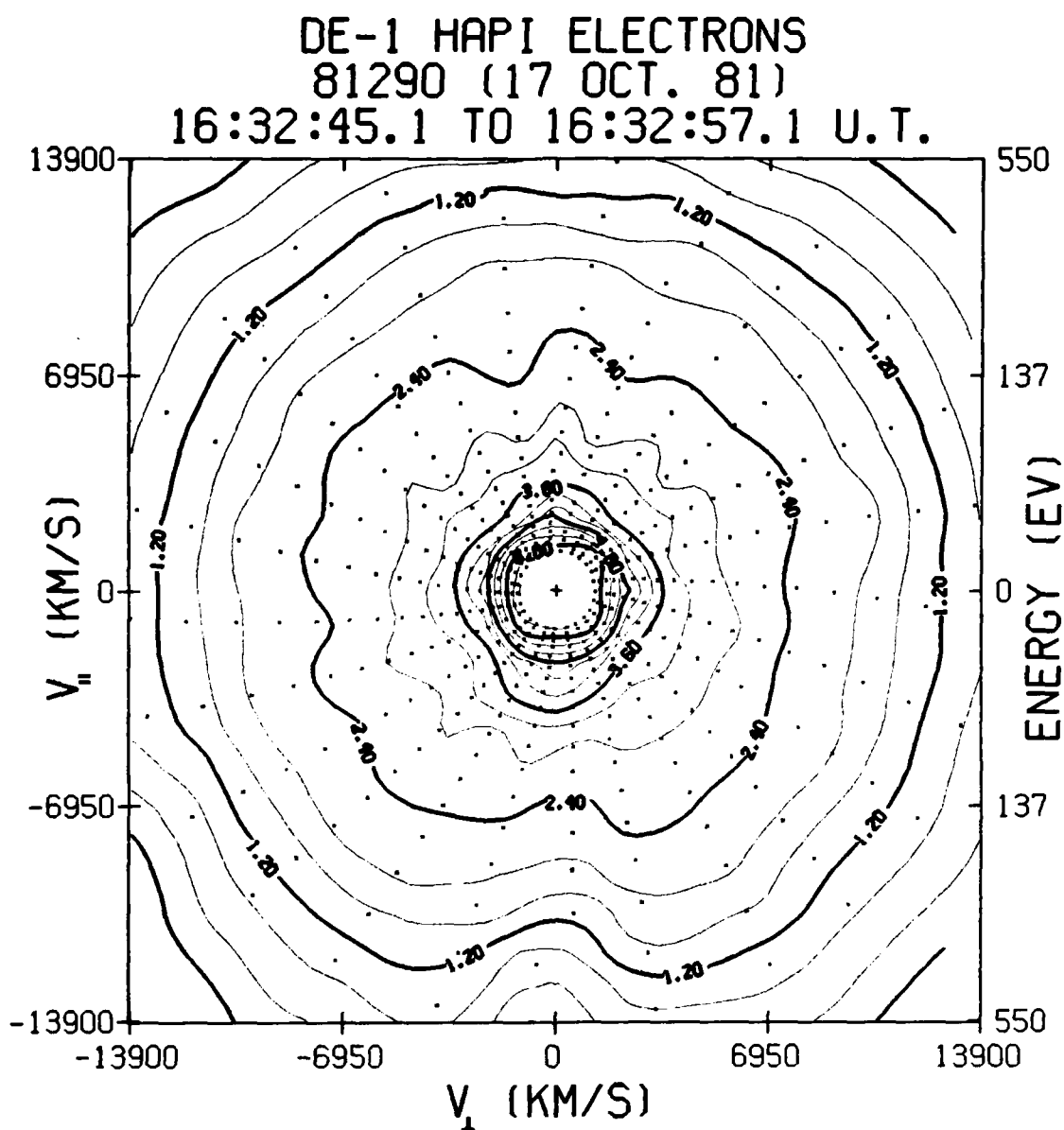
DISTRIBUTION CONTOURS LOG F (SEC³/KM³)

MIN EV	MAX EV	AV. EV.	AMPS/M ²
6.	417.	4.17E+01	-1.47E-08

FLUX (/CM ² S)	DEN (/CM ³)	ERGS/CM ² S
90 - 180	90 - 180	90 - 180
1.05E+07	1.27E+00	9.69E-04

VPAR (KM/S)	PC (MHOS)	HC (MHOS)
-7.23E+01	N/A	N/A

FIGURE 34a. Isocontours of the distribution function for ions at DE-1



ILAT (D) 78.8
MLT (HR) 22.6
ALT (KM) 18819
GLAT (D) 75.9
GLONG (D) 66.3

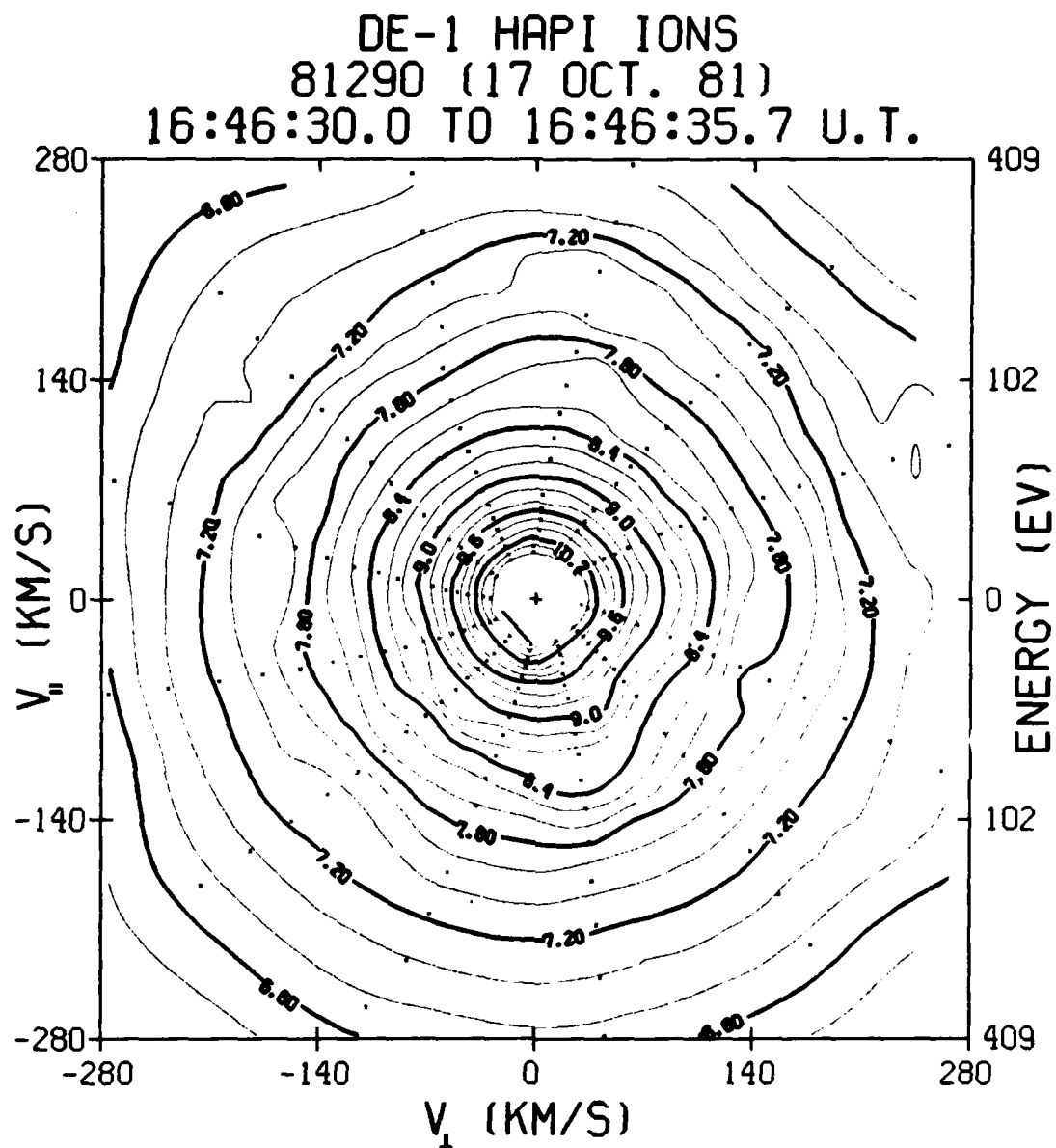
DISTRIBUTION CONTOURS LOG F (SEC³/KM³)

MIN EV	MAX EV	AV. EV.	AMPS/M ²
6.	739.	1.60E+01	-1.47E-07

FLUX (1/CM ² S)	DEN (1/CM ³)	ERGS/CM ² S
0 - 90	0 - 90	0 - 90
4.02E+09	2.04E+01	2.84E-01

VPAR (KM/S)	PC (MHOS)	HC (MHOS)
-2.24E+01	N/A	N/A

FIGURE 34b. Isocontours of the distribution function for electrons at DE-1



ILAT (ID) 76.1
MLT (HR) 22.4
RLT (KM) 17313
GLAT (ID) 70.7
GLONG (ID) 63.0

DISTRIBUTION CONTOURS LOG F (SEC³/KM³)

MIN EV	MAX EV	AV. EV.	AMPS/M ²
6.	554.	2.91E+02	-3.77E-09

FLUX (1/CM ² S)	DEN (1/CM ³)	ERGS/CM ² S
0 - 90	0 - 90	0 - 90
9.44E+06	4.17E-01	5.09E-03

VPAR (KM/S)	PC (MMOS)	MC (MMOS)
-1.32E+01	N/A	N/A

FIGURE 35a. Isocontours of the distribution function for ions at DE-1

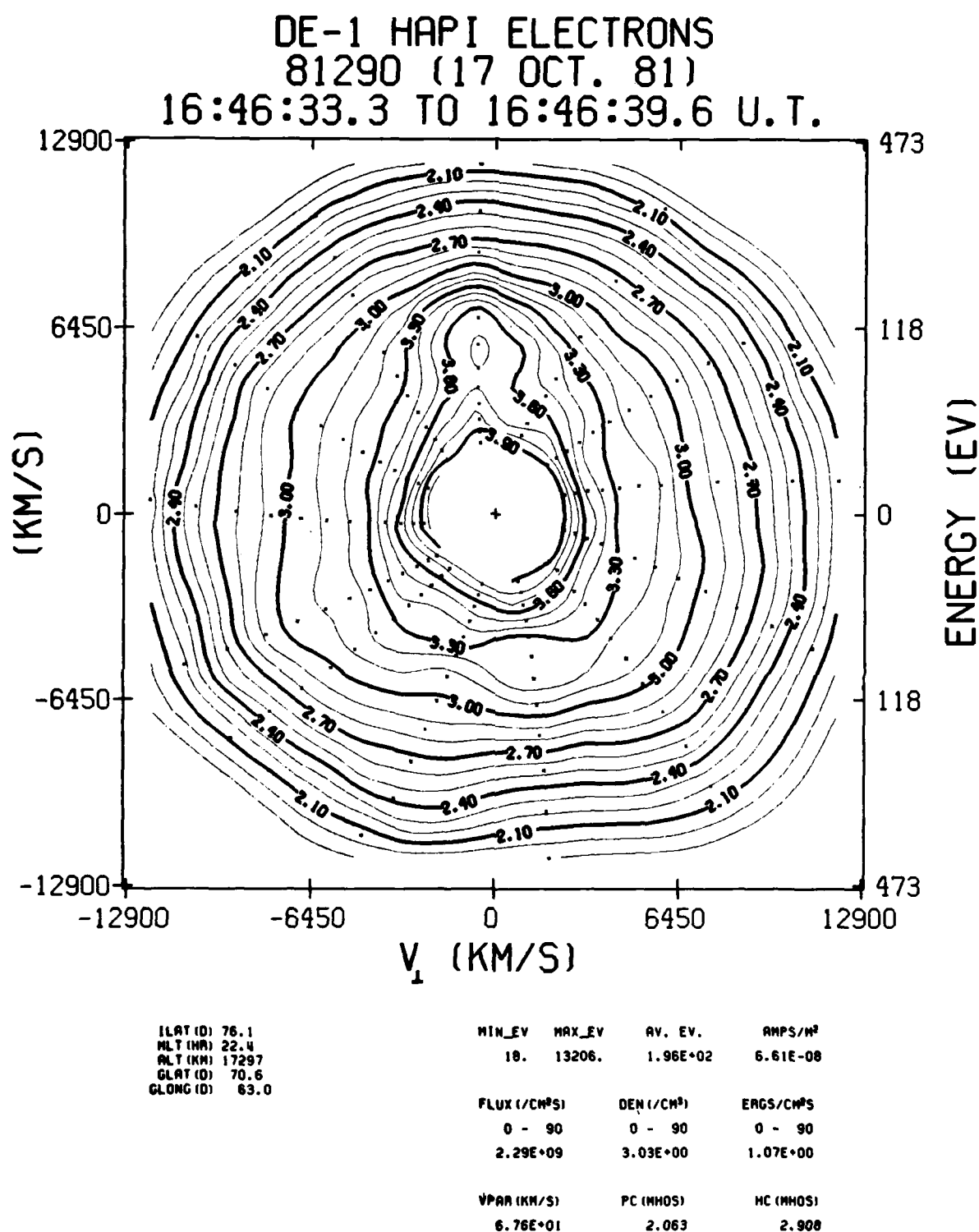


FIGURE 35b. Isocontours of the distribution function for electrons at DE-1

IX. PUBLICATIONS SUPPORTED BY CONTRACT

- Burch, J.L., P.H. Reiff, R.A. Heelis, J.D. Winningham, W.B. Hanson, C. Gurgiolo, J.D. Menietti, R.A. Hoffman, and J.N. Barfield, Plasma Injection and Transport in the Mid-Altitude Polar Cusp, Geophys. Res. Lett., 9, 921, 1982.
- Gurgiolo, C. and J.L. Burch, DE-1 Observations of the Polar Wind--A Heated and Unheated Component, Geophys. Res. Lett., 9, 945, 1982.
- Gurgiolo, C., D.W. Slater, J.D. Winningham, and J.L. Burch, Observations of a Heated Electron Population Associated With the 6300A SAR Arc Emission, Geophys. Res. Lett., 9, 965, 1982.
- Lin, C.S., J.L. Burch, S.D. Shawhan, and D.A. Gurnett, Correlation of Electrostatic Hiss and Upward Electron Beams Near the Polar Cusp, submitted to J. Geophys. Res., 1983.
- Lin, C.S., M. Sugiura, J.L. Burch, J.N. Barfield, and E. Nielsen, DE-1 Observations of Type-1 Counterstreaming Electrons and Field-Aligned Currents, accepted by Journal of Geophysical Research, 1984.
- Winningham, J.D. and C. Gurgiolo, DE-2 Photoelectron Observation Consistent With a Large Scale Parallel Electric Field Over the Polar Cap, Geophys. Res. Lett., 9, 977, 1982.

X. PAPERS PRESENTED AT SCIENTIFIC MEETINGS

Edwards, P.A., L.A. Frank, J.D. Craven, J.L. Burch and J.D. Winningham, Sun-aligned polar cap auroral arcs and their implications concerning magnetospheric dynamics, paper presented at the spring annual meeting of the American Geophysical Union, May, 1982

Varosi, F. H.G. Mayr, H.S. Porter, L.A. Frank, J.D. Craven, J.D. Winningham, L.H. Brace, Precipitating electron distribution inferred from dynamics explorer (DE-1) auroral images, paper presented at the spring annual meeting of the American Geophysical Union, May, 1982

Burch, J.L., J.D. Winningham and C. Gurgiolo, Simultaneous hot plasma observations by dynamics Explorer 1 and 2, paper presented at the spring annual meeting of the American Geophysical Union, May, 1982

Lin, C.S., J.L. Burch, J.D. Menietti and J.D. Winningham, DE observations of counterstreaming electrons: a HAPI look, paper presented at the spring annual meeting of the American Geophysical Union, May, 1982

Kozyra, J.U., T.E. Cravens, A.F. Nagy, L.H. Brace, N.C. Maynard, J.D. Winningham and B.A. Emery, Observational characteristics of stable auroral red arc events, paper presented at the spring annual meeting of the American Geophysical Union, May, 1982

Hernandez, G., J.W. Meriwether, D.W. Slater, R.G. Roble, B.A. Emery, J.U.Kozyra, A.F.Nagy, L.H.Brace, J.D.Winningham, and D.S.Evans, Thermospheric response to the October 21 and 23, 1981 SAR-arcs and aurora as observed from Fritz Peak, Colorado, and Calgary, Alberta during the Dynamics Explorer (DE-2) and NOAA-6 satellite overflights, paper presented at the spring annual meeting of the American Geophysical Union, May, 1982

Curtis, S.A., W.R. Hoegy, L.H. Brace, N.C. Maynard, M. Sugiura and D. Winningham, Ionospheric temperature and density structuring in the low altitude polar cusp, paper presented at the spring annual meeting of the American Geophysical Union, May, 1982

Chang, T., B. Coppi, J. Jasperse, B. Basu, and J. Retterer and J.L. Burch, Electron beams, lower hybrid waves, and ion conics in the lower supauroral region, paper presented at the spring annual meeting of the American Geophysical Union, May, 1982

Sharber, J.R., J.D. Winningham and E.J. Weber, Comparison of DE-2 soft particle observations with 6300A enhancements in the polar cap, paper presented at the fall annual meeting of the American Geophysical Union, December, 1982

Slater, D.W., C. Gurgiolo, E.W. Kleckner, J.D. Winningham and J.L. Burch, Observational evidence of a SAR-arc energy source: precipitating electrons, paper presented at the fall annual meeting of the American Geophysical Union, December, 1982

Lin, C.S., J.L. Burch, D.A. Gurnett and S.D. Shawhan, Plasma instabilities equatorward of the polar cusp, paper presented at the fall annual meeting of the American Geophysical Union, December, 1982

Heelis, R.A., J.D. Winningham, D.M. Klumpar, M. Sugiura, N.C. Maynard and L.H. Brace, DE-2 observations of transverse and parallel ion acceleration, paper presented at the fall annual meeting of the American Geophysical Union, December, 1982

Burch, J.L. and P.H. Reiff, Upward electron beams measured by DE-1 - a potential source of dayside region-1 field-aligned currents, paper presented at the fall annual meeting of the American Geophysical Union, December, 1982

Barfield, J.N., C.S. Lin, J.L. Burch, J.D. Winningham, C. Gurgiolo, J.D. Menietti, and N.A. Saflekos, Polar plasmas as observed by dynamics explorer 1 and 2, paper presented at USAF/NASA Spacecraft Environmental Interactions Technology Conference, October, 1983.

REFERENCES

Anderson, H. R., and R. R. Vondrak, Observations of Birkeland currents at auroral latitudes, Rev. Geophys. Space Phys., 13, 243, 1975.

Arnoldy, R. L., Auroral particle precipitation and Birkeland currents, Rev. Geophys. Space Phys., 12, 217, 1974.

Anderson, H. R., and R. R. Vondrak, Observations of Birkeland currents at auroral latitudes, Rev. Geophys. Space Phys., 13, 243, 1975.

Anderson, H. R., Birkeland currents and auroral structure, in Auroral Processes, ed. by C. T. Russell, p. 181, Japan Scientific Societies Press, Tokyo, 1979.

Barbier, D., The Auroral activity at low altitudes, Ann. Geophys., 14, 334, 1958.

Berko, F. W., R. A. Hoffman, R. K. Burton, and R. E. Holzer, Simultaneous particle and field observations of field-aligned currents, J. Geophys. Res., 80, 37, 1975.

Burch, J. L., S. A. Fields, and R. A. Heelis, Polar Cap Electron Acceleration Regions, J. Geophys. Res., 84, 5863, 1979.

Burch, J. L., P. H. Reiff, R. W. Spiro, R. A. Heelis, and S. A. Fields, Cusp region particle precipitation and ion convection for northward interplanetary magnetic field, Geophys. Res. Lett., 7, 393, 1980.

Burch, J. L., J. D. Winningham, V. A. Blevins, N. Eaker, W. C. Gibson, and R. A. Hoffman, High-altitude plasma instrument for Dynamics Explorer-A, Space Sci. Instrum., 5, 455, 1981.

Burch, J. L., P. H. Reiff, and M. Sugiura, Upward electron beams measured by DE-1: A primary source of dayside region-1 Birkeland currents, Geophys. Res. Lett., 10, 753, 1983.

Burch, J. L., S. A. Fields, and R. A. Heelis, Polar cap electron acceleration regions, J. Geophys. Res., 84, 5863, 1979.

Burch, J. L., J. D. Winningham, V. A. Blevins, N. Eaker, W. C. Gibson, and R. A. Hoffman, High altitude plasma instrument for Dynamics Explorer-A, Space Sci. Instrum., 5, 455, 1981.

Burch, J. L., P. H. Reiff, R. A. Heelis, J. D. Winningham, W. B. Hanson, C. Gurgiolo, J. D. Menietti, R. A. Hoffman, and J. N. Barfield, Plasma injection and transport in the mid-altitude polar cusp, Geophys. Res. Lett., 9, 921, 1982.

Burke, W. J., D. A. Hardy, F. J. Rich, M. C. Kelley, M. Smiddy, B. Shuman, R. C. Sagalyn, R. P. Vancour, P. J. Wildman, and S. T. Lai, Electrodynamical structure of the late evening sector of the auroral zone, J. Geophys. Res., 85, 1179, 1980.

Burke, W. J., Magnetosphere-Ionosphere Coupling, Contributions from IMS Satellite Observations, Rev. Geophys. Space Phys., 20, 685, 1982.

Burke, W. J., M. S. Gussenhoven, M. C. Kelley, D. A. Hardy, and F. J. Rich, Electric and Magnetic Field Characteristics of Discrete Arcs in the Polar Cap, J. Geophys. Res., 87, 2431, 1982.

Carlson, C. W., and R. B. Torbert, Solar wind ion injections in the morning auroral oval, J. Geophys. Res., 85, 2903, 1980.

Chang, T., and B. Coppi, Lower Hybrid Acceleration and Ion Evolution in the Supraauroral Region, Geophys. Res. Lett., 18, 1253, 1981.

Chiu, Y. T., and M. Schulz, Self-consistent particle and parallel electrostatic field distributions in the magnetospheric-ionospheric auroral region, J. Geophys. Res., 83, 629, 1978.

Cole, K. D., Stable auroral red arcs, sinks for energy of Dst main phase, J. Geophys. Res., 70, 1689, 1965.

Collin, H. L., R. D. Sharp, and E. G. Shelley, The occurrence and characteristics of electron beams over the polar regions, J. Geophys. Res., 87, 7504, 1982.

Cornwall, J. M., F. V. Coroniti and R. M. Thorne, Unified theory of SAR arc formation at the plasmopause, J. Geophys. Res., 76, 4428, 1971.

Dusenbery, P. B., and L. R. Lyons, Generation of Ion-Conic Distribution by Upgoing Ionospheric Electrons, J. Geophys. Lett., 18, 1253, 1981.

Dusenbery, P. B., and L. R. Lyons, Generation of ion-conic distribution by upgoing ionospheric electrons, J. Geophys. Res., 86, 7627, 1981.

Evans, D. S., Precipitating electron fluxes formed by a magnetic field aligned potential difference, J. Geophys. Res., 79, 2853, 1974.

Farthing, W. H., M. Sugiura, B. G. Ledley, and L. J. Cahill, Jr., Magnetic field observations on DE-A and -B, Space Sci. Instr., 5, 551, 1981.

Farthing, W. H., M. Sugiura, B. G. Ledley, and L. J. Cahill, Jr., Magnetic field observations on DE-A and -B, Space Sci. Instrum., 5, 551, 1981.

Fennell, J. F., D. J. Gorney, and P. F. Mizera, Auroral particle distribution functions and their relationship to inverted V's and auroral arcs, Physics of Auroral Arc Formation, ed. by S.-I. Akasofu and J. R. Kan, AGU, Wash. D.C., 1981, p. 91.

Foster, J. D. and J. R. Burrows, Electron Fluxes over the Polar Cap 1. Intense keV Fluxes During Poststorm Quieting, J. Geophys. Res., 81, 6016, 1976.

Frank, L. A., Plasma in the earth's polar magnetosphere, J. Geophys. Res., 76, 5202, 1971.

Gorney, D. J., A. Clarke, D. R. Croley, J. F. Fennell, J. Luhman, and P. Mizera, The Distributions of Ion Beams and Conics below 8000 km, J. Geophys. Res., 86, 83, 1981.

Gurgiolo, C. and J. L. Burch, DE-1 Observations of the Polar Wind--A Heated and an Unheated Component, Geophys. Res. Lett., 9, 945, 1982.

Gurnett, D. A., and L. A. Frank, Plasma waves in the polar cusp: observations from Hawkeye 1, J. Geophys. Res., 83, 1447, 1978.

Hanson, W. B., R. A. Heelis, R. A. Power, C. R. Lippincott, D. R. Zuccaro, B. J. Holt, L. H. Harmon, and S. Sanatani, The retarding potential analyzer for Dynamics Explorer-B, Space Sci. Instrum., 5, 503, 1981.

Hardy, D. A., W. J. Burke, and M. S. Gussenhoven, DMSP Optical and Electron Measurements in the Vicinity of Polar Cap Arcs, J. Geophys. Res., 87, 2413, 1982.

Hasagawa, A., and K. Mima, Anomalous transport produced by Kinetic Alfvén wave turbulence, J. Geophys. Res., 83, 1117, 1978.

Heelis, R. A., W. B. Hanson, C. R. Lippincott, D. R. Zuccaro, L. H. Harmon, B. J. Holt, J. E. Doherty, and R. A. Power, The ion drift meter for Dynamics Explorer-B, Space Sci. Instrum. 5, 511, 1981.

Heikkila, W. J., Impulsive plasma transport through the magnetopause, Geophys. Res. Lett., 9, 159, 1982.

Hoffman, J. H. and W. H. Dodson, Light Ion Concentrations and Fluxes in the Polar Regions during Magnetically Quiet Times, J. Geophys. Res., 85, 626, 1980.

Iizuka, S., P. Michelson, J. J. Rasmussen, R. Schrittwieser, R. Hatakeyama, K. Saeki and N. Sato, Dynamics of a potential barrier formed on the tail of a moving double layer in a collisionless plasma, Phys. Rev. Lett., 48, 145, 1982.

Johnstone, A. D., and J. D. Winningham, Satellite observations of suprathermal electron bursts, J. Geophys. Res., 87, 2321, 1982.

Kleckner, E. W., J. J. Michalsky, L. L. Smith, J. R. Schmelzer, R. H. Severtsen, J. L. Berndt, and D. W. Slater, A multipurpose, computer controlled, mobile automatic scanning photometer (MASP), in Proceedings of the Finnish-American Auroral Workshop, Aug. 17-20, 1981 in Oulu, Finland, ed. L. Jalonen and T. Nygren, Finnish Academy of Science and Letters, Sodankylä Geophysical Observatory, pg. 141-148, 1981.

Klumpar, D. M., Relationship between auroral particle distributions and magnetic field perturbations associated with field-aligned currents, J. Geophys. Res., 84, 6524, 1979.

Klumpar, D. M., and W. J. Heikkila, Electrons in the ionospheric source cone: evidence for runaway electrons as carriers of downward Birkeland currents, Geophys. Res. Lett., 9, 873, 1982.

Knight, S., Parallel electric fields, Planet. Space Sci., 21, 741, 1973.

Lee, J. S., J. P. Doering, T. A. Potemra, and L. H. Brace, Measurements of the ambient photoelectron spectrum from Atmosphere Explorer: II AE-E measurements from 300-100 km during solar minimum conditions, Planet. Space Sci., 28, 973, 1980.

Lemaire, J., and M. Roth, Penetration of solar wind plasma elements into the magnetosphere, J. Atmos. Terr. Phys., 40, 331, 1978.

Leroy, M. M., C. C. Goodrich, D. Winske, C. S. Wu and K. Papadopoulos, Simulation of a perpendicular shock, Geophys. Res. Lett., 8, 1269, 1981.

Lin, C. S., and R. A. Hoffman, Fluctuations of inverted V electron fluxes, J. Geophys. Res., 84, 6547, 1979.

Lin, C. S., B. Mauk, G. K. Parks, S. DeForest, and C. E. McIlwain, Temperature characteristics of electron beams and ambient particles, J. Geophys. Res., 84, 2651, 1979.

Lin, C. S., J. L. Burch, J. D. Winningham, J. D. Menietti, and R. A. Hoffman, DE-1 observations of counterstreaming electrons at high altitudes, Geophys. Res. Lett., 9, 925, 1982.

Lin, C. S., J. L. Burch, S. D. Shawhan, and D. A. Gurnett, Correlation of electrostatic hiss and upward electron beams near the polar cusp, submitted to J. Geophys. Res., 1983.

Lysak, R. L., M. K. Hudson, and M. Temerin, Ion Heating by Strong Electrostatic Ion Cyclotron Turbulence, J. Geophys. Res., 85, 678, 1980.

Maier, E. J., S. E. Kayser, J. R. Burrows, and D. M. Klumpar, The suprathermal electron contributions to high-latitude Birkeland currents, J. Geophys. Res., 85, 2003, 1980.

Mizera, P. F., J. F. Fennell, D. R. Croley, Jr., and D. J. Gorney, Charged particle distributions and electric field measurements from S3-3, J. Geophys. Res., 86, 7566, 1981.

Moore, T. E., and R. L. Arnoldy, Plasma pitch angle distributions near the substorm injection front, J. Geophys. Res., 87, 265, 1982.

Nielsen, E., and R. A. Greenwald, Electron flow and visual aurora at the Harang Discontinuity, J. Geophys. Res., 84, 4189, 1979.

Rees, M. H., and S. Akasofu, On the association between subvisual red arcs and the Dst(H) decrease, Planet. Space Sci., 11, 105, 1963.

Reiff, P. H., J. L. Burch, and R. W. Spiro, Cusp proton signatures and the interplanetary magnetic field, J. Geophys. Res., 85, 5997, 1980.

Reiff, P. H., T. W. Hill, and J. L. Burch, Solar wind plasma injection at the dayside magnetospheric cusp, J. Geophys. Res., 82, 479, 1977.

Russell, C. T., and E. W. Greenstadt, Initial ISEE magnetometer results; shock observations, Space Sci. Rev., 23, 3, 1979.

Saflekos, N. A., R. E. Sheehan, and R. L. Carovillano, Global nature of field-aligned currents and their relation to auroral phenomena, Rev. of Geophys. and Space Phys., 20, 709, 1982.

Schunk, R. D., and D. S. Watkins, Proton Temperature Anisotropy in the Polar Wind, J. Geophys. Res., 87, 171, 1982.

Senior, C., R. M. Robinson, and T. A. Potemra, Relationship between field-aligned currents, diffuse auroral precipitation and the westward electrojet in the early morning sector, J. Geophys. Res., 87, 10469, 1982.

Sharp, R. D., R. G. Johnson, and E. G. Shelley, Energetic particle measurements from within ionospheric structures responsible for auroral acceleration processes, J. Geophys. Res., 84, 480, 1979.

Sharp, R. D., E. G. Shelley, R. G. Johnson, and A. G. Ghielmetti, Counter-streaming electron beams at altitudes of $1 R_e$ over the auroral zone, J. Geophys. Res., 85, 92, 1980.

Shelley, E. G., R. D. Sharp, and R. G. Johnson, He⁺⁺ and H⁺ flux measurements in the dayside cusp: estimates of convection electric field, J. Geophys. Res., 81, 2363, 1976.

Sugiura, M., N. C. Maynard, W. H. Farthing, J. P. Heppner, and B. G. Ledley, Initial results on the correlation between the magnetic and electric fields observed from the DE-2 satellite in the field-aligned current regions, Geophys. Res. Lett., 9, 985, 1982.

Sugiura, M., T. Iyemori, R. A. Hoffman, N. C. Maynard, J. L. Burch, and J. D. Winningham, Relationships between field-aligned currents, electric fields, and particle precipitation as observed by Dynamics Explorer-2, Magnetospheric Currents, ed. T. A. Potemra, page 96, AGU, Washington, D. C., 1983.

Ungstrup, E., D. M. Klumppar, and W. J. Heillila, Heating of Ions to Super-thermal Energies in the Topside Ionosphere by Electrostatic Ion Cyclotron Waves, J. Geophys. Res., 84, 4289, 1979.

Wagner, J. S., A computer simulation of auroral arc formation, Ph.D. thesis, Geophysics Institute, Univ. of Alaska, Fairbanks, Alaska, 1980.

Wagner, J. S., J. R. Kan, S.-I. Akasofu, T. Tajima, J. N. Leboeuf and J. M. Dawson, A simulation study of V-potential double layers and auroral arc formations, Physics of Auroral Arc Formation, ed. by S.-I. Akasofu and J. R. Kan, AGU, Washington, D.C., 1981, p. 304.

Winningham, J. D., and W. J. Heikkila, Polar Cap Electron Fluxes Observed with ISIS-1, J. Geophys. Res., 79, 949, 1974.

Winningham, J. D., F. Yaschara, S. I. Akasofu, and W. J. Heikkila, The latitudinal morphology of 10-eV to 10-keV electron fluxes during magnetically quiet and disturbed times in the 2100-0300 MLT sector, J. Geophys. Res., 80, 3148, 1975.

Winningham, J. E., J. L. Burch, N. Eaker, V. A. Blevins, and R. A. Hoffman, The Low Altitude Plasma Instrument (LAPI), Space Sci. Instr., 5, 465, 1981.

Winningham, J. D., and C. Gurgiolo, DE-2 photoelectron measurements consistent with a large scale parallel electric field over the polar cap, Geophys. Res. Lett., 9, 977, 1982.

Zanetti, L. J., T. A. Potemra, J. P. Doering, J. S. Lee, and R. A. Hoffman, Magnetic field-aligned electron distributions in the dayside cusp, J. Geophys. Res., 86, 8957, 1981.

END

DTIC

7-86